Lattice QCD studies of inclusive semileptonic decays of charmed mesons

Kellermann, Ryan

Doctor of Philosophy

Department of Particle and Nuclear Physics
School of High Energy Accelerator Science

The Graduate University for Advanced Studies, SOKENDAI

March 2024

Abstract

The Standard Model of Particle Physics (SM) combines the knowledge that has been accumulated over the last century into one comprehensive framework. Nevertheless, the limitations of the theory in describing all phenomena is highlighted by inexplicable discrepancies between experimental measurements and theoretical predictions, motivating the search for New Physics and extensions of the SM.

The long-standing tension in the Cabbibo-Kobayashi-Maskawa (CKM) matrix elements $|V_{cb}|$ and $|V_{ub}|$ of the bottom sector between inclusive and exclusive determination is one such discrepancy. These parameters are mainly extracted from semileptonic decays of B mesons, hence providing theorists and experimentalists alike with an opportunity to review and deepen their understanding of these decays in order to resolve the tension. This is a necessary step in the search for New Physics, since it is imperative to have precise and well-understood predictions of the SM.

We present a nonperturbative calculation of the inclusive decay rate for semileptonic decays of the D_s meson from lattice QCD. We focus on the charm sector to verify the methodology since it is easier to treat in lattice simulations but an extension of the presented formalism towards the bottom sector, in hope of providing new insights into the aforementioned discrepancy, is straightforward once the data becomes available. We present results from a first study based on the computation for the inclusive semileptonic $D_s \to X_s \ell \nu_\ell$ decay using a full and flexible lattice setup, employing the Möbius domain-wall action for all quarks where the masses of the c and s quarks are simulated near their physical values. Our calculation for the decay rate from lattice data of four-point correlation functions is based on the Chebyshev polynomial approximation approach. We compare the results of our analysis for $\Gamma/|V_{cs}|^2$ with experimental measurements from the BESIII collaboration to obtain a first prediction for the CKM matrix element. We further perform a cross-check of the inclusive analysis strategy by studying the ground-state limit, comparing it to results obtained from form factors for the exclusive decay mode, and to which degree it dominates the inclusive decay rate.

We further present a first estimation of systematic effects in the inclusive analysis strategy, namely, we address the systematic error introduced through the Chebyshev approximation as well as the influence of finite volume effects in our analysis. The former is estimated by a combination of the required limits and employing properties of the Chebyshev polynomials, while the latter is estimated by formulating a model under the assumption of two-body final states which is combined with the lattice data to extrapolate the infinite volume limit.

Contents

Chapter 1

Introduction

One of the most fundamental characteristics of mankind is the aim to explore and explain the mechanisms of nature. This endeavor manifests itself in two different ways, a philosophical-spiritual approach on one hand and a scientific-mathematical on the other. The latter expresses itself by formulating theories and carrying out experiments based on the principles of verification and reproducibility. The goal is to describe the Nature in a universal language. As part of this development the limits and sizes for experiments become broader, from the giant dimensions of astrophysics up to quantum mechanics, the magnitude and scale of our physical reality have long since left our everyday perception. To proceed in these areas new challenges for theories and experiments arise. In the last century considerable achievements were made in the field of particle physics, these results are now known as the *Standard Model of Particle Physics* (SM). Especially the early times of modern particle physics were dominated by revolutions and new discoveries, starting from the discovery of the atomic nucleus by E. Rutherford in 1911. The most recent success was the proof of existence of the *Higgs-boson*[1], completing the experimental verification of all particles of the SM at the *Large Hadron Collider* at the Research Center CERN in Geneva. In recent years the Standard Model has proven to be extremely consistent and accurate in its explanation of experimental results. Nevertheless, there are some indications that the Standard Model is not complete as of yet:

- The Standard Model possesses 18 free parameters (including neutrino masses and mixing angles this number is raised to 25). But even though the physical effects of the Standard Model can be ascribed to these parameters, the question concerning their origin remains unanswered. While their magnitude can be measured experimentally, they are not determined by the Standard model itself. For the sake of simplifying the theory the goal is to reduce the number of parameters as far as possible.

- Within the Standard Model neutrinos are introduced as massless particles. Experiments concerning neutrino oscillations however, show that neutrinos actually possess a mass, even though it is very small. And even though extensions of the SM are capable of describing neutrino masses, none have been experimentally proven.

- Although gravity is the oldest known force in nature, currently there is no way to describe it in the SM. A consistent description of gravitation in analogy to the other forces in the framework of a gauge theory failed up until now.

- Looking at the Higgs mechanism the so called *hierarchy problem* is encountered. At first sight the mass of the Higgs boson should be very large based on radiation and quantum corrections, namely in the range of the Planck scale ($m_P \sim \mathcal{O}(10^{19}\,\mathrm{GeV})$)[2]. But since the Higgs mass implies the energy scale of weak interaction the Higgs boson should be considerably lighter which was proven at the Large Hadron Collider[1] to be $m_{\mathrm{Higgs}} = 125.10(14)\,\mathrm{GeV}$[3]. In the end it results in the question why gravitation is much weaker than the electroweak interaction (~ 26 orders of magnitude) or in another way, why the scales of the different forces in the SM possess such a strict hierarchy. In the SM, this behavior can be explained through some complex fine-tuning of the parameters, so that the hierarchy problem is not in direct contradiction to the SM.

- The matter-anti-matter-asymmetry of the universe can be ascribed to a combination of charge and parity violation (*Charge-Parity (CP)-violation*). While the SM contains CP-violation, it is too small to explain the observed asymmetry.

All these points show that modern physics has not reached its limits. The experimental search for *New Physics* as well as their theoretical description is the topic of several researches. To discover new physics two things are necessary. Firstly, the precision of experiments has to continue to increase. Secondly, based on models, an accurate prediction has to be made from the theoretical side allowing for a comparison. In what follows, before formulating the goal of this work, the physical framework is outlined.

1.1 The Standard Model of Particle Physics

The Standard Model forms the framework for particle physics. In this section the fundamental properties of the SM will be discussed and the aspects of the SM relevant for this thesis will be outlined. Since a detailed treatment of the SM content would go beyond the scope of this work, textbooks and review papers shall be referenced here. For a theoretical standpoint useful references include [2, 4], while [5, 6] choose a more experimentally oriented approach.

Table 1.1: Fermions in the SM and their associated mass m and electric charge in units of e.

Leptons			
Flavor		m / MeV[3]	e
e^-	Electron	0.511	-1
ν_e	Electron-Neutrino	$<2 \times 10^{-6}$	0
μ	Muon	105.7	-1
ν_μ	Muon-Neutrino	$< 0.19 \times 10^{-6}$	0
τ	Tau-Lepton	1777	-1
ν_τ	Tau-Neutrino	$< 18.2 \times 10^{-6}$	0

Quarks			
Flavor		m / GeV[3]	e
u	Up	0.0022	2/3
d	Down	0.0047	-1/3
c	Charm	1.27	2/3
s	Strange	0.093	-1/3
t	Top	172.9	2/3
b	Bottom	4.18	-1/3

The foundation of the SM is build on a series of fundamental achievements in the area of particle physics. Two important examples include the unification of electromagnetic and weak interaction[7, 8] and the proof of asymptotic freedom in *Quantum Chromodynamics* (QCD)[9, 10]. The SM combines the ideas of classical relativistic field theory with the concepts of quantum mechanics, expressing classical fields through operators. The addition of local *gauge symmetries* introduces interactions, creating a Lorentz invariant theory, describing the dynamics and interactions between all known particles (excluding gravity). The elementary particles receive their masses through the *Higgs-mechanism* which describes the interaction of particles with the *Higgs-field*. This field possesses a vacuum expectation value not equal to zero and interacts with particles in such a way, that the normally massless gauge bosons of the theory receive a mass through *spontaneous symmetry breaking* (SSB). The aforementioned Higgs-boson is an excitation of this field.

In this work natural unit will be used, $c = \hbar = 1$.

1.1.1 Particles and Interactions

The SM contains *elementary particles* which, according to present knowledge, have no further substructure and hence build the foundation for all observable particles.

In general there are two different types for particles, *fermions* and *bosons*. The basis for this differentiation is the quantum number called *spin*. While bosons carry an integer spin number, fermions carry an half-integer spin number. Fermions are subdivided in two categories: *leptons* (Greek "leptos": fine, small, thin) and quarks, as shown in Table 1.1.

Each fermion carries a quantum number called *Flavor*. The quark masses are based on the $\overline{\text{MS}}$ scheme at a scale $\mu = 2\,\text{GeV}$. The final column denotes the electric charge of the particle in units of the elementary charge e. For every particle in Table 1.1 there is a corresponding anti-particle.

The listed fermions are subject to the Pauli-principle and hence behave according to the Fermi-Dirac-statistics. Historically, from the 24 known fermions (including anti-particles) only those of the first generation (first line in Table 1.1) were known. Additionally to the electron which was experimentally verified in 1897, Wolfgang Pauli postulated the electron neutrino in 1933 to explain

Table 1.2: Interactions in the SM.

Interactions			
	El.mag.	Weak	Strong
Gauge boson	1 Photon γ	W^+, W^-, Z^0	8 Gluons g
Mass[3]	0	$m_{W^\pm} = 80.4\,\text{GeV}$ $m_{Z^0} = 91.2\,\text{GeV}$	0
Charge	Electric charge	isospin	color charge
Gauge theory	El-weak theory ($SU(2) \times U(1)$)		QCD ($SU(3)$)

the kinematics of beta decays which were not understood until then. Not much later there turned out to be more types of leptons. In 1936 Carl D. Anderson discovered the muon in cosmic rays. The associated neutrino as well as the third generation of leptons were to follow. Within the SM neutrinos are assumed to be massless. Experiments measuring neutrino oscillations, however, showed that neutrinos do have a mass. The upper limit for the mass of the electron neutrinos is currently given with $m_{\nu_e} \leq 2\,\text{eV}$[3]. The latest neutrino experiments, e.g. KATRIN in Karlsruhe try to put further constraints on these limits. In principle the addition of neutrinos with masses to the SM is possible. The extension is similar to the quark sector with lepton-flavor-mixing and introducing the PMNS-matrix (from Pontecorvo, Maki, Nakagawa and Sakata). For a more detailed view on this the aforementioned literature shall be referenced.

The development of the quark model was another important step towards the SM. The improvement of detection methods in the middle of the 20th century was followed by the discovery of a multitude of strongly interacting particles called *hadrons* (Greek "hadros": stout, thick). To properly explain this *particle zoo* M. Gell-Mann and G. Zweig developed the quark model in 1964. This model views hadrons as composite states of two or more elementary particles (u-, d- and s-quarks) based on a $SU(3)$-symmetry group. The model could be experimentally verified early on by the discovery of the Ω^--baryon. Furthermore, new quarks had to be added to the model to explain the discoveries of new hadrons. This development ended with the discovery of the top-quark at the Fermilab 1995, so that currently, analogous to the lepton sector, there are three generations of quarks with two flavors in each generation. Thus, the number of leptons and quarks in the SM is equal[3]. A fundamental reason of that is yet to be understood.

The stable matter that surrounds us is composed of leptons and quarks of the first generation, the nucleons building atomic nuclei consist of up- and down-quarks, while the electrons are coupled to nuclei in atoms. Turning to another fundamental part of our world the interactions of particles between themselves, as far as the current knowledge is concerned, are described by four fundamental interactions. Three of these can be described through gauge theories in the framework of the SM and are listed in Table 1.2.

The fourth fundamental interaction, gravity, could not be consistently included in the SM as

of yet. Each interaction in the SM is transmitted by intermediate particles called gauge bosons. Bosons with their even spin number form the second big group of particles in the SM and obey the *Bose-Einstein-statistics*. In theory, these gauge bosons are massless for reasons of gauge invariance. But experiments show that the gauge bosons of weak interaction do possess a mass (Tab. 1.2). In the SM this is explained by the *Higgs-mechanism*, which gives the exchange particles of weak interaction a mass through spontaneous symmetry breaking. A detailed review of the Higgs-mechanism is beyond our scope here. The gauge bosons couple to particles which carry the charge of the corresponding gauge theory, e.g. photons couple to all particles carrying electrical charge while gluons only interact with particles carrying color charge. One part of the SM is the *electroweak theory* which unites the electromagnetic and weak interaction. Based on the contribution of S. Glashow, A. Salam and S. Weinberg the theory is also known as the *Glashow-Weinberg-Salam-theory* [11–13]. The other part is *Quantum Chromodynamics* (QCD) which represents the theory of strong interaction.

Each of these gauge theories has its symmetry group and the SM can be expressed as a group-theoretic combination of these symmetry groups

$$SU(3)_C \times SU(2)_L \times U(1)_Y. \tag{1.1}$$

Here C denotes the color, L the weak isospin and Y the hypercharge and correspond to the underlying theory. In this work a special emphasis should be put on the $SU(3)_C$, as it is of special importance for the theory of strong interaction and hence the description of hadronic decays. It will be discussed in more detail in chapter 1.2. For a more detailed discussion on gauge theories and symmetry groups we refer to the named literature. For a more mathematical stand point on group theory and gauge theory we refer to [14].

1.1.2 CKM-matrix and the Unitarity Triangle

Additionally to the aforementioned classification of fermions based on spin, fermions can also be classified based on their chirality. There are *left-handed* and *right-handed* fermions, generally denoted by indices L and R, respectively. To change the chirality of a particle a parity operation P is used which correspond to a reflection of all coordinates to a plane. And while the massive fermions and quarks may show both handedness, in the framework of the minimal SM there are no right-handed neutrinos or left-handed anti-neutrinos. This represents a parity violation shown experimentally in beta decays by C. Wu in 1957[15].

Another symmetry operation is the charge conjugation C which inverts the charge of a particle. The combination of charge- and parity conjugation is known as CP-transformation which transfers a particle to its corresponding anti-particle. For a long time it was assumed that CP is an universally realized symmetry but observations show an asymmetry between particles and anti-particles. The first experimental evidence for CP-violation was found in kaon decays in 1964[16]. After CP-

symmetry was proven to be non universal nowadays CPT-invariance is assumed in which T is an inversion of the time coordinates. This fact is formulated in the *CPT-theorem* and is experimentally verified up until now. More experiments are probing the CPT-theorem, e.g. CERN at Geneva and FAIR in Darmstadt.

The explanation of CP-violation is closely related to the mechanism that is responsible for generating the quark masses, since in the SM particles receive their masses through *Yukawa couplings* in the Lagrangian density, where left- and right-handed components of the quark fields couple to each other. The corresponding term has the form

$$\mathcal{L}_{\text{Yukawa}} = -(M_u^{ij}\bar{u}_L^i u_R^j + M_d^{ij}\bar{d}_L^i d_R^j + \text{h.c.}) \tag{1.2}$$

where $u_{L,R}^{i,j}$ and $d_{L,R}^{i,j}$ denote the upper and lower elements of the respective quark family, i.e.

$$u_H^i = (u_H, c_H, t_H), \quad d_H^i = (d_H, s_H, b_H), \quad H = L, R\,. \tag{1.3}$$

In general the upper elements are called *up-type*-quarks, while the lower elements are called *down-type*-quarks. The factors $M_{u,d}^{ij}$ mediate the coupling between the quark fields and can be identified as mass matrices of the quarks. Initially, these matrices are not required to be diagonal, so that the mixing of different quark families contribute to the mass states. But since the physical quarks are mass eigenstates where each quark interacts only with itself, a change of basis has to be performed to diagonalize the mass matrices. But since the quarks also couple to the weak gauge bosons of the weak interaction, this change of basis does not only change the mass terms of the Lagrangian density but also the weak interaction terms. While in the initial basis the charged W-bosons could only induce a quark-type change within one family (*flavor changing current*) in the new basis the transition of each type of up-type quark to every type of down-type-quark is now possible. So while in the initial basis the quarks are electroweak eigenstates (d', s', b') in the new base they are physical mass eigenstates (d, s, b). For the sake of illustration, only the down-type quarks are listed here. The matrix governing these transitions is known as CKM-matrix (named after N. Cabibbo, M. Kobayashi and T. Maskawa)[17, 18] and for the down-type quarks has the form

$$\begin{pmatrix} d' \\ s' \\ b' \end{pmatrix} = \underbrace{\begin{pmatrix} V_{ud} & V_{uc} & V_{ub} \\ V_{cd} & V_{cs} & V_{cb} \\ V_{td} & V_{ts} & V_{tb} \end{pmatrix}}_{V_{\text{CKM}}} \begin{pmatrix} d \\ s \\ b \end{pmatrix}, \tag{1.4}$$

so that the eigenstates of the weak interaction are a linear combination of the mass eigenstates. The complex matrix elements characterize the transition between the quarks mediated by the weak interaction. As a complex 3×3 matrix the CKM-matrix initially possess 18 independent parameters

but since all quark generations possess the same weak coupling constant the *CKM*-matrix is unitary, i.e.

$$V_{CKM} \cdot V_{CKM}^{\dagger} = \mathbb{1}\,, \tag{1.5}$$

so that the number of independent parameters is reduced to nine. Furthermore, by redefining the quark fields, five more parameters can be eliminated so that four independent physical quantities remain which are then identified as three mixing angles and one complex phase. As for the transition from particle to anti-particle the complex-conjugated *CKM*-matrix has to be considered, and the complex phase gives rise to the *CP*-violation since it changes its sign under complex conjugation. Due to this change the weak interaction differentiates between particle and anti-particle. Since the mixing between different quark families is a small effect, the *CKM*-matrix is roughly diagonal[3]

$$|V_{\mathrm{CKM}}| = \begin{pmatrix} 0.974\,20(21) & 0.2243(5) & 0.003\,94(36) \\ 0.218(4) & 0.997(17) & 0.0422(8) \\ 0.0081(5) & 0.0394(23) & 1.019(25) \end{pmatrix}. \tag{1.6}$$

Eq. (1.6) also shows that the *CKM*-matrix is strongly hierarchical with respect to the quark families, the matrix elements become smaller the further from the main diagonal they are, i.e. transitions between distant quark families become unlikely. Using the *Wolfenstein parametrization* (from L. Wolfenstein) the hierarchy of the *CKM*-matrix can be expressed by a parameter λ[19]:

$$V_{\mathrm{CKM}} = \begin{pmatrix} 1-\lambda^2/2 & \lambda & \lambda^3 A(\rho - i\eta) \\ -\lambda & 1-\lambda^2/2 & \lambda^2 A \\ \lambda^3 A(1-\rho-i\eta) & -\lambda^2 A & 1 \end{pmatrix} + \mathcal{O}(\lambda^4)\,, \quad \lambda \sim 0.22\,. \tag{1.7}$$

Here, η is the complex phase causing the *CP*-violation, which together with A, ρ and λ represent the four free parameters of the *CKM*-matrix. While an explanation of the strong hierarchy of the *CKM*-matrix is still to be given, the measurement of the matrix elements through weak decays allows one important check of the SM, i.e. the unitary. Given the unitary of the *CKM*-matrix, certain triangle relations between the matrix elements can be derived. Looking at Eq. (1.7) the relation

$$V_{ub}^* V_{ud} + V_{cb}^* V_{cd} + V_{tb}^* V_{td} = 0 \tag{1.8}$$

proves to be convenient, since this is the only relation where all terms have the same order of λ. Eq. (1.8) can now be represented as a triangle in the complex plane, shown in Fig. 1.1

The experimental measurement of the triangle elements allows to compare them with theoretical predictions providing a test of the SM and an important search for physics beyond the SM. The

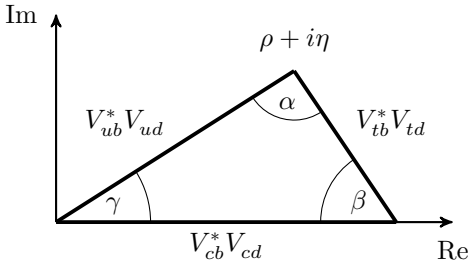

Figure 1.1: The unitarity triangle for Eq. (1.8).

investigation of the *CKM*-matrix elements is object of many research efforts. Since this work considers the semileptonic decays of heavy mesons, it can also be used for a more precise measurement of certain CKM matrix elements. For a better understanding of semileptonic decays of heavy mesons a discussion of QCD is in place. This follows in the upcoming section.

1.2 Quantum Chromodynamics and Hadrons

As mentioned in section 1.1 Quantum Chromodynamics (QCD) (greek: "chromos": color) is an essential part of the SM and as the gauge theory of strong interaction of special importance for the hadronic decays considered in this work. So in this section the theoretical background related to this work will be discussed. For a more complete and detailed review we refer to [20–22].

As already mentioned in section 1.1.1 QCD is the gauge theory of strong interactions. The first indication for the existence of the strong interaction was provided by the discovery of the nucleons by Rutherford (proton, 1917) and Chadwick (neutron, 1932). Since the proton is positively charged and the neutron does not carry electric charge, there had to be an additional force that could compensate the electrical repulsion and keep the atomic nucleus together. Even long before the introduction of the quark model, the existence of nuclear force was already postulated by H. Yukawa in 1935, who first affiliated it to an exchange of pions between the nucleons [23]. The exchange of these virtual quark-anti-quark-states is responsible for the long range part of the strong interaction, while later it turned out that the nuclear binding is a result of the coupling between the quarks and antiquarks to *gluons* (engl. "Glue"), the latter being the gauge bosons of the strong interaction.

During the development of the quark model the quarks were first postulated as a purely mathematical model, but deep inelastic scattering experiments during the 60's showed that the proton does indeed possess an inner structure. After this discovery, to describe the strong interaction theoretically Quantum Chromodynamics was designed as an $SU(3)$ gauge theory to theoretically describe the strong interaction. The degree of freedom for this symmetry group is the *color charge*. A quark is able to carry one of three possible colors (red, blue, green). The first hints at this

additional quantum number was the discovery of the Ω^- Hyperon in 1964 [24] which, based on the predictions of the quark model, should consist of three s-quarks all possessing the same spin configuration. But since quarks are fermions this would pose a violation of the Pauli principle. Similar problems occurred with other Baryons, so that in the following M. Han, Y. Nambu and O. Greenberg independently from each another postulated the existence of the color degree of freedom [25, 26]. An additional experimental evidence for the existence of color was provided by comparing the cross sections of e^+e^--scattering. The ratio of the cross sections for muon and hadron production

$$R = \frac{\sigma(e^+e^- \to \text{Hadrons})}{\sigma(e^+e^- \to \mu^+\mu^-)} \tag{1.9}$$

being measured, has a three times higher value than theoretically predicted, i.e. the production rate for colorless $q\bar{q}$-pairs is three times higher than anticipated, so that the color degree of freedom is needed. Not only this fact provides an experimental proof for the existence of color it also confirms the number of colors. So while the observation of the Ω^- Hyperon does not provide any hints towards the number of colors, the ratio of cross sections indicates the existence of exactly three colors. Furthermore, the quark model predicts the existence of an anti-color for every color which could be verified by the discovery of diverse mesons (e.g. J/Ψ). A detailed representation of the historical context and the associated experiments for the introduction of color can be found in [5].

As a theory QCD possesses three special properties

- *Asymptotic Freedom*: At the aforementioned deep inelastic scattering experiments it was observed that at very high energies and small distances quarks behave like free particles even though they are still bound in a hadronic state. This fact is known as *asymptotic freedom* and is attributable to the properties of the strong coupling constant(see sec. 1.2). Unlike in QED the coupling in QCD becomes weaker the smaller the distance between the particles is which in return means, that an infinite amount of energy is needed to separate two quarks. The asymptotic freedom was theoretically derived from QCD by D. Gross, F. Wilczeck and D. Ploitzer in 1973 [9, 27] and is hence considered proven in the framework of the SM.

- *Confinement*: The property that quarks and gluons can only be found in bound states and not as free particles is known as *confinement*. All observed hadrons are colorless. Up until now all experiments verify the confinement but theoretical proof in the framework of QCD is still to come.

- *Spontaneous breaking of the chiral symmetry*: In QCD, left- and right-handed quark fields couple in the QCD-vacuum. The vacuum expectation value of such a quark-anti-quark-pair $\langle 0|\overline{q}_L q_R + \overline{q}_R q_L|0\rangle$ is not equal to zero and hence breaks the chiral symmetry of massless QCD. The quark-anti-quark pairs form a *condensate* in the QCD vacuum. These condensates play an important role in the QCD sum rules.

Gauge Theory and Coupling of QCD

After discussing the theoretical background and introducing the basic properties of QCD, in this section we focus on the group theoretical aspects as well as perturbative calculations in QCD. Structurally, QCD and QED are similar in many ways but in this section a special focus will be put on the differences.

As mentioned before, QCD is based on a $SU(3)$ gauge group where the $SU(3)$ is a Lie group with the corresponding algebra. A special, unitary group of dimension N possesses N^2-1 generators. In case of QCD this corresponds to eight generators which in general are represented by the Gell-Mann matrices λ^a $(a = 1, ..., 8)$. Their representation is, for example, given in [21]. The generators satisfy the Lie-algebra

$$[\lambda_j, \lambda_k] = 2if_{jkl}\lambda_l\,, \tag{1.10}$$

with the totally anti-symmetric structure constant f_{jkl}. These generators can be identified with the eight gluon fields A^a_μ. In analogy to QED these gluon fields couple to all particles that carry color. There is an essential difference which can be explained by looking at the Yang-Mills-Lagrangian with an $SU(3)$ gauge group which in case for QCD is given by

$$\mathcal{L}_{\text{QCD}} = \bar{\psi}_i(i\gamma^\mu D_\mu - m)\psi_j - \frac{1}{4}G^a_{\mu\nu}G^{\mu\nu}_a\,, \tag{1.11}$$

where

$$\begin{aligned}
\psi &: \text{quark fields, } i,j = 1,2,3 \text{ color index}\,,\\
\gamma_\mu &: \text{dirac matrices}\,,\\
D_\mu = \partial_\mu - ig_sT_aA^a_\mu &: \text{covariant derivative}\,,\\
m &: \text{quark mass}\,,\\
g_s &: \text{coupling constant of strong interaction}\,,\\
T^a = \frac{\lambda^a}{2} &: \text{generator of } SU(3) \text{ gauge group (color matrix)}\,,\\
A^a_\mu &: \text{gauge boson (gluon) fields, } a = 1,..,8\,,\\
G^a_{\mu\nu} = \partial_\mu A^a_\nu - \partial_\nu A^a_\mu + g_sf^{abc}A^b_\mu A^c_\nu &: \text{gluon field strength tensor}\,.
\end{aligned}$$

Since QCD, in contrast to QED, is a *non-Abelian* gauge theory there is an additional term in the definition of the gluon field strength tensor $G^a_{\mu\nu}$ with the strong coupling g_s and the structure constant f^{abc}. The result of this is that the gauge bosons can strongly interact with each other. In

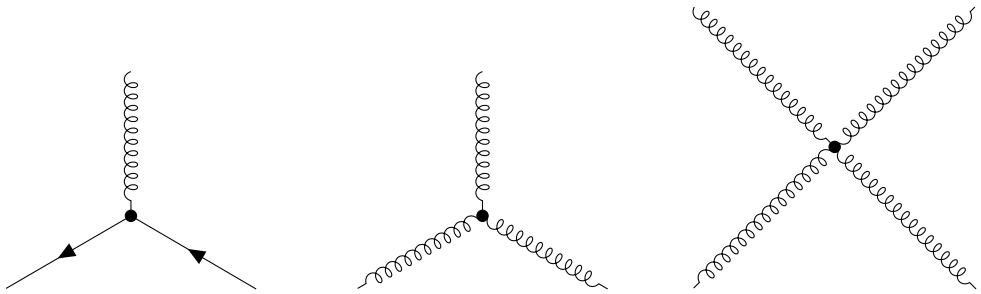

Figure 1.2: Vertices of QCD. Represented are the a) Quark-Gluon-vertex, b) 3-gluon-vertex and c) 4-gluon-vertex. The gluon-vertices b) and c) emerge as a consequence of the non-abelian gauge theory.

contrast to the photon, which is electrically neutral in QED, the gluon also carries a color charge so that in QCD there are additional fundamental vertices that include gluon-gluon interactions. These are shown in Fig. 1.2.

The additional self interactions are the main reason for the aforementioned asymptotic freedom but also hinder a consistent quantization, because the introduced gluon fields A^a_μ have four components while the massless gluon only possesses two polarizations. The remaining two degrees of freedom result in non physical contributions in perturbative calculations. These contributions can be dealt with by subtracting suitable scalar fields (*Faddeev-Popov-Ghost*). These ghost fields are of special importance for renormalizing the theory and are described in detail in [20]. A fundamental difference to QED arises from the couplings of the gauge bosons. Since gluons themselves carry color and anti-color, they can change their color by interacting with quark fields. Additionally, the self interactions result in a modified behavior in the couplings, i.e. they induce new diagrams in the renormalization of the gluon-propagator, as shown in Fig. 1.3.

The diagram c) in Fig. 1.3 represents a simple fermion-loop and results in an effective attenuation of the coupling, since, illustratively, the polarization of the vacuum results in a shielding of the charge. This is the reason why the coupling of QED shrinks at larger distances or smaller energies. In case of QCD the additional diagrams result in an amplification of the coupling resulting in the rise of the strong coupling dependent on the renormalization scale μ. For this reason, QCD cannot be treated perturbatively in case of long distances or small energies. Only a decrease in the coupling for large energies (asymptotic freedom) allows for a perturbative calculation in QCD. The scale dependent behavior of g_s (*running coupling*) will be discussed in the following section.

The hadronic bound states are invariant under $SU(3)_C$-transformations, so that all in all they are colorless. The easiest allowed combinations under these conditions for quark fields q^i with color indices i are quark-anti-quark states $\overline{q}^i q_i$, as well as three quark- $\epsilon^{ijk} q_i q_j q_k$ and three anti-quark

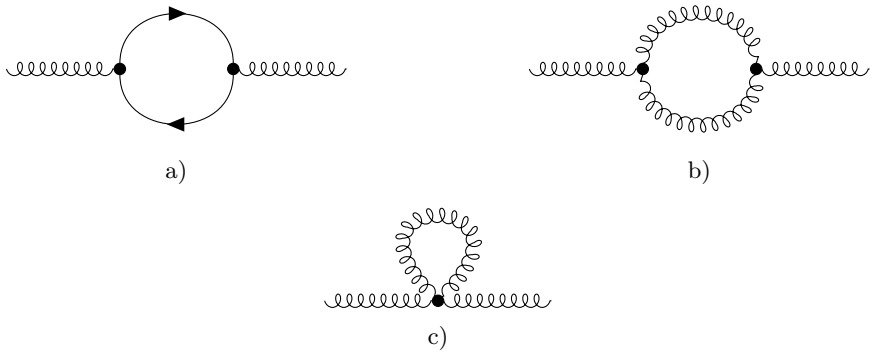

Figure 1.3: Leading order contributions to the renormalization of the gluon propagator. The contributions are as follows: a) loop contribution, b) gluon self energy and c) the *Tadpole* diagram.

states $\epsilon^{ijk}\overline{q}_i\overline{q}_j\overline{q}_k$. The former are known as *mesons* (Greek *meson*: the middle), while the latter are known as baryons (Greek *barys*: heavy). In comparison to other stable particles in the SM baryons possess a large mass, while meson states are heavier than the stable leptons but lighter than baryons. In principle, all possible flavors can be combined to a corresponding meson, except for the heavy top quark which, due to its short lifetime, decays before it can hadronize. In this work, mesons which contain a heavy quark (c, b), especially the c quark and a light quark (u, d, s) (*heavy-light-mesons*) are of special interest. These mesons are easily accessible by experiment and contain a heavy quark which is of interest in many applications. Additionally, many contributions can be expanded in terms of the light quark mass, due to $m_{u,d,s} \ll m_{c,b}$ and might be neglected altogether.

Scale Dependence of the Strong Coupling

In this section the scale dependence of the strong coupling will be illustrated. The scale dependence of the parameters in a theory is described by the corresponding *renormalization group equation* (RGE) which are differential equations that specify the μ-dependence for each parameter. A detailed derivation for this equation for the $\overline{MS}$-scheme (*modified minimal subtraction scheme*) can be found in [20]. For the coupling g_s the RGE has the form

$$0 = \mu \frac{d}{d\mu} g_{s,0}\,, \tag{1.12}$$

with

$$g_{s,0} = \left(\frac{\mu}{\mu_0}\right)^{\epsilon} Z_g(\mu) g_{s,R}\,, \tag{1.13}$$

where μ is the energy scale, μ_0 is a fixed mass scale, ϵ is the parameter used for the dimensional regularization, $g_{s,R}$ is the renormalized coupling and Z_g the corresponding renormalization constant. The bare, non renomalized coupling $g_{s,0}$ should not depend on μ so that its derivative vanishes. A point of note is that the μ and μ_0 dependent prefactor is a result of dimensional regularization where the coupling receives a mass dimension based on $g_s = g_{s,0}\mu_0^\epsilon$ and $g_{s,r} = g_{s,R}\mu^\epsilon$. In case of $\epsilon \to 0$ the couplings are massless, as usual. Replacing the bare coupling in Eq. (1.12) with the renormalized one the result reads

$$\mu \frac{dg_{s,R}}{d\mu} = \frac{dg_{s,R}}{d\ln\mu} = \beta(g_{s,R})\,, \tag{1.14}$$

with the Symanzik beta function determined by the coupling $g_{s,R}$

$$\beta(g_{s,R}) = -\epsilon g_{s,R} - \frac{\mu}{Z_g}\frac{dZ_g}{d\mu} g_{s,R}\,. \tag{1.15}$$

This beta function can be perturbatively expanded as

$$\beta(g_{s,R}) = -\beta_0 \frac{g_{s,R}^4}{(4\pi)^2} - \beta_1 \cdot \mathcal{O}(g_{s,R}^6) - \beta_2 \cdot \mathcal{O}(g_{s,R}^8) + ... \tag{1.16}$$

while taking note that the coupling $g_{s,R}$ is μ dependent. Eq. (1.16) shows that the behavior of the coupling depending on the scale μ (running coupling) up to first order is mainly influenced by the factor β_0. Turning to the calculation of β_0, Eq. (1.15) is considered and

$$Z_g = \frac{\tilde{Z}_1}{\tilde{Z}_3 Z_3^{1/2}}\,, \tag{1.17}$$

is used where $\tilde{Z}_1$ is the Gluon-Ghost-renormalization constant, $\tilde{Z}_3$ the Gluon-Ghost-self energy-renormalization constant and Z_3 the Gluon-self energy-renormalization constant. The ghost contributions are the Faddeev-Popov-ghost fields mentioned in sec. 1.2. The explicit form of these constants is given in [20]. The result for Z_g in leading order reads

$$Z_g = 1 - \frac{g_{s,R}^2}{4\pi}\frac{1}{\epsilon}\cdot\frac{1}{6}(11N_C - 2n_f) + \mathcal{O}(g_{s,R}^4)\,. \tag{1.18}$$

Here, n_f is the number of flavors and N_C the number of colors in an $SU(N)$ gauge theory. Inserting (1.18) in (1.15) and applying $N_C = 3$ for QCD the result reads as follows

$$\beta(g_{s,R}) = -\frac{1}{(4\pi)^2}\frac{33 - 2n_f}{3} g_{s,R}^3 + \mathcal{O}(g_{s,R}^5)\,, \tag{1.19}$$

so that

$$\beta_0 = 11 - \frac{2}{3} n_f \,. \tag{1.20}$$

An analogous calculation yields results for β_1 and β_2 and explicit values can for example be found in [20]. The behavior of the coupling in QCD can best be illustrated by looking at the parameter $\alpha_s(\mu) = g_s^2(\mu)/4\pi$. Inserting this in the differential equation (1.12) and solving the resulting equation, the behavior of the running coupling in leading order of QCD is obtained

$$\alpha_s(\mu) = \frac{\alpha_s(\mu_0)}{1 + \frac{\alpha_s(\mu_0)}{4\pi} \beta_0 \ln\left(\frac{\mu^2}{\mu_0}\right)} \,. \tag{1.21}$$

Several aspects are to be noted at this point. For one (1.21) contains a reference scale μ_0, which is identified as the energy scale where α_s is measured, i.e. to determine the running coupling an experimental measurement is necessary. On the other hand, (1.21) shows a central property of QCD, based on (1.20) β_0 is positive in QCD meaning that the complete beta function takes on a negative value. As a consequence the strength of the coupling decreases with rising energy, especially

$$\lim_{\mu \to \infty} \alpha_s(\mu) = 0 \,, \tag{1.22}$$

showing the *asymptotic freedom* of QCD. Conversely, with $\mu \to \Lambda_{\mathrm{QCD}}$ the characteristic QCD-scale Λ_{QCD} can be found as a Landau pole of the coupling. Λ_{QCD} marks the energy scale at which the coupling becomes large enough, so that quarks hadronize, additionally marking the point at which a treatment in perturbation theory is no longer possible. Experimentally its value was found to be around $\lambda_{\mathrm{QCD}} \simeq (200 - 300)\,\mathrm{MeV}$[2].

1.2.1 Leptonic and the simplest Semileptonic Decays of D-Mesons

In the SM the charged current leptonic and semileptonic processes at quark level are mediated by an exchange of a charged $W^{\pm}$ boson between a quark and a lepton current. The purely leptonic decay, shown in Fig. 1.4a, is only possible for the charged D-meson and is realized by the annihilation of the quark and anti quark within the meson into a virtual W boson. From a theoretical point of view these decays are easy to deal with since no hadrons appear in the final state. The decay rate at leading order is given by

$$\Gamma(D \to \ell \nu_\ell) = \frac{G_F^2}{8\pi} f_D^2 |V_{cd}|^2 m_\ell^2 \left(1 - \frac{m_\ell^2}{m_D^2}\right)^2 \,, \tag{1.23}$$

where m_D is the charged D-meson mass, m_ℓ the mass of the final lepton, $|V_{cd}|$ the CKM matrix element and f_D the decay constant of the D-meson. The decay rate shows that the only hadronic

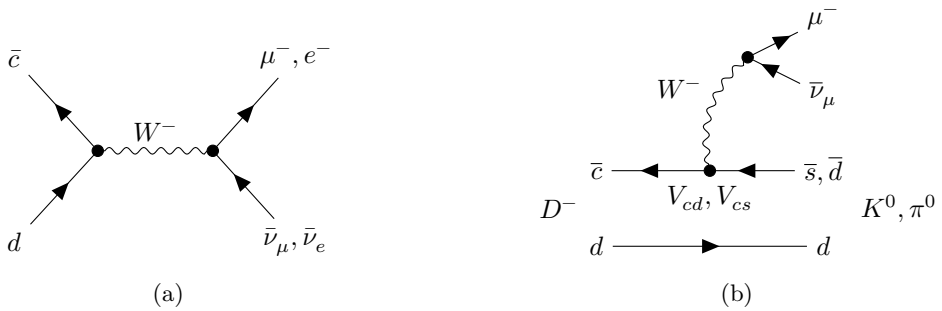

Figure 1.4: Feynman diagrams showcasing a) a leptonic D-decay and b) a semileptonic D-decay.

input in a purely leptonic decay is given by the decay constant, more details on the decay constant are given in [28]. The factor m_ℓ^2 reflects the helicity suppression due to the left handedness of the the charged current in the SM.

Turning to semileptonic decays of charm mesons, at quark level these are mediated by the semileptonic decay of the charm quark $c \to q\ell^+\nu_\ell$, shown in Fig. 1.4b, where $q = d, s$. The resulting quark combines with the initial light antiquark to form final hadrons. As mentioned before, leptons do not interact strongly and can hence be factored out in the amplitude of the semileptonic process

$$\mathcal{M} = \frac{G_F}{\sqrt{2}} V_{cq}^* \bar{\nu}\gamma_\mu(1-\gamma_5)\ell \, \langle X|\bar{q}\gamma^\mu(1-\gamma_5)c|D\rangle \tag{1.24}$$

where all strong interactions are included in the hadronic matrix element $\langle X|\bar{q}\gamma^\mu(1-\gamma_5)c|D\rangle$. Given that the amplitude depends on the CKM-matrix element V_{cq}, as well as the hadronic matrix element, semileptonic charm decays are a good test ground for both the study of quark mixing and testing theoretical techniques for calculating the hadronic matrix element. As mentioned at the beginning the hadronic matrix element can be decomposed into several form factors according to its Lorentz structure. In general the form factors are governed by non-perturbative dynamics, i.e. perturbative QCD can not be applied directly. Nonetheless, several methods were developed for the calculation of the transition form factors.

1.2.2 Inclusive decays of charmed mesons

As mentioned above, the focus of this work lies with the inclusive semileptonic decays of the charm meson and we focus on presenting and applying the method of lattice QCD for this decay mode. The inclusive decay can be visualized in a similar way to the diagram shown above in Fig. 1.4b, and we show one possible diagram in 1.5. Here, we show the inclusive semileptonic decay of a D_s meson into any final state containing an s quark, denoted by X_s.

This work will focus on a newly developed method and treating inclusive decays by employing

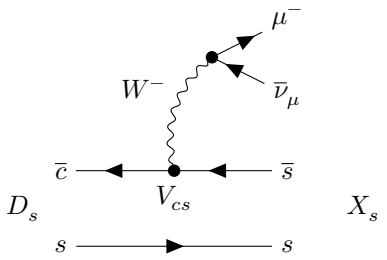

Figure 1.5: Feynman diagrams showcasing the inclusive semileptonic decays of the D_s meson.

lattice QCD [29], to obtain predictions for the CKM matrix elements. Further discussion on how lattice theory is applied on these types of decays can be found in Ch. 3. This section will focus on the current status on currently available strategies on treating inclusive decays, and why the inclusive decays pose an interesting field of study. Let us give the reason to the latter first.

The inclusive sector is interesting due to a recent discrepancy discovered in experimental determination of CKM parameters V_{cb} and V_{ub} between exclusive and inclusive determinations [30]. This provides both, theorists and experimentalists alike, with a chance and the task to obtain a better understanding of these decays. The attentive reader will have realized that our focus lies on the treatment of the inclusive decays of charmed meson, while the aforementioned discrepancy was observed in the bottom sector. The reason for this pertains to challenges in the treatment of the bottom sector specific to lattice QCD, i.e. the large discretization effects expected for m_b, as well as the challenge of simulating the physical bottom quark mass on the lattice. This is why this work will focus on the charm sector, not only to verify the validity of the proposed method, but also since the formalism developed and discussed in this work can be straightforwardly applied to the bottom sector.

Analytical treatment of inclusive decays

As a preface to this work, we will shortly discuss currently available analytical techniques for inclusive semileptonic decays from the theory perspective. In this section we will briefly introduce the operator product expansion (OPE) in heavy quark effective field theory (HQET). We are not able to give a full review on this topic here, so we refer the interested reader to [31–37] for a more complete review.

The general idea is to employ a double expansion in α_s and inverse powers of m_Q, where Q denotes the heavy quark. It is important to mention, that while heavy quark expansion is a very powerful tool, and has been applied to the bottom sector with great success [38, 39], it remains an open question on whether similar success can be achieved in the charm sector, since the expansion parameters $\alpha_s(m_c)$ and $1/m_c$ are larger compared to the bottom case. Generally

speaking, depending on the masses of the initial state heavy quark Q and the final state quark q, it is possible to distinguish four cases

1. $m_Q \sim m_q \gg \Lambda_{\mathrm{QCD}}$
2. $m_Q \gg m_q \gg \Lambda_{\mathrm{QCD}}$
3. $m_Q \gg m_q \sim \Lambda_{\mathrm{QCD}}$
4. $m_Q \gg \Lambda_{\mathrm{QCD}} \gg m_q$

The $c \to s$ transition considered in this work would correspond to 3., since in this case we have $m_s \sim \Lambda_{\mathrm{QCD}}$. In this case, a third expansion parameter, in addition to α_s and $1/m_c$, has to be considered, i.e. $m_s/m_c \sim 1/12$. More details on the different cases, as well as how the third expansion parameter has to be treated in the HQE can be found in [40].

For now, let us consider a generalized version of the decay showcased in Fig. 1.5

$$H(p_H = m_H v) \to X(p_X) + \ell(k) + \nu_\ell(k')\,, \tag{1.25}$$

where we consider some heavy hadronic state H carrying momentum p_H in the initial state decaying into a hadronic state X carrying momentum p_X with a lepton, neutrino pair carrying momenta k and k', respectively. For this type of inclusive decay the differential decay rate in the rest frame of the initial heavy hadron is given by

$$d\Gamma = \frac{G_F^2}{4m_H}|V_{Qq}|^2 W_{\mu\nu}(k+k', v) L^{\mu\nu} d(\mathrm{PS})\,, \tag{1.26}$$

where $W_{\mu\nu}$ and $L^{\mu\nu}$ are the hadronic and leptonic tensors, respectively, k and k' are the momenta of the final state lepton and neutrino, and $d(\mathrm{PS})$ is a short-hand notation for the phase-space integral defined as

$$d(\mathrm{PS}) = \int \tilde{dk}\tilde{dk}'\,\delta(\text{observables})\,, \quad \tilde{dk} = \frac{d^4k}{(2\pi)^3}\delta(k^2 - m_\ell^2)\Theta(k_0)\,, \tag{1.27}$$

where $\delta(\text{observables})$ is used to denote the observables that are to be considered. The hadronic tensor $W_{\mu\nu}$ can be decomposed into Lorentz invariant form factors reducing the dependencies to only two invariants, which for convenience sake are generally chosen to be $q^2 = (p_X - p_H)^2$ and vq, where $v = p_h/m_H$ is the four-velocity of the initial hadron. These form factors can be related to the discontinuity of the form factors defining the time-ordered product $T_{\mu\nu}(q, v)$. For the time-ordered product we can define two cuts in the complex vq frame for a fixed value of q^2, which we show in Fig. 1.6 and highlight the cuts by representing them as thick lines. We have a physical cut extending

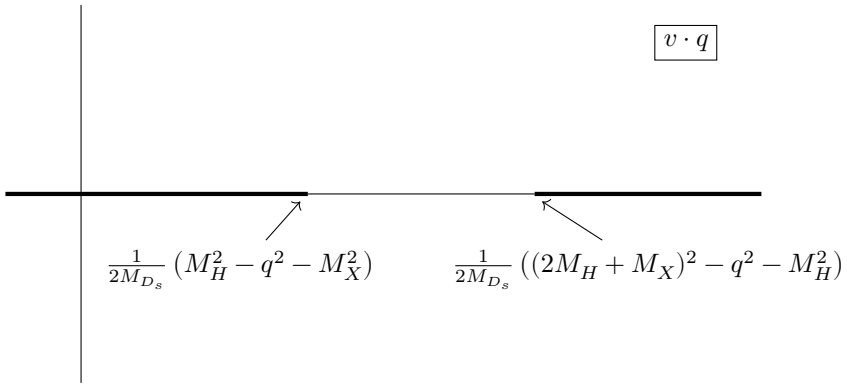

Figure 1.6: Cuts in the complex vq plane for the time-ordered product. The cuts are represented by the thick lines. The cut on the left corresponds to the physical $Q \to q$ decay, while the right one represents the unphysical $Q \to \bar{q}QQ$ decay.

along the real axis

$$\sqrt{q^2} < vq < \frac{1}{2M_{D_s}}\left(M_H^2 - q^2 - M_X^2\right) , \tag{1.28}$$

as well as a second cut extending along the real axis

$$vq < \frac{1}{2M_{D_s}}\left((2M_H + M_X)^2 - q^2 - M_H^2\right) . \tag{1.29}$$

Here, m_H denotes the mass of the lightest hadronic state. The physical process (1.25) is possible only parts of the region defined by (1.28), while the region defined through (1.29) correspond to the unphysical process $Q \to \bar{q}QQ$.

It is important to remark that there exists a problematic region in the phase space, i.e. when the invariant mass of the final state hadron approaches m_H, since we expect large corrections to perturbative QCD due to the dominance of resonant states for this case. To circumvent this problem it is possible to consider a smooth average over some portion of the cut. This kind of average can be achieved by introducing a suitable weight function and then perform a contour integration in the complex vq plane of $T_{\mu\nu}$ and the weight function. The contour is defined such that it encircles the physical cut in a way as to specifically pick out the discontinuity $T_{\mu\nu}$ of the cut. We skip the details of the calculation and refer the interested reader to [35]. We will only conclude that it is possible to avoid the dangerous region proportional to a distance which is large compared to Λ_{QCD}.

Keeping the preceding discussion in mind, we can now write down the relation

$$W_{\mu\nu}(q, v) = 2\mathrm{Im}T_{\mu\nu}(q, v) , \tag{1.30}$$

with $q = p_H - p_X$, relating the hadronic tensor with the perturbatively calculated time ordered product $T_{\mu\nu}$, defined as

$$T_{\mu\nu}(q,v) = \int dx^4 \, \langle H(v)| \left[\left(\bar{Q}(x)\gamma_\mu(1-\gamma_5)q(x) \right) \left(\bar{q}(0)\gamma_\nu(1-\gamma_5)Q(0) \right) \right] |H(v)\rangle \ . \tag{1.31}$$

Here, Q and q denote the heavy and light quark fields constituting the initial heavy hadron, respectively, while $H(v)$ defines the initial hadronic state with four-velocity v. Even though it is possible to expand (1.31) in a sum of local operators, it is convenient to switch to an effective theory, to entangle long and short distance contributions. This essentially results in a rescaling of the heavy hadron momentum, and the relevant variable will be the hadronic momentum transfer $\mathcal{Q} = q - m_Q v$, which is assumed to be the only large scale in our problem. In this effective theory, the OPE is then an expansion in inverse powers of $\mathcal{Q}^2$.

Going forward, by switching to an effective theory, we scale out the large parameter m_H and the residual momentum $k = P_H - m_Q v$ becomes our characterizing variable for the initial state. From here on, to obtain the inclusive decay rate, we define the OPE for the projection of $T_{\mu\nu}$

$$T(k,k',v) = T_{\mu\nu} L^{\mu\nu} \, . \tag{1.32}$$

The OPE up to dimension five operators at tree level can written as

$$\begin{aligned}
T(k,k',v) = & \left(\frac{1}{\mathcal{Q}^2 - m_l^2 + i\epsilon} \right) 64 (k'\mathcal{Q}) \bar{h}_v \not{k} (1-\gamma_5) h_v \\
& + \left(\frac{1}{\mathcal{Q}^2 - m_l^2 + i\epsilon} \right) 64 \bar{h}_v (ik'D) \not{k} (1-\gamma_5) h_v \\
& - \left(\frac{1}{\mathcal{Q}^2 - m_l^2 + i\epsilon} \right)^2 128 (k'\mathcal{Q}) \bar{h}_v (i\mathcal{Q}D) \not{k} (1-\gamma_5) h_v \\
& - \left(\frac{1}{\mathcal{Q}^2 - m_l^2 + i\epsilon} \right)^2 64 (k'\mathcal{Q}) \bar{h}_v (iD)^2 \not{k} (1-\gamma_5) h_v \\
& - \left(\frac{1}{\mathcal{Q}^2 - m_l^2 + i\epsilon} \right)^2 64 \bar{h}_v [(i\mathcal{Q}D), (ik'D)] \not{k} (1-\gamma_5) h_v \\
& - \left(\frac{1}{\mathcal{Q}^2 - m_l^2 + i\epsilon} \right)^2 64 \epsilon_{\lambda\alpha\beta\rho} \mathcal{Q}^\lambda k'^\rho \bar{h}_v (iD^\alpha)(iD^\beta) \not{k} (1-\gamma_5) h_v \\
& - \left(\frac{1}{\mathcal{Q}^2 - m_l^2 + i\epsilon} \right)^2 128 \bar{h}_v (ik'D)(i\mathcal{Q}D) \not{k} (1-\gamma_5) h_v \\
& + \left(\frac{1}{\mathcal{Q}^2 - m_l^2 + i\epsilon} \right)^3 256 (k'\mathcal{Q}) \bar{h}_v (i\mathcal{Q}D)^2 \not{k} (1-\gamma_5) h_v \\
& + \text{Dimension six or higher operators} \, .
\end{aligned} \tag{1.33}$$

In the equation above, h_v denotes the static heavy quark field and D denotes the covariant derivative.

Finally, it is now possible to write the differential decay rate in terms of the imaginary part of the forward matrix element of the operator T

$$d\Gamma = \frac{G_F^2}{4m_H}|V_{Qq}|^2 \left(2\mathrm{Im}\,\langle H(v)|T(k,k',v)|H(v)\rangle\right) d(\mathrm{PS})\,. \tag{1.34}$$

We can now turn towards a discussion on the relevant operators in a general framework up to $\mathcal{O}(m_Q^{-2})$ where we consider the rest frame of the heavy hadron H, i.e. we set $v = (1,0,0,0)$. The matrix element for the leading operator of dimension three

$$\bar{h}_v h_v\,, \tag{1.35}$$

is fixed by

$$\langle H(v)|\bar{h}_v h_v|H(v)\rangle = 2m_H\,. \tag{1.36}$$

Following the arguments from [35, 40], we have no contributions of dimension four operators in the case considered here. Going forward, we have two dimension five operators

$$O_G = \frac{i}{2}\bar{h}_v \sigma^{\mu\nu} G_{\mu\nu} h_v \tag{1.37}$$

$$O_M = \bar{h}_v (-i\vec{D})^2 h_v\,, \tag{1.38}$$

where $\sigma^{\mu\nu} = 1/2(\gamma^\mu\gamma^\nu - \gamma^\nu\gamma^\mu)$ and $G_{\mu\nu} = gG^q_{\mu\nu}T^\mu$ is the gluon field strength tensor. The corresponding matrix elements are generally given by

$$\frac{1}{2m_H}\langle H(v)|\bar{h}_v \frac{i}{2}\sigma^{\mu\nu}G_{\mu\nu}h_v|H(v)\rangle = \mu_G^2\,, \tag{1.39}$$

$$\frac{1}{2m_H}\langle H(v)|\bar{h}_v (i\vec{D})^2 h_v|H(v)\rangle = \mu_\pi^2\,. \tag{1.40}$$

At this point it is now possible to insert the OPE into (1.34) and perform the phase space integration to arrive at [32]

$$\Gamma = \frac{G_F^2 m_Q^5 |V_{Qq}|^2}{192\pi^3}\left[z_0\left(1 + \frac{1}{2}(G_h - K_h)\right) - 2z_1 G_h\right]\,, \tag{1.41}$$

where we used the following definitions

$$\begin{aligned} z_0 &= 1 - 8\rho + 8\rho^3 - \rho^4 - 12\rho^2 \log\rho \,, \\ z_1 &= (1-\rho)^4 \,, \\ \rho &= \frac{m_q}{m_Q} \,, \\ G_h &= \frac{\mu_G^2}{m_Q^2} \,, \\ K_h &= \frac{\mu_\pi^2}{m_Q^2} \,. \end{aligned} \tag{1.42}$$

We will stop our discussion at this point, having presented a general expression for the total decay rate and refer to [41] for a discussion on the relevant operators for the $c \to s$ transition and [42] for the corresponding application in the bottom sector.

But while OPE provides a strong method to obtain predictions in an analytical framework, it is still desirable to have full control over systematic effects. This condition is satisfied by lattice QCD, able to give precise prediction based solely on first principles and being systematically improvable through more computational resources. Let us conclude this section by mentioning that there are more methods available towards treating non perturbative QCD, such as QCD sum rules [28, 43–45] and light-cone sum rules[46–48]. And while all these methods are complementary to each other, an extensive study and a comparison between them goes beyond the scope of this work. We will hence point towards the corresponding references for the interested reader.

The rest of this work is structured as follows. In Chapter 2 we present a short introduction into the field of lattice QCD, presenting a short review on important techniques and developments in the field. This is followed by a discussion on the extension of lattice QCD towards inclusive decays in Chapter 3, where we will introduce all the necessary ideas, techniques, as well as notations needed to analyze inclusive decays using hadron correlators obtained from lattice simulations. This chapter will also introduce the challenges that have to be overcome to obtain reliant estimates on the systematic errors, with a special focus on the systematic error induced due to finite volume effects. In chapter 4 we show our numerical results, before summarizing and discussing our results in chapter 5 where we also include a discussion on the future development and prospects of this work.

Chapter 2

Introduction to Lattice Field Theory

As mentioned above, in recent years lattice QCD has become a standard tool in treating quarks and gluons, since it provides a systematically improvable way for fully non-perturbative calculations which do not rely on any perturbative expansions. Since its proposal by Wilson in 1974 [49], lattice QCD has produced a lot of outstanding results. Following the Monte Carlo simulation of pure SU(2) gauge theory by Creutz [50], a myriad of computational methods and algorithms have been introduced, with recent lattice studies becoming more realistic and reliable, yielding a better understanding of the underlying non-perturbative nature of QCD.

To perform lattice studies on low-energy hadron, a consistent formulation for fermions is necessary. The naive approach of simply replacing the derivatives of the continuum theory by discrete differences however, does not yield the desired results. This is due to the fact that these naive fermions posses undesired poles, generally referred to as *doublers*. Wilson introduced a counter term in the formulation of the action which removes the doublers, although this formulation breaks chiral symmetry. Employing these so-called *Wilson fermions* the hadron masses were computed from lattice QCD simulations in 1981 [51, 52].

New problems arise when dynamical quarks are included in lattice simulations, since those quarks require the calculation of the determinant of the Dirac operator which is computationally challenging. Early studies of this field relied on the *quenched approximation*, ignoring the effect of sea quarks. Additionally, several methods, such as Hybrid-Monte-Carlo [53] or R-algorithm [54], were proposed to deal with this problem. In recent years, the development of computational resources allows state-of-the-art lattice simulations to run simulations involving the dynamical light quarks.

One success of lattice QCD is the prediction of the hadron mass spectra. To be able to compare lattice results with their experimental counterpart, it is necessary to perform the continuum

extrapolation, take the infinite volume limit and perform an extrapolation towards the physical quark masses. These requirements have been fulfilled using Wilson fermions in quenched QCD and their results are reported in, e.g. [55–57]. The limit of the quenched approximation is indicated in [57], where the deviation between the mass spectra from lattice and experimental determination is at most 11 %. A proper reproduction of the mass spectra was accomplished by the BMW Collaboration [58], where they employed Wilson fermions with dynamical u, d and s quarks. The errors on their predictions of the spectra were in the region of percents, with the exception of the Δ baryon, and were in generally good agreement with experiment. This success indicated the key role of lattice QCD in the search for New Physics.

In the treatment of QCD, one important property is chiral symmetry and it would hence be desirable to preserve this property on the lattice. In 1981, Ginsparg and Wilson formulated the lattice version of chiral symmetry, nowadays known as the Ginsparg-Wilson relation [59]. Following this relation, many formulations of lattice fermions were discovered in the 1990s, such as domain-wall fermions [60, 61] and overlap fermions [62–64]. Currently, these fermion formulations are used extensively in actual simulations where chiral symmetry plays a significant role.

This chapter focuses on an overview on lattice field theory and is structured in the following way. Following the review of QCD in the continuum theory of the previous chapter, here we start with an introduction on the implementation of gauge action into Euclidean spacetime in sec 2.1, followed by the introduction of the gluon action on the lattice in sec. 2.2. This is then followed by an introduction into the fermion implementation onto the lattice in sec. 2.3. After introducing these basic tools, we then shift our focus on the calculation of meson correlators in sec. 2.4. We follow this discussion by introducing the fermion formulation employed in this work, i.e. the Möbius domain-wall formulation for fermions, in sec. 2.5. Finally, we alo discuss the renormalization of lattice operators, as well as the PCAC relation in sections 2.6 and 2.7, respectively.

In the scope of this work we cannot hope to achieve a complete and satisfying overview over the complex topic that is lattice field theory, so we refer to [65–67] for more detailed and complete overviews.

2.1 The Euclidean action

Following our introduction we shall now begin our discussion into the implementation of QCD onto the lattice. When we turn our focus towards measurements in lattice QCD, we have to discuss the Euclidean path integral. The general idea is to introduce Euclidean time and then identify the phase-space factor $\exp(iS)$ as the Boltzman weight, to enable the application of techniques of statistical mechanics for lattice QCD in Euclidean spacetime.

We first start with a discussion of the gauge action in Euclidean spacetime. For brevity, we

introduce the short-hand notation of the gauge field introduced in (1.11)

$$gA_\mu(x) \to A_\mu(x)\,, \tag{2.1}$$

to be used in the following. Furthermore, after applying a Wick rotation

$$x_0 \to -ix_4\,, \quad A_0 \to iA_4\,, \tag{2.2}$$

the components of the field strength tensor and the Euclidean action are given by

$$G^a_{\mu\nu} \equiv \partial_\mu A^a_\nu - \partial_\nu A^a_\mu - f^{abc} A^b_\mu A^c_\nu\,, \tag{2.3}$$

and

$$S_G = \frac{1}{g^2}\int d^4x\, G^a_{\mu\nu} G^a_{\mu\nu}\,, \tag{2.4}$$

respectively, where μ and ν run from 1 to 4.

Going forward, we now consider the Euclidean action for quark fields. In Euclidean space the γ matrices fulfill the anti-commutation relations

$$\{\gamma_\mu, \gamma_\nu\} = 2\delta_{\mu\nu}\,. \tag{2.5}$$

The fermionic action is given by

$$S_F = \sum_{q=u,d,s,\ldots} \int d^4x\, \bar{q}(\not{D} + m_q)q\,, \tag{2.6}$$

with the redefined covariant derivative

$$D_\mu = \partial_\mu - iA^a_\mu \frac{\lambda_a}{2}\,. \tag{2.7}$$

By employing the Euclidean action a bridge between the path integral in quantum field theory and statistical mechanics is build. The phase appearing in the path integral is replaced by the Boltzman weight in the Euclidean space

$$\exp(iS_{QCD}) \to \exp(-S_{QCD})\,, \tag{2.8}$$

where $S_{QCD} = S_G + S_F$ defines the action of QCD in Euclidean space. Using this notation, the

vacuum expectation value of a physical quantity O is defined through

$$\langle O \rangle = \frac{1}{Z} \int D\bar{\psi} D\psi DA e^{-S_{QCD}} O \,, \tag{2.9}$$

where

$$Z \equiv \frac{1}{Z} \int D\bar{\psi} D\psi DA e^{-S_{QCD}} \,. \tag{2.10}$$

is the partition function. This path integral formulation can be related to statistical mechanics. Therefore, numerical techniques, such as Monte Carlo methods, can be applied, and in the following sections we discuss lattice QCD computations employing the Euclidean path integral.

2.2 Formulation of gluons in lattice QCD

After introducing the Euclidean action, our next step is to take a look at the different contribution constituting to this action. We first focus on the discussion on the gluonic part of the action. To this end, we start by introducing link variables

$$U_\mu(x) \equiv e^{iagA_\mu(x)T_c} \,, \tag{2.11}$$

where a is the lattice spacing, g is the coupling constant and T_c is the generator of the gauge group. Let us now consider the so-called *plaquette*, i.e. a closed loop of these link variables

$$U_{\mu\nu}(x) = U_\mu(x) U_\nu(x+\hat{\mu}) U_\mu^\dagger(x+\hat{\nu}) U_\nu^\dagger(x) \,, \tag{2.12}$$

where $\hat{\mu}$ and $\hat{\nu}$ are unit vectors in a $\mu - \nu$ plane. In Figure 2.1 we illustrate the link variable and the plaquette. In the continuum limit, i.e. $a \to 0$, this plaquette approaches the field strength tensor $G_{\mu\nu}(x)$

$$U_{\mu\nu} \overset{a\to 0}{\to} \exp\left(ia^2 G_{\mu\nu}(x) + \mathcal{O}(a^4)\right) \,. \tag{2.13}$$

It is hence possible to construct the gauge action in terms of the plaquettes as

$$S_G = \frac{\beta}{3} \sum_x \sum_{\mu<\nu} \mathrm{Re}\,\mathrm{Tr}\left[\mathbb{1} - U_{\mu\nu}(x)\right] \,, \tag{2.14}$$

introducing the inverse coupling $\beta = 1/g^2$ which is conventionally used to replace the standard coupling constant. The action introduced in (2.14) is known as the Wilson action and, up to

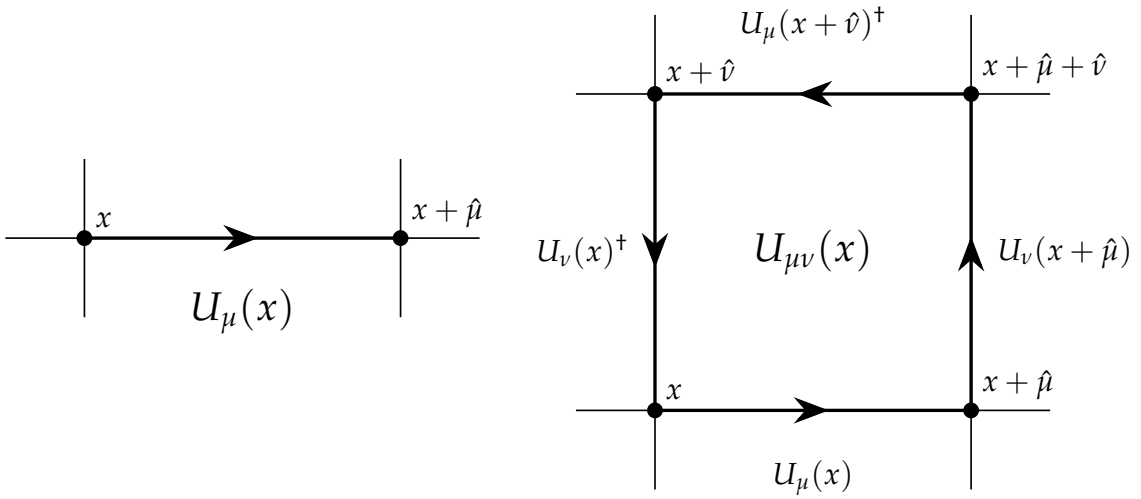

Figure 2.1: Visualization of the link variable $U_\mu(x)$ on the l.h.s and plaquette $U_{\mu\nu}(x)$ on the r.h.s. .

discretization effects, reproduces the correct continuum limit

$$S_G \simeq \frac{1}{4g^2} \int d^4x \, G^a_{\mu\nu} G^a_{\mu\nu} \,. \tag{2.15}$$

To obtain better control over the discretization error, contributions from other loops, such as rectangles and parallelograms, can be considered in the construction of (2.14) [68]. An important tool in controlling discretization effects is the Symanzik effective theory [69, 70] where the correction terms of the discretized action are identified with their corresponding terms in the continuum limit. To achieve cancellation up to a desired order, the basic idea is to add a discretized expression to the action, so that the correction terms in the continuum limit are cancelled up to that order. A toy example as well as an application to Wilson's gauge action can be found in [65]. For the small a expansion, discretization effects are limited by symmetries on the lattice and the fact that dimension-five operators do not contribute. In consequence this means that the leading $\mathcal{O}(a^2)$ corrections are controlled by dimension-six operators. In this work, we employ the tree-level Symanzik improved gauge action, containing the rectangular terms so that the leading corrections are of the order $\mathcal{O}(\alpha_s a^2)$

2.3 Lattice QCD formulation of fermions

Following the discussion of the gluonic part of the action, we shall now focus on the fermionic part and the corresponding challenges that accompany the introduction of fermions onto the lattice and

their treatment. For notational convenience this section is limited to the single-flavor case, with an extension to the multi flavor case being straightforward.

For starters, let us consider the discretization of the Dirac operator of the QCD action. On the lattice, the continuum partial derivative is replaced by a discrete finite-difference

$$\partial_\mu \psi(x) \to \frac{\psi(x+\hat{\mu}) - \psi(x-\hat{\mu})}{2a}\,. \tag{2.16}$$

It now becomes obvious that the term $\bar{\psi}\gamma_\mu\psi(x+\hat{\mu})$, appearing in the fermion action, breaks gauge invariance. To solve this problem and restore the gauge invariance of the lattice action, the link variables $U_\mu(x)$ can be introduced and the so-called naive fermion action

$$S_F = a^4 \sum_x \left[\frac{1}{2a} \bar{\psi}(x)\gamma_\mu \left(U_\mu(x)\psi(x+\hat{\mu}) - U_\mu(x-\hat{\mu})^\dagger \psi(x-\hat{\mu}) \right) + m\bar{\psi}(x)\psi(x) \right] \tag{2.17}$$

can be constructed. This expression is consistent with (2.6) up to the leading order in the small a expansion. On the other hand, against the naive assumption that this expression would give rise to the correct continuum limit, the naive fermion approach does not reproduce the correct limit.

This can be shown by considering a well-known problem of the naive fermion action. To this end, let us consider the simplest example of free lattice fermions. Let us now consider the Fourier transform of the Dirac operator

$$\tilde{D}(p) = m\mathbb{1} + \frac{i}{a}\sum_\mu \gamma_\mu \sin(p_\mu a)\,, \tag{2.18}$$

as well as its inverse, i.e. the quark propagator, given by

$$\tilde{D}^{-1}(p) = \frac{m\mathbb{1} - ia^{-1}\sum_\mu \gamma_\mu \sin(p_\mu a)}{m^2 + a^{-2}\sum_\mu \sin^2(p_\mu a)},. \tag{2.19}$$

In the massless limit, the denominator in (2.19) vanishes for $p_\mu = 0$ or π/a. This results in unphysical poles except for the one at $p_\mu = (0,0,0,0)$. The total number of these unphysical poles is 15 and they are generally called *doublers*. To obtain proper predictions of physical quantities from lattice QCD these doublers have to be removed.

Removing the doublers is achieved by introducing the Wilson term in the Dirac operator to make the doublers irrelevant in the continuum limit

$$\tilde{D}(p) = m\mathbb{1} + \frac{i}{a}\sum_\mu \gamma_\mu \sin(p_\mu a) + \mathbb{1}\frac{1}{a}\sum_\mu \left(1 - \cos(p_\mu a)\right)\,. \tag{2.20}$$

The additional term gives a correction for higher orders in the small a expansion

$$\frac{1}{a}\sum_{\mu}\left(1-\cos(p_\mu a)\right) = \frac{a}{2}\sum_{\mu} p_\mu^2 + \mathcal{O}(a^3)\,, \tag{2.21}$$

corresponding to the discretization of the quadratic derivative $\partial_\mu\partial_\mu$. It is obvious that the Wilson term vanishes for $p_\mu = (0,0,0,0)$, while leading to an additional mass term for the doublers

$$m + \frac{2l}{a}\,, \tag{2.22}$$

where l is the number of the momentum components $p_\mu = \pi/a$. This additional mass results in a decoupling of the doublers in the continuum theory since in the continuum limit, i.e. $a \to 0$, the masses of the doublers become substantially large.

We now return our focus to the Dirac operator treating the gauge interaction in position space. In this scenario, the Wilson term is given by

$$-\frac{1}{2a}\sum_{\mu}\left(U_\mu(x)\delta_{x+\hat{\mu},y} - 2\delta_{x,y} + U_\mu^\dagger(x-\hat{\mu})\delta_{x-\hat{\mu},y}\right)\,. \tag{2.23}$$

Furthermore, the fermionic action of the Wilson fermions is given by

$$S_F = a^4\sum_{x,y}\bar{\psi}(x)D_W(x|y)\psi(y)\,, \tag{2.24}$$

where the Wilson-Dirac operator $D_W(x|y)$ is defined through

$$D_W(x|y) = \left(m+\frac{4}{a}\right)\delta_{x,y} - \frac{1}{2a}\sum_{\mu}(\mathbb{1}-\gamma_\mu)U_\mu(x)\delta_{x+\hat{\mu},y} - \frac{1}{2a}\sum_{\mu}(\mathbb{1}+\gamma_\mu)U_\mu^\dagger(x-\hat{\mu})\delta_{x-\hat{\mu},y}\,. \tag{2.25}$$

An important point to notice here is that the Wilson fermion action explicitly breaks chiral symmetry, even in the massless limit $m \to 0$. Chiral symmetry of the fermion action, in the continuum limit, can be written as

$$D\gamma_5 + \gamma_5 D = 0\,, \tag{2.26}$$

which is fulfilled in the case of $D = \gamma_\mu(\partial_\mu + iA_\mu)$. This is not the case for the Wilson term given in (2.23) as it does not anti-commute with γ_5 since it is proportional to $\mathbb{1}$. This breaking of the chiral symmetry as well as the appearance of doublers are inseparately connected to each other. Based on the Nielson-Ninomiya theorem [71, 72], it is impossible to conserve chiral symmetry in lattice theory without the appearance of doublers, giving rise to the limitation of lattice QCD, especially in the case of physics strongly related to chiral symmetry.

On the lattice, it is expected that the relation (2.26) is modified by $\mathcal{O}(a)$ and based on a renormalization group transformation, Ginsparg and Wilson [59] proposed the modified relation

$$D\gamma_5 + \gamma_5 D = aD\gamma_5 D\,. \tag{2.27}$$

In this relation the Dirac operator does not anti-commute with γ_5 by introducing an additional term on the r.h.s.. Furthermore, this additional term on the r.h.s vanishes in the continuum limit, recovering chiral symmetry. The relation (2.27), commonly referred to as the Ginsparg-Wilson relation, hence defines the lattice version of chiral symmetry.

The Ginsparg-Wilson relation can be satisfied by several formulations of the fermion action. One such action is the overlap formulation [62, 73–75], which has been explicitly shown to satisfy the Ginsparg-Wilson relation [63]. In this work we focus on the domain-wall formulation [60, 61] of fermions and refer the interested reader to [65] for different approaches. The domain-wall formulation obeys the Ginsparg-Wilson relation in a certain limit and the formulation of the fermion action is quite similar to that of the Wilson fermions. It is therefore possible to apply identical numerical techniques to both, the domain-wall and Wilson fermion. A more detailed discussion of domain-wall fermions follows in Sec. 2.5

2.4 Computation of meson correlators

This section focuses on the discussion of the computation of meson correlators. For convenience sake in the later parts, we separate the path integral into a fermionic and a gluonic part, where the fermionic part is given by

$$\langle O\rangle_{_F} \equiv \frac{1}{Z_F}\int \mathcal{D}\bar{\psi}\mathcal{D}\psi e^{-S_F} O\,. \tag{2.28}$$

Here, the denominator Z_F is known as the *fermion determinant* given by

$$Z_F = \int \mathcal{D}\bar{\psi}\mathcal{D}\psi e^{-S_F} = \det D\,, \tag{2.29}$$

with D being the Dirac operator on the lattice. The path integral for the fermionic part can be performed by Wick contraction with a more detailed discussion following in Sec. 2.4.3. The full path integral, which can then be evaluated numerically, can be written as

$$\langle O\rangle \equiv \frac{1}{Z}\int \mathcal{D}U e^{-S_G} \det D \,\langle O\rangle_{_F}\,, \tag{2.30}$$

with the partition function

$$Z = \int \mathcal{D}U e^{-S_G} \det D \,. \tag{2.31}$$

The fermion determinant appearing in (2.30) is a consequence due to the effects of sea quarks, i.e. the creation and annihilation of quark-antiquark pairs in the vacuum. And including this determinant in lattice simulations is a challenge from a numerical point of view since the elements of the Dirac matrix D scale with $(12 \times \text{lattice size})^2$ where the expression in the brackets usually is of the order $\geq 10^6$. Due to limitations in computational power in the early days of lattice QCD, early studies employed the so-called quenched approximation, where dynamical sea quark loops are neglected, effectively replacing $\det D \to 1$. Nowadays, due to the development of massively parallel computers, accurate simulations including dynamical sea quarks employing various numerical techniques are possible.

One such approach is to consider the fermion determinant as a part of the Boltzman weight. By using

$$\log \det D = \operatorname{tr} \log D \,, \tag{2.32}$$

an effective action

$$S_{\text{Eff}} = S_G - \operatorname{tr} \log D \tag{2.33}$$

can be defined and the path integral can be rewritten as

$$\langle O \rangle = \frac{1}{Z} \int \mathcal{D}U e^{-S_{\text{Eff}}} \langle O \rangle_F \,. \tag{2.34}$$

In the case of Monte Carlo simulations, an approximation of the path integral is obtained by averaging the values on an ensemble of gauge configurations distributed with a probability $\approx \exp(-S_{\text{Eff}})$. Let $\langle O \rangle_F^{(i)}$ be the fermionic part of the path integral of the i-th gauge configuration. The total path integral is then reconstructed as follows

$$\langle O \rangle \simeq \frac{1}{N_{\text{Conf}}} \sum_i^{N_{\text{Conf}}} \langle O \rangle_F^{(i)} \,, \tag{2.35}$$

with N_{Conf} being the total number of configurations. This work employs gauge configurations obtained with $2+1$ flavors of dynamical quarks, generated with hybrid Monte Carlo algorithms [53].

2.4.1 Implementation of quark propagator

As mentioned previously, due to limitations in computational power as well as the accompanying numerical costs, it is quite challenging to completely solve the inverse of the Dirac operator for lattice fermions. To avoid the computation of the full inverse of the matrix D, we instead consider the propagator G and source S as vectors with a fixed source position $(t_0, \boldsymbol{x}_0, c_0, s_0)$, where c_0 and s_0 are the color index and Dirac index, respectively. By using a local source vector

$$S^{(\alpha_0,c_0)}(t,\boldsymbol{x})^{\alpha}_{c} = \delta_{t,t_0}\delta_{\boldsymbol{x},\boldsymbol{x}_0}\delta_{\alpha,\alpha_0}\delta_{c,c_0}\,, \tag{2.36}$$

the solution of the Dirac equation is written as

$$G^{\alpha_0,c_0}_{\text{local}}(t,\boldsymbol{x})^{\alpha}_{c} = \sum_{t',\boldsymbol{x}'}\sum_{\beta,d} D^{-1}(t,\boldsymbol{x}|t',\boldsymbol{x}')^{\alpha\beta}_{cd} S^{\alpha_0,c_0}(t',\boldsymbol{x}')^{\beta}_{d} = D^{-1}(t,\boldsymbol{x}|t_0,\boldsymbol{x}_0)^{\alpha\alpha_0}_{cc_0}\,. \tag{2.37}$$

This solution $G^{\alpha_0,c_0}_{\text{local}}(t,\boldsymbol{x})^{\alpha}_{c}$ represents a quark propagator from a fixed source point $(t_0, \boldsymbol{x}_0, c_0, s_0)$ to all sink points $(t, \boldsymbol{x}, c, s)$, i.e. a point-to-all propagator.

Going forward, we limit ourselves to the computation of connecting diagrams with degenerate quark masses. As will be shown later, in this case, we only require 12 solutions for all c_0 and s_0.

2.4.2 γ_5-hermiticity

One property that can be used to calculate meson correlators is that most of the fermions defined on the lattice are γ_5-hermitian, i.e. the Dirac operator, as well as its inverse, satisfy the relation

$$\gamma_5 D \gamma_5 = D^{\dagger}\,. \tag{2.38}$$

To show that γ_5-hermiticity is satisfied, let us consider the case of Wilson fermions. For this case, the Dirac operator with quark mass m is written as

$$\begin{aligned} D_W(x|y)_{\alpha\beta} =& (m+4)\mathbb{1}_{\alpha\beta}\delta_{x,y} \\ &- \frac{1}{2}\sum_{\mu=1}^{4}(\mathbb{1}-\gamma_\mu)_{\alpha\beta}U_\mu(x)\delta_{x+\hat{\mu},y} \\ &- \frac{1}{2}\sum_{\mu=1}^{4}(\mathbb{1}+\gamma_\mu)_{\alpha\beta}U^{\dagger}_\mu(x-\hat{\mu})\delta_{x-\hat{\mu},y}\,, \end{aligned} \tag{2.39}$$

where m is given in lattice units and $\hat{\mu}$ is a unit vector in the μ-direction. For simplicity we have

omitted the color indices. Since U_μ commutes with γ_5, we can then write

$$\begin{aligned}(\gamma_5 D_W \gamma_5)_{\alpha\beta} &= (m+4)\mathbb{1}_{\alpha\beta}\delta_{x,y} \\ &\quad - \frac{1}{2}\sum_{\mu=1}^{4}(\mathbb{1}+\gamma_\mu^\dagger)_{\alpha\beta}U_\mu(y-\hat{\mu})\delta_{x,y-\hat{\mu}} \\ &\quad - \frac{1}{2}\sum_{\mu=1}^{4}(\mathbb{1}-\gamma_\mu^\dagger)_{\alpha\beta}U_\mu^\dagger(y)\delta_{x,y+\hat{\mu}} \\ &= D_W^\dagger(x|y)_{\alpha\beta}\ ,,\end{aligned} \tag{2.40}$$

where we employed $\gamma_\mu = \gamma_\mu^\dagger$ and $\delta_{x\pm\hat{\mu},y} = \delta_{x,y\mp\hat{\mu}}$. With this we have verified relation (2.38). And since domain-wall fermions consist of Wilson fermions this property is inherited for them as well.

2.4.3 Coordinate space correlation functions

Correlation functions with the corresponding quantum numbers can be used to calculate the meson spectroscopy and amplitudes. Various quantities from correlation functions, such as time separated correlator $C(t)$, hadron vacuum polarization $\Pi(q^2)$ or temporal moment M_n, can be used to extract QCD and low-energy parameters. A clear physical interpretation can be achieved from two-point correlator functions in coordinate space.

While this section puts a special focus on the long distance behavior of correlators, the short-distance behavior also plays an important role for, e.g. renormalization [76] and the determination of the strong coupling constant α_s [77, 78]. We specifically return to the renormalization through the short distance behavior in Sec. 2.6.

Going forward, let us consider the operator corresponding to the π^-, i.e. $J_P = i\bar{u}\gamma_5 d$. The relation between the two-point function in coordinate space and the quark propagator is given by the Wick theorem

$$\begin{aligned}\langle 0|J_P(t,\boldsymbol{x})J_P^\dagger(0,\mathbf{0})|0\rangle &= \langle i\bar{u}\gamma_5 d(t,\boldsymbol{x})i\bar{d}\gamma_5 u(0,\mathbf{0})\rangle \\ &= \mathrm{tr}\left[\langle u(0,\mathbf{0})\bar{u}(t,\boldsymbol{x})\rangle_F\gamma_5\,\langle d(t,\boldsymbol{x})\bar{d}(0,\mathbf{0})\rangle_F\gamma_5\right] \\ &= \mathrm{tr}\left[D_u^{-1}(0,\mathbf{0}|t,\boldsymbol{x})\gamma_5 D_d^{-1}(t,\boldsymbol{x}|0,\mathbf{0})\gamma_5\right]\ ,\end{aligned} \tag{2.41}$$

where the trace denotes the trace over color and Dirac matrices. To continue, let us ignore isospin breaking, i.e. we put $m_u = m_d = m$ and $D_u^{-1}(0,\mathbf{0}|t,\boldsymbol{x}) = D_d^{-1}(0,\mathbf{0}|t,\boldsymbol{x}) = D^{-1}(0,\mathbf{0}|t,\boldsymbol{x})$. Then, using the γ_5-hermiticity (2.38), the two-point correlator can be written in terms of the quark propagator

with local sources (2.37)

$$\begin{aligned}\langle 0|J_P(t,\boldsymbol{x})J_P^\dagger(0,\mathbf{0})|0\rangle &= \mathrm{tr}\left[D^{-1,\dagger}(0,\mathbf{0}|t,\boldsymbol{x})D^{-1}(t,\boldsymbol{x}|0,\mathbf{0})\right] \\ &= \sum_{\alpha,\beta}\sum_{c,d}\left|D^{-1}(t,\boldsymbol{x}|0,\mathbf{0})_{\substack{\beta\alpha\\dc}}\right|^2 \\ &= \sum_{\alpha,\beta}\sum_{c,d}\left|F^{(\alpha,c)}_{\mathrm{local}}(t,\boldsymbol{x})_{\substack{\beta\\d}}\right|^2 .\end{aligned} \tag{2.42}$$

(2.42) contains the implication that a measurement of $\langle 0|J_P(t,\boldsymbol{x})J_P^\dagger(0,\mathbf{0})|0\rangle$ requires the propagator from $(0,\mathbf{0})$ to $(t,\boldsymbol{x})$ with 12 local sources.

Let us now consider the extension of (2.42) to other color singlet operators $J_\Gamma = \bar{u}\Gamma d$, with $\Gamma = \mathbb{1}, \gamma_5, \gamma_\mu, \gamma_\mu\gamma_5, \sigma_{\mu\nu}$. It is straightforward to check that the hermitian conjugate of these operators is given by simply swapping $u \leftrightarrow d$ with an additional sign, where the sign depends on the choice of Γ, i.e. $J_\Gamma^\dagger = d^\dagger\Gamma^\dagger\gamma_4 u = \pm\bar{d}\Gamma u$. Assuming $\bar{J}_\Gamma \equiv \bar{d}\Gamma u$, the two-point correlation function can be expressed as

$$\begin{aligned}\langle 0|J_\Gamma(t,\boldsymbol{x})\bar{J}(0,\mathbf{0})|0\rangle_F &= -\mathrm{tr}\left[D^{-1,\dagger}(0,\mathbf{0}|t,\boldsymbol{x})\gamma_5\Gamma D^{-1}(t,\boldsymbol{x},0,\mathbf{0})\Gamma\gamma_5\right] \\ &= -\sum_{\substack{\alpha,\beta\\\rho,\sigma}}\sum_{c,d} D^{-1}(t,\boldsymbol{x}|0,\mathbf{0})^*_{\substack{\rho\sigma\\dc}}(\gamma_5\Gamma)_{\rho\beta}D^{-1}(t,\boldsymbol{x}|0,\mathbf{0})_{\substack{\beta\alpha\\dc}}(\Gamma\gamma_5)_{\alpha\sigma} \\ &= -\sum_{\substack{\alpha,\beta\\\rho,\sigma}}\sum_{c,d} G^{(\sigma,c),*}_{\mathrm{local}}(t,\boldsymbol{x})_{\substack{\rho\\d}}(\gamma_5\Gamma)_{\rho\beta}G^{(\alpha,c)}_{\mathrm{local}}(t,\boldsymbol{x})_{\substack{\beta\\d}}(\Gamma\gamma_5)_{\alpha\sigma} .\end{aligned} \tag{2.43}$$

It is also possible to consider the case where the operators in the correlation function have different Γ's. Under the assumption of $J_{\Gamma_1} = \bar{u}\Gamma_1 d$ and $\bar{J}_{\Gamma_2} = \bar{d}\Gamma_2 u$, the correlation function is given by

$$\begin{aligned}\langle 0|J_{\Gamma_1}(t,\boldsymbol{x})\bar{J}_{\Gamma_2}(0,\mathbf{0})|0\rangle &= -\mathrm{tr}\left[D^{-1,\dagger}(0,\mathbf{0}|t,\boldsymbol{x})\gamma_5\Gamma_1 D^{-1}(t,\boldsymbol{x},0,\mathbf{0})\Gamma_2\gamma_5\right] \\ &= -\sum_{\substack{\alpha,\beta\\\rho,\sigma}}\sum_{c,d} G^{(\sigma,c),*}_{\mathrm{local}}(t,\boldsymbol{x})_{\substack{\rho\\d}}(\gamma_5\Gamma_1)_{\rho\beta}G^{(\alpha,c)}_{\mathrm{local}}(t,\boldsymbol{x})_{\substack{\beta\\d}}(\Gamma_2\gamma_5)_{\alpha\sigma} .\end{aligned} \tag{2.44}$$

But since the allowed intermediate states are controlled by the quantum numbers of the operators not all possible combinations of matrices Γ correspond to real physical measurements. One important and non-zero combination of operators is given by $J_{\Gamma_1} = \bar{u}\gamma_5 d$ and $J_{\Gamma_2} = \bar{d}\gamma_4\gamma_5 d$, which is important for the PCAC relation discussed in Sec. 2.7.

2.4.4 Zero momentum projection of correlation functions

This section focuses on the discussion of the zero momentum projection of the two-point correlator, i.e. the sum over all spatial points in the two-point correlation function. This allows for the measurement of the meson spectra in the rest frame of the sum. In the case of zero momentum, the correlation function for large time separations t is dominated by the lowest-lying energy state. This can be represented by expressing the correlation function as an exponential

$$\begin{aligned} C(t) &= \sum_{\boldsymbol{x}} \langle 0|J(t,\boldsymbol{x})J^{\dagger}(0,\mathbf{0})|0\rangle \\ &\simeq \frac{\langle 0|J|h\rangle\,|^2}{2m_h} e^{-m_h t}\,, \end{aligned} \tag{2.45}$$

where h is the ground-state hadron with corresponding mass m_h. The mass of the ground state can be estimated by considering the *effective mass*. Since the behavior of the correlator is controlled by an exponential, we can define

$$m_{\text{eff}} \equiv \log \frac{C(t)}{C(t+1)}\,. \tag{2.46}$$

This relation can be redefined to take into account periodic boundary conditions on the lattice. In this case, the correlator is given by

$$C(t) \simeq \frac{\langle 0|J|h\rangle\,|^2}{2m_h} \left(e^{-m_h t} + e^{-m_h (T-t)}\right)\,, \tag{2.47}$$

where T is the temporal extent of the lattice. The ratio of correlators can then be approximated by a cosh function

$$\frac{C(t+1)+C(t-1)}{C(t)} \simeq e^{-m_h} + e^{m_h}\,, \tag{2.48}$$

so that our redefined effective mass is given by

$$m_{\text{eff}} \equiv \cosh^{-1}\left(\frac{C(t+1)+C(t-1)}{2C(t)}\right)\,. \tag{2.49}$$

The practical use of the effective mass is found in the fixing of the fit range from fits to correlators, employing (2.45) or (2.47), to extract quantities, such as hadronic matrix elements or the mass from correlators. For this, the fit range is set to range where the effective mass shows a plateau, since the effective mass is a qualitative indicator on whether the correlator is sufficiently saturated by the ground state.

Although excited states are also of interest in lattice QCD studies, their measurement proves to

be more challenging than the ground state. Let there be a state with energy E, this state would then exponentially decay following $\exp(-(E_{m_h})t)$ and is hence only visible in the short-distance regime of the correlator, while it is buried in the ground state and only contributes as a kind of contamination for the long-distance regime.

2.4.5 Noise source

Following the discussion of the correlation function, this section focuses on the introduction of a noise source to estimate the sum over the spatial position of the source points $\boldsymbol{x}_0$. As previously mentioned in Sec. 2.4.1, the source position is fixed to a single point due to the local source. And since the number of available configurations is limited, a lot of information would be lost by only calculating the correlation function once for each configuration. At the same time, solving the Dirac equation with shifted source points would increase the amount of statistics, at the cost of higher computational time. By introducing the noise source, the higher computational cost can be avoided, while still allowing us to estimate the propagator from all spatial points $\boldsymbol{x}_0$.

To this end, let us discuss the correlation function $C(t)$ with noise source and the corresponding relations between local and noisy sources. We assume a noise vector η consisting of random numbers at each spatial point, which satisfy the condition

$$\left\langle\left\langle \eta(\boldsymbol{x})\eta^\dagger(\boldsymbol{y})\right\rangle\right\rangle = \delta_{\boldsymbol{x},\boldsymbol{y}}\,, \tag{2.50}$$

where $\langle\langle\cdot\rangle\rangle$ denotes an expectation value for the random numbers. This relation implies that the random numbers are independent. The actual type of random numbers is optional and up to preference. This work employs Z_2 random numbers, i.e. $\eta(\boldsymbol{x}) = \pm 1$, so that a Z_2 noise source at time slice t_0 is defined as

$$S_{Z_2}^{(\alpha_0,c_0)}(t,\boldsymbol{x})_{\;c}^{\alpha} = \delta_{t,t_0}\delta_{\alpha,\alpha_0}\delta_{c,c_0}\eta(\boldsymbol{x})\,. \tag{2.51}$$

In terms of this noise source, the Dirac equation is expressed through

$$G_{Z_2}^{(\alpha_0,c_0)}(t,\boldsymbol{x})_{\;c}^{\alpha} = \sum_{\boldsymbol{x}_0} D^{-1}(t,\boldsymbol{x}|t_0,\boldsymbol{x}_0)_{cc_0}^{\alpha\alpha_0}\eta(\boldsymbol{x}_0)\,. \tag{2.52}$$

We now replace $G_{\text{local}}^{(\alpha,c)}(t,\boldsymbol{x})$ in (2.43) with $G_{Z_2}^{(\alpha,c)}(t,\boldsymbol{x})$, so that our zero momentum projected

correlator $C(t)$ is given by

$$\begin{aligned}
&-\left\langle\left\langle \sum_{\substack{\alpha,\beta\\ \rho,\sigma}} \sum_{c,d} G^{(\sigma,c)}_{Z_2}(t,\boldsymbol{x})^*_{\substack{\rho\\ d}} G^{(\alpha,c)}_{Z_2}(t,\boldsymbol{x})_{\substack{\beta\\ d}} (\Gamma\gamma_5)_{\alpha\sigma} \right\rangle\right\rangle \\
&= -\sum_{\boldsymbol{x},x_0,y_0} \left\langle\left\langle \mathrm{tr}\left[\eta^\dagger(y_0) D^{-1,\dagger}(t_0,y_0|t,\boldsymbol{x})\gamma_5\Gamma D^{-1}(t,\boldsymbol{x}|t_0,x_0)\eta(x_0)\Gamma\gamma_5\right]\right\rangle\right\rangle \\
&\simeq -\sum_{\boldsymbol{x},x_0} \mathrm{tr}\left[D^{-1,\dagger}(t_0,x_0|t,\boldsymbol{x})\gamma_5\Gamma D^{-1}(t,\boldsymbol{x}|t_0,x_0)\Gamma\gamma_5\right] \\
&= \sum_{\boldsymbol{x},x_0} \langle 0|J_\Gamma(t,\boldsymbol{x})\bar{J}_\Gamma(t_0,x_0)|0\rangle_F \,.
\end{aligned} \tag{2.53}$$

Here, we have used (2.50) in the third step. (2.53) demonstrates that the sum of the local correlator over the source positions $\boldsymbol{x}_0$ can indeed be estimated by the noise source.

Interpreting the coordinates $\boldsymbol{x}$ and $\boldsymbol{x}_0$ as indices of the propagation matrix, the noise vector becomes a stochastic estimate of the trace. It is also possible to estimate the trace over color and spin by distributing the noise vector over the corresponding degrees of freedom. For the interested reader, [79, 80] consider the linked source distributed over the color space

$$S^{(\alpha_0)}_{\mathrm{linked}}(t,\boldsymbol{x})^{\alpha}_{c} = \delta_{t,t_0}\delta_{\alpha,\alpha_0}\eta(\boldsymbol{x})_c \,, \tag{2.54}$$

$$\langle\langle \eta(\boldsymbol{x})_c \eta^\dagger(\boldsymbol{y})_d \rangle\rangle = \delta_{\boldsymbol{x},\boldsymbol{y}}\delta_{c,d} \,, \tag{2.55}$$

while [81] the source distributed over the color and spinor space

$$\tilde{S}_{Z_2}(t,\boldsymbol{x})^{\alpha}_{c} = \delta_{t,t_0}\tilde{\eta}(\boldsymbol{x})^{\alpha}_{c} \,, \tag{2.56}$$

$$\left\langle\left\langle \tilde{\eta}(\boldsymbol{x})^{\alpha}_{c}\tilde{\eta}^\dagger(\boldsymbol{y})_{\substack{\beta\\ d}} \right\rangle\right\rangle = \delta_{\boldsymbol{x},\boldsymbol{y}}\delta_{c,d}\delta_{\alpha,\beta} \,, \tag{2.57}$$

is employed.

While these sources indeed save computational cost, the trade-off is that the corresponding results are more affected by stochastic noise. Additionally, in the cases where $\gamma_5\Gamma$ are not diagonal, the correlator cannot be simply measured by the source $\tilde{S}_{Z_2}$, but instead require a different solution vector for each Γ

$$\tilde{G}^{\Gamma}_{Z_2}(t,\boldsymbol{x}) = \sum_{x_0} D^{-1}(t,\boldsymbol{x}|t_0,x_0)(\Gamma\gamma_5)^\dagger\tilde{\eta}(x_0) \,, \tag{2.58}$$

in addition to the solution for the source $\tilde{S}_{Z_2}$

$$\tilde{G}_{Z_2}(t,\boldsymbol{x}) = \sum_{x_0} D^{-1}(t,\boldsymbol{x}|t_0,x_0)\tilde{\eta}(x_0) \,. \tag{2.59}$$

In the same way, it is not possible to simply measure the two point correlator of the color octets in case where the source is distributed over the color space. These measurements require an appropriate choice of the source for the correlator and a more detailed discussion on this topic can be found in [82].

2.5 Domain-wall fermion formulation

This section now focuses on a discussion of Möbius domain-wall (MDW) fermions, which is the formulation of fermions [83] employed in this work. This formulation of lattice fermions is defined on a 5D lattice, consisting of a 4D space-time and an additional dimension. The big advantage of this formulation is the good conservation of chiral symmetry. For MDW fermions, chiral symmetry is broken due to the finite extent of the additional dimension L_s, which is negligibly small in the ensembles employed in this work. This allows for some chiral relations to hold even at non-zero lattice spacing. One such example is given by the short-distance correlators for the vector and axial-vector cases, which are consistent up to finite mass and nonperturbative corrections. This provides us with a better method to compare lattice results with their corresponding counterparts in the continuum limit.

Let us start our discussion by defining the domain-wall fermion action for five dimensional fermion fields $\psi(x,s)$ as

$$S_{DW} = \sum_{x,y} \sum_{s,r=0}^{L_s-1} \bar{\psi}(x,s) D_{GDW}(x,s|,y,r) \psi(y,r)\,. \tag{2.60}$$

Here, x, y are coordinates in four dimensional space-time and s, r denote the indices of the additional fifth dimension. D_{GDW} is a generalized domain-wall Dirac operator, including the Shamir-type [84, 85] and Boriçi-type [86, 87], and, up to the mass term, can be written as a band matrix for s and r

$$D_{GDW} = \begin{pmatrix} \tilde{D} & -P_- & & & & mP_+ \\ -P_+ & \tilde{D} & -P_- & & & \\ & -P_+ & \tilde{D} & -P_- & & \\ & & \ddots & \ddots & \ddots & \\ & & & -P_+ & \tilde{D} & -P_- \\ mP_- & & & & -P_+ & \tilde{D} \end{pmatrix}. \tag{2.61}$$

In this definition, m is the bare mass of the fermions, $P_\pm = (1 \pm \gamma_5)/2$ are the chirality projection

operators and $\tilde{D}$ is defined through the 4D Wilson-Dirac operator $D(-M)$ with negative mass M

$$\tilde{D} = D_-^{-1} D_+ \tag{2.62}$$

$$D_- = 1 - cD_W(-M) \tag{2.63}$$

$$D_+ = 1 + bD_W(-M)\,. \tag{2.64}$$

The Möbius domain-wall fermions Dirac operator D_{MDW} is defined by setting $(b, c) = (3/2, 1/2)$. Through the definition (2.61), we are in a situation where we have to solve the inverse of D_- for all diagonal components. We hence redefine the operator by multiplying (2.61) with D_-

$$\begin{aligned}\hat{D}_{MDW} &\equiv D_- D_{MDW} \\ &= \begin{pmatrix} D_+ & -D_-P_- & & & & & mD_-P_+ \\ -D_-P_+ & D_+ & -D_-P_- & & & & \\ & -D_-P_+ & D_+ & -D_-P_- & & & \\ & & \ddots & \ddots & \ddots & & \\ & & & -D_-P_+ & D_+ & -D_-P_- & \\ mD_-P_- & & & & -D_-P_+ & D_+ & \end{pmatrix}.\end{aligned} \tag{2.65}$$

In a practical situation, to obtain the 4D quark propagator, we solve the equations for $\hat{D}_{MDW}$ instead of D_{MDW}. Going forward, let us consider S and G to be the source and propagator for the Dirac operator D_{MDW}, respectively. Their relation is then given by

$$\hat{D}_{MDW}(x, s|y, r)G(y, r|x_0, s_0) = S(x, s|x_0, s_0) \tag{2.66}$$

with x, y, x_0 being the coordinates in 4D space-time and s, r, s_0 being the indices in the extra dimension. We have omitted the color and spinor indices here. Following the Wick contraction discussed in Sec. 2.4, the hadron correlator can then be extracted from the solution

$$G(x, s|x_0, s_0) = \hat{D}^{-1}_{MDW}(x, s|y, r)S(y, r|x_0, s_0)\,. \tag{2.67}$$

To obtain proper physical quantities composed of 4D quarks, a projection of the 5D fermion fields $\psi(x, s)$ onto 4D space-time is required. To this end, we construct the 4D quark fields following

$$q(x) = P_-\psi(x, 0) + P_+\psi(x, L_s - 1)\,, \tag{2.68}$$

$$\bar{q}(x) = \bar{\psi}(x, 0)P_+ + \bar{\psi}(x, L_s - 1)P_-\,, \tag{2.69}$$

employing the fact that the left-handed and right-handed modes live near $s = 0$ and $s = L_s - 1$, respectively. Employing this definition, the relation between the 4D quark propagator D^{-1}_{4D} and

$\hat{D}^{-1}_{MDW}$ can be given through

$$\begin{aligned} D^{-1}_{4D} \equiv & \langle q(x)\bar{q}(y)\rangle_F \\ =& P_- D^{-1}_{MDW}(x,0;y,0)P_+ + P_- D^{-1}_{MDW}(x,0;y,L_s-1)P_- \\ & + P_+ D^{-1}_{MDW}(x,L_s-1;y,0)P_+ + P_+ D^{-1}_{MDW}(x,L_s-1;y,L_s-1)P_- \\ =& (\delta_{s,0}P_- + \delta_{s,L_s-1}P_+) D^{-1}_{MDW}(x,s|y,s)(\delta_{r,0}P_+ + \delta_{r,L_s-1}P_-) \\ =& (\delta_{s,0}P_- + \delta_{s,L_s-1}P_+) \hat{D}^{-1}_{MDW}(x,s;y,s) D^{-1} (\delta_{r,0}P_+ + \delta_{r,L_s-1}P_-)\,. \end{aligned} \tag{2.70}$$

Through comparison of (2.67) with (2.70), the 4D quark propagator can be extracted by multiplying the source and solution $G(x,s|x_0,s_0)$ with $D^{-1}(\delta_{r,0}P_+ + \delta_{r,L_s-1}P_-)$ and $(\delta_{s,0}P_- + \delta_{s,L_s-1}P_+)$, respectively. Furthermore, by combining these two relations it is possible to measure hadron correlation functions following the discussions of the previous sections.

2.6 Renormalization of operators on the lattice

In the previous sections we have established Lattice QCD as a tool that allows for the nonperturbative study of hadronic decays and transition processes. Important input parameters in the phenomenological studies of the Standard Model, such as decay constants and form factors from hadronic matrix elements, can be extracted from two- and three-point correlation functions.

To study hadronic matrix elements from lattice QCD calculations we require renormalization, since they do not correspond to the values in the renormalization scheme of the continuum theory, e.g. the $\overline{\text{MS}}$-scheme. This is necessary even though the operators involved in the determination of these matrix elements, such as locally constructed vector currents $\bar{q}\gamma_\mu q$, have no anomalous dimensions, since they do not conserve due to the existence of lattice artifacts. After renormalization though, physical quantities determined on the lattice can be compared to the continuum theory counterpart.

One possible way to perform renormalization is through *matching*. The basic idea is to measure some physical quantity in lattice QCD containing the operator to be renormalized and calculate the same quantity perturbatively in the $\overline{\text{MS}}$-scheme. We then determine the renormalization constant by imposing the condition that both determinations should be equal. While it is possible to perform matching through an intermediate scheme such as the RI/MOM scheme [88], we, however, focus on the direct renormalization here. The quantity employed to perform the matching should satisfy the following conditions to obtain good control over the systematic error in the renormalization constant. First, the discretization error on the lattice should be under good control. Secondly, the energy scale should be large enough so that perturbative expansion and operator product expansion (OPE) can be applied.

Going forward, we are now going to discuss one way to extract the renormalization constant

known as the X-space method [76]. This method employs a correlation function with finite separation $|x|$

$$\Pi^{\text{lat}}(x^2, a^2) = \langle 0|J_\Gamma(x)\bar{J}_\Gamma(0)|0\rangle \ , \tag{2.71}$$

which can be directly measured following our discussion from Sec. 2.4.3. Introducing the renormalization constant $Z_\Gamma^{\overline{\text{MS}}/\text{lat}}$ for J_Γ the relation between the perturbative series $\Pi^{\overline{\text{MS}}}$, obtained in the $\overline{\text{MS}}$-scheme, and Π^{lat}, up to nonperturbative and discretization effects, can be written as

$$\Pi^{\overline{\text{MS}}}(\mu^2; x^2) = \left(Z_\Gamma^{\overline{\text{MS}}/\text{lat}}(\mu^2, a^2)\right)^2 \Pi^{\text{lat}}(x^2, a^2)\,, \tag{2.72}$$

Treating this equation as the renormalization condition, we can solve it for $Z_\Gamma^{\overline{\text{MS}}/\text{lat}}$ and express the solution as

$$\begin{aligned}\tilde{Z}_\Gamma^{\overline{\text{MS}}/\text{lat}}(\mu^2, a^2; x) &\equiv \sqrt{\frac{\Pi^{\overline{\text{MS}}}(\mu^2; x^2)}{\Pi^{\text{lat}}(x^2, a^2)}} \\ &= Z_\Gamma^{\overline{\text{MS}}/\text{lat}}(\mu^2, a^2) + C_{-2}(a/x)^2 + C_4 x^4 + C_6 x^6\,.\end{aligned} \tag{2.73}$$

In this formulation, the discretization error is controlled through the coefficient C_{-2}, while C_4 and C_6 control the nonperturbative corrections from mass-dimension four and six operators, respectively. Based on (2.73) it is hence possible to extract the renormalization constant $Z_\Gamma^{\overline{\text{MS}}/\text{lat}}(\mu^2, a^2)$ from a fit to $\tilde{Z}_\Gamma^{\overline{\text{MS}}/\text{lat}}(\mu^2, a^2; x)$.

In the case of MDW fermions the renormalization constants retain chiral symmetry, i.e. the renormalization constants for the vector current $\bar{q}\gamma_\mu q$ and axial current $\bar{q}\gamma_\mu\gamma_5 q$ are equivalent

$$Z_V^{\overline{\text{MS}}/\text{lat}}(a^2) = Z_A^{\overline{\text{MS}}/\text{lat}}(a^2)\,. \tag{2.74}$$

In this definition we have omitted the scale μ dependence since vector (axial) current has no anomalous dimension. A similar relation can be obtained relating the (pseudo-) scalar density

$$Z_S^{\overline{\text{MS}}/\text{lat}}(\mu^2, a^2) = Z_P^{\overline{\text{MS}}/\text{lat}}(\mu^2, a^2)\,. \tag{2.75}$$

By taking advantage of these chiral properties, the authors of [76] have determined the renormalization constant by combining $\tilde{Z}_\Gamma^{\overline{\text{MS}}/\text{lat}}(\mu^2, a^2; x)$ in order to cancel out some of the nonperturbative effects contributing to the fit. This not only makes a determination of the renormalization constant easier, it also helps in the determination of Z_Γ.

2.7 The PCAC Relation on the lattice

This section focuses on a discussion of the partially conserved axial vector current relation, commonly referred to as the PCAC relation, associated with chiral symmetry. We focus our discussion on how the relation holds on the lattice and what effects it has on the correlation function. For a more detailed discussion we refer to [65, 89].

To start off our discussion, let us first review the PCAC relation in the continuum theory. To this end, we define isovector axial currents, as well as pseudoscalar density operators

$$A_\mu^a \equiv \frac{1}{2}\bar{\psi}\gamma_\mu\gamma_5\tau^a\psi\,, \tag{2.76}$$

$$P^a \equiv \frac{1}{2}\bar{\psi}\gamma_5\tau^a\psi\,, \tag{2.77}$$

where $\psi = (u, d)^T$ and τ^a are the Pauli matrices. We then consider an infinitesimal chiral rotation

$$\delta\psi(x) = \frac{1}{2}\omega^a(x)\gamma_5\tau^a\psi(x)\,, \tag{2.78}$$

$$\delta\bar{\psi}(x) = \frac{1}{2}\omega^a(x)\psi(x)\gamma_5\tau^a\,. \tag{2.79}$$

The change of the action S and an operator $\mathcal{O}$ under the aforementioned transformation are then related through the Ward-Takahashi identity by

$$\langle 0|\delta S\mathcal{O}|0\rangle = \langle 0|\delta\mathcal{O}|0\rangle\ . \tag{2.80}$$

The explicit expression for the change of the action is given by

$$\delta S = \int d^4x\omega^a\left(-\partial_\mu A_\mu^a + 2mP^a\right)\,, \tag{2.81}$$

where we ignore isospin breaking, i.e. we set $m = m_u = m_d$. The expression for the change of the operator $\mathcal{O}$ can be obtained by setting $\mathcal{O} = P^a(y)$ and $\omega^b(x) = \omega\delta_{ab}\delta(x-y)$

$$\delta\mathcal{O} = 2\omega\delta(x-y)\bar{\psi}\psi(y)\,. \tag{2.82}$$

Combining (2.81), (2.82) with (2.80), the identity can be written as

$$\langle 0|\partial_\mu A_\mu^a(x)P^a(y)|0\rangle - 2m\,\langle 0|P^a(x)P^a(y)|0\rangle = 2\delta(x-y)\,\langle 0|\bar{\psi}\psi(y)|0\rangle\ . \tag{2.83}$$

From (2.83) we can derive the PCAC relation for the low energy regime. For this, we consider correlators with time separation t summed over the spatial coordinate $\boldsymbol{x}$. For the sake of simplicity,

we assume $y = (0, \mathbf{0})$. Since the operator $\partial_\mu A^a_\mu(x)$ is projected to zero momentum, the only visible contribution to the l.h.s. of (2.83) comes from $\mu = 4$. For long time separations t, the contribution of the ground state π mesons is dominant.

Employing this knowledge, and the fact that through the definition of the pion decay constant, the matrix element of the axial current can be written as

$$\partial_t \langle 0|A^a_4(t, \boldsymbol{x})|\pi^a(t, \boldsymbol{p} = \mathbf{0})\rangle = m_\pi^2 f_\pi e^{-m_\pi t}\,, \tag{2.84}$$

it is possible to express the asymptotic form factor of the correlator as

$$\begin{aligned} &\sum_{\boldsymbol{x}} \langle 0|\partial_t A^a_4(t, \boldsymbol{x}) P^a(0, \mathbf{0})|0\rangle \\ &\simeq \frac{m_\pi f_\pi}{2} e^{-m_\pi t} \langle \pi^a(\mathbf{0})|P^a|0\rangle\ . \end{aligned} \tag{2.85}$$

On the other hand, we can write the correlator of the pseudoscalar correlator as

$$\begin{aligned} &\sum_{\boldsymbol{x}} \langle 0|P^a(t, \boldsymbol{x}) P^a(0, \mathbf{0})|0\rangle \\ &\simeq \frac{1}{2m_\pi} e^{-m_\pi t} \langle 0|P^a|\pi^a(\mathbf{0})\rangle \langle \pi^a(\mathbf{0})|P^a|0\rangle\ . \end{aligned} \tag{2.86}$$

Going back to (2.83), in the limit of $t \gg 0$ the r.h.s. can be ignored, and combining this with (2.85) and (2.86) we arrive at the compact

$$m_\pi^2 f_\pi = 2m \langle 0|P^a|\pi^a(\mathbf{0})\rangle\ . \tag{2.87}$$

This equation gives a relation between the pion mass and the quark mass, which explicitly breaks chiral symmetry. It furthermore contains the implication that in the chiral limit $m \to 0$ the axial current is a conserved quantity, hence why (2.87) is known as the PCAC relation.

Turning our attention towards the lattice, it seems reasonable to assume a similar relation to (2.87), albeit some modifications are expected. As previously shown in Sec. 2.6, renormalization is required for the local current $A^a_\mu(x)$. In addition to that, due to lattice regularization, it is also necessary to incorporate the corrections for the chiral symmetry. In the case of MDW fermions, the chiral symmetry is slightly broken due to the finite L_s on which they are defined. This results in a modification of the quark mass away from their bare mass m_{bare}

$$m = m_{\text{bare}} + m_{\text{res}}\,, \tag{2.88}$$

where the residual quark mass m_{res} parametrizes the symmetry breaking. With this setup, the

PCAC relation is expressed as

$$m_\pi^2 f_\pi = Z_A \langle 0|\partial_\mu A_\mu^a|\pi^a(\mathbf{0})\rangle = 2(m_{\rm bare} + m_{\rm res}) \langle 0|P^a|\pi^a(\mathbf{0})\rangle \ . \tag{2.89}$$

This work employs the JLQCD ensembles with MDW fermions where the residual mass is $\lesssim 1\,\mathrm{MeV}$ [90, 91]. The residual mass can be estimated by the breaking of the Ginsparg-Wilson relation and gives an indication of the good chiral properties of the lattice used in this work. As mentioned previously in 2.6, the renormalization constant relations $Z_V = Z_A$ and $Z_S = Z_P$ hold from chiral symmetry up to $\mathcal{O}(m_{\rm res}^2)$ [92].

Chapter 3

Inclusive Decays on the Lattice

Following the previous chapter, we will now focus on the extension of lattice QCD techniques towards the description of inclusive decays. As mentioned at the end of ch. 1, the discrepancy in the determination of the CKM parameters in the bottom sector remain an unresolved question, as of yet. Hence why this newly developed application of lattice QCD provides an interesting prospect, since lattice techniques have not been applied on inclusive decays before and, if applicable, will provide a new and independent outlook on the discrepancy.

Obviously, the lattice comes with its own sets of challenges. One major problem in the application of lattice techniques towards the inclusive sector is the sheer amount of potential states, possibly containing multi hadron states, contributing in these types of decays. It is easy to imagine that singling out the amplitudes for each of these contributions and summing them up over the whole phase space seems like a daunting task. Combining this with the fact that the extraction of spectral densities from hadron correlators remains an intractable task, it becomes clear that a treatment on the lattice seems impractical, if not possible at all.

Recently, the authors of [29] have proposed a method through which the analysis of inclusive decays is enabled through the computation of smeared spectral densities of hadron correlators. For the inclusive semileptonic decays the role of the smearing is defined through the energy integral over the allowed phase-space. This smearing then allows an approximation of the energy integral appearing in the total decay rate by employing four-point correlation function computed on the lattice. Although it would be desirable to immediately apply this new method towards a determination of the CKM matrix elements V_{ub} and V_{cb}, the bottom sector has its own sets of problems when treated on the lattice. Namely, we expect large discretization errors for m_b, while at the same time it is also challenging to simulate the physical bottom mass in lattice simulations. These reasons lead us to first apply this method on the inclusive decays of charmed mesons, since for the charm sector the aforementioned systematic effects are under better control, allowing us to verify the new method.

Furthermore, a good understanding of the systematic errors is required, such as the error due to the approximation introduced in this new method, as well as finite volume corrections, which pose a general challenge in lattice simulations. This work will present new ideas and their application, on how these systematic errors can be estimated and on what their corresponding effects on our final result are.

The rest of this chapter will introduce all tools and notation necessary to analyze inclusive decays through the use of hadron correlators obtained on the lattice and is structured as follows. In 3.1, we will present a formulation of the inclusive decay rate in the continuum limit. This will be followed by an introduction on how an estimate for the energy integral over the hadronic final states can be constructed using hadron correlators in 3.2

3.1 The inclusive decay rate

First of all, we focus on the theoretical framework for the calculation of the decay rate of inclusive semileptonic processes in the continuum theory. In contrast to [29, 93], where the focus was on the $B_s \to X_c \ell \nu_\ell$ channel, in this work we focus on the decay $D_s \to X_s \ell \nu_\ell$ as depicted in Figure 3.1, where X_s represents all possible final state mesons containing an s-quark. The formalism for both cases is essentially the same, so an application towards the bottom sector is straightforward.

For the vector channel the ground-state contribution to X_s is given by the $\eta^{(\prime)}$. We differentiate between the η and η' meson. While the main quantum numbers are the same for both and they possess the same quark contents, they possess a different superposition of those

$$\eta = \frac{1}{\sqrt{6}} \left(u\bar{u} + d\bar{d} - 2s\bar{s} \right) , \quad \eta' = \frac{1}{\sqrt{3}} \left(u\bar{u} + d\bar{d} + s\bar{s} \right) ,$$

where the η is part of a flavor $SU(3)$ octet while the η' is a singlet. The η', when compared to the η, possesses a higher mass, longer lifetime and different decays. More details on the difference can

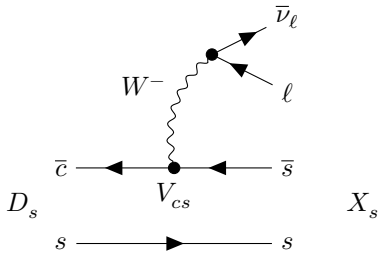

Figure 3.1: Feynman digram for the decay $D_s \to X_s \ell \nu_\ell$.

be found in [94–97]. For the $\bar{c} \to \bar{s}$ process, the weak Hamiltonian is given by

$$H_W = \frac{4G_F}{\sqrt{2}} V_{cs} [\bar{c}_L \gamma^\mu s_L][\bar{\nu}_{\ell L} \gamma_\mu \ell_L] \,,$$

where G_F is the Fermi constant and V_{cs} is the CKM matrix element governing the charged-current flavor-changing quark transition. For this process, the electroweak quark-current is then given by $J_\mu = \bar{c}_L \gamma^\mu s_L = 1/2 \bar{c} \gamma_\mu (1 - \gamma_5) s$, which can also be written in the form $J_\mu = V_\mu - A_\mu$ where V_μ and A_μ are given by $\bar{c} \gamma_\mu s$ and $\bar{c} \gamma_\mu \gamma_5 s$, respectively.

Going forward we consider the decay rate of inclusive processes, which, compared to its exclusive counterpart, has one more kinematical variable due to the freedom in the mass of the outgoing hadrons, totaling at three. The differential decay rate for the inclusive process can be written as

$$\frac{d\Gamma}{dq^2 dq_0 dE_\ell} = \frac{G_F^2 |V_{cs}|^2}{8\pi^3} L_{\mu\nu} W^{\mu\nu} \,, \tag{3.1}$$

where we neglect QED corrections. Here, $L_{\mu\nu}$ is the leptonic tensor

$$L_{\mu\nu} = p_\ell^\mu p_{\nu_\ell}^\nu + p_\ell^\nu p_{\nu_\ell}^\mu - g^{\mu\nu} p_\ell p_{\nu_\ell} - i\epsilon^{\mu\alpha\nu\beta} p_{\ell,\alpha} p_{\nu_\ell,\beta} \,, \tag{3.2}$$

where p_ℓ and p_{ν_ℓ} denote the four-momenta of the lepton and neutrino, respectively, hence allowing to write the momentum transfer between initial and final meson as $q = p_\ell + p_{\nu_\ell}$. Furthermore, the hadronic tensor $W^{\mu\nu}$ is given by

$$\begin{aligned} W^{\mu\nu}(p_{D_s}, q) =& \frac{1}{2\pi} \frac{1}{2E_{D_s}} \int d^4x e^{iqx} \langle D_S(\boldsymbol{p}_{D_s}) | J^{\mu\dagger}(x) J^\nu(0) | D_S(\boldsymbol{p}_{D_s}) \rangle \\ =& \frac{1}{2E_{D_s}} \sum_{X_s} (2\pi)^3 \delta^{(4)}(p_{D_s} - q - p_{X_s}) \\ & \times \langle D_S(\boldsymbol{p}_{D_s}) | J^{\mu\dagger}(x) | X_s(\boldsymbol{p}_{X_s}) \rangle \langle X_s(\boldsymbol{p}_{X_s}) | J^\nu(0) | D_S(\boldsymbol{p}_{D_s}) \rangle \,, \end{aligned} \tag{3.3}$$

where we inserted a complete set of states $\mathbb{1} = \sum_{X_s} |X_s(\boldsymbol{q}_{X_s})\rangle \langle X_s(\boldsymbol{q}_{X_s})|$ in the second line. It implicitly includes an integration over all possible momenta $\boldsymbol{p}_{X_s}$ under a Lorentz invariant phase-space integral, where $q = p_{D_s} - p_{X_s}$ is the momentum transfer between the initial and final hadronic states. One point of notice to that this work focuses solely on the case of a D_s meson at rest, i.e. $\boldsymbol{p}_{D_s} = (0,0,0)$. Furthermore, the hadronic tensor can be decomposed as a sum of five scalar structure functions $W_i \equiv W_i(q^2, v \cdot q)$ given by

$$W^{\mu\nu} = g^{\mu\nu} W_1 + v^\mu v^\nu W_2 - i\epsilon^{\mu\nu\alpha\beta} v_\alpha q_\beta W_3 + q^\mu q^\nu W_4 + (v^\mu q^\nu + v^\nu q^\mu) W_5 \,, \tag{3.4}$$

where $v = p_{D_s}/M_{D_s} = (1,0,0,0)$ is the four-velocity of the initial D_s meson at rest and $q = (q_0, \boldsymbol{q}) =$

$(M_{D_s} - \omega, -\boldsymbol{p}_{X_s})$. Going forward, ω will denote the energy of the final state hadron, i.e. $\omega = E_{X_s}$. In anticipation of the following calculations it is convenient to introduce the relations

$$W^{00} = -W_1 + W_2 + q_0^2 W_4 + 2q_0 W_5 \tag{3.5}$$

$$W^{ij} = \delta_{ij} W_1 + q_i q_j W_4 - i\epsilon_{ij0k} q^k W_3 \tag{3.6}$$

$$W^{0i} = q_i (q_0 W_4 + W_5)\,, \tag{3.7}$$

where we denote the spatial indices by i, j, k. These relations will prove useful in the following calculations. By contracting the spatial indices with the three-momentum components q_i it is possible to invert these relations and hence obtain expressions for the structure functions W_i in terms of the hadronic tensor and $\boldsymbol{q}$. For this, let us first write down more general expressions by multiplying the spatial indices of the hadronic tensor with q_i and/or q_j, respectively and summing over the indices

$$\sum_i W_{ii} = 3W_1 + \boldsymbol{q}^2 W_4 \tag{3.8}$$

$$\sum_{i,j} q_i W_{ij} q_j = \boldsymbol{q}^2 W_1 + (\boldsymbol{q}^2)^2 W_4 \tag{3.9}$$

$$\sum_i q_i (W_{0i} + W_{i0}) = 2\boldsymbol{q}^2 (q_0 W_4 + W_5) \tag{3.10}$$

$$\sum_{i,j,k} W_{ij} \epsilon^{ijk} q_k = -i\boldsymbol{q}^2 W_3\,. \tag{3.11}$$

These relations hold for any $\boldsymbol{q}$. The relation (3.11) for the structure function W_3 will not contribute in the rest of this work, since it only appears in the case where massive leptons $m_\ell \neq 0$ appear. Since this work considers only the case of massless or negligible leptons, the relation for W_3 is mentioned only for the sake of completeness.

We now consider the inversion of these relations. For $\boldsymbol{q} = 0$ it follows that the only contribution is from

$$W_1 = \frac{1}{2} \sum_i W_{ii}\,. \tag{3.12}$$

For all $\boldsymbol{q} \neq 0$ we can solve the system created by (3.8) and (3.9) and obtain

$$\left\{ \begin{array}{ll} \boldsymbol{q}^2 W_4 & = \frac{1}{\boldsymbol{q}^2} \sum_{i,j} q_i W_{ij} q_j - W_1 \\ W_1 & = \frac{1}{3} \left(\sum_i W_{ii} - \boldsymbol{q}^2 W_4 \right) \end{array} \right. \rightarrow \left\{ \begin{array}{ll} \boldsymbol{q}^2 W_4 & = \frac{3}{2} \frac{1}{\boldsymbol{q}^2} \sum_{i,j} q_i W_{ij} q_j - \frac{1}{2} \sum_i W_{ii} \\ W_1 & = \frac{1}{2} \sum_i W_{ii} - \frac{1}{2} \frac{1}{\boldsymbol{q}^2} \sum_{i,j} q_i W_{ij} q_j \end{array} \right. . \tag{3.13}$$

By combining these two, we obtain a relation for W_5 using (3.10)

$$W_5 = \frac{1}{2}\frac{1}{\boldsymbol{q}^2}\sum_i q_i(W_{i0}+W_{0i}) - \frac{q_0^2}{\boldsymbol{q}^2}\left[\frac{3}{2}\frac{1}{\boldsymbol{q}^2}\sum_{i,j} q_i W_{ij} q_j - \frac{1}{2}\sum_i W_{ii}\right], \tag{3.14}$$

as well as W_2 from (3.5)

$$W_2 = W_{00} - \frac{q_0}{\boldsymbol{q}^2}\sum_i q_i(W_{i0}+W_{0i}) + W_1 - q_0^2 W_4\,, \tag{3.15}$$

where we further replace W_1 and W_4 with their corresponding expression from (3.13) to obtain a full expression in term of the hadronic tensor $W_{\mu\nu}$. In summary, here we list all relations between the structure functions and the hadronic tensor

$$W_1 = \frac{1}{2}\sum_{i,j}\left[\delta_{ij} - \frac{q_i q_j}{\boldsymbol{q}^2}\right] W_{ij}\,, \tag{3.16}$$

$$\begin{aligned} W_2 = {} & W_{00} - \frac{q_0}{\boldsymbol{q}^2}\sum_i q_i(W_{i0}+W_{0i}) + \frac{q_0^2}{(\boldsymbol{q}^2)^2}\sum_{i,j} q_i W_{ij} q_j \\ & + \frac{1}{2}\left(1 - \frac{q_0^2}{\boldsymbol{q}^2}\right)\sum_{i,j}\left[\delta_{ij} - \frac{q_i q_j}{\boldsymbol{q}^2}\right] W_{ij} \end{aligned}\,, \tag{3.17}$$

$$W_4 = \frac{1}{(\boldsymbol{q}^2)^2}\sum_{i,j} q_i W_{ij} q_j - \frac{1}{2}\frac{1}{(\boldsymbol{q}^2)^2}\sum_{i,j}\left[\delta_{ij} - \frac{q_i q_j}{\boldsymbol{q}^2}\right] W_{ij}\,, \tag{3.18}$$

$$W_5 = \frac{1}{2}\frac{1}{\boldsymbol{q}^2}\sum_i q_i(W_{i0}+W_{0i}) - \frac{q_0}{(\boldsymbol{q}^2)^2}\sum_{i,j} q_i W_{ij} q_j + \frac{1}{2}\frac{q_0}{(\boldsymbol{q}^2)^2}\sum_{i,j}\left[\delta_{ij} - \frac{q_i q_j}{\boldsymbol{q}^2}\right] W_{ij}\,. \tag{3.19}$$

Going back to the differential decay rate, (3.1), we perform the integration over the lepton energy $E_{l,0} = p_{l,0}$ in the massless lepton limit, i.e. $m_l \simeq 0$. Additionally, we can also rewrite the integrals over q^2 and q_0 in terms of $\boldsymbol{q}^2 = q_0^2 - q^2$ and $\omega = M_{D_s} - q_0$, i.e. the three-momentum and energy of the final hadronic state X_c, where the Jacobian of this transformation is 1, to obtain an expression for the decay rate

$$\frac{\Gamma}{d\boldsymbol{q}^2 d\omega} = \frac{G_F^2 |V_{cs}|^2}{24\pi^3}\sqrt{\boldsymbol{q}^2}\left[(q_0^2 - \boldsymbol{q}^2)W_1 + \frac{1}{3}\boldsymbol{q}^2 W_2\right]. \tag{3.20}$$

By inserting (3.16) and (3.17) we arrive at

$$\begin{aligned}\frac{\Gamma}{d\boldsymbol{q}^2 d\omega} = \frac{G_F^2|V_{cs}|^2}{24\pi^3}\sqrt{\boldsymbol{q}^2}\Bigg[\boldsymbol{q}^2\left\{W_{00} - \sum_i W_{ii}\right\} + \sum_{i,j} q_i W_{ij} q_j \\ - q_0 \sum_i q_i (W_{i0} + W_{0i}) \\ + q_0^2 \sum_i W_{ii}\Bigg] \,.\end{aligned} \tag{3.21}$$

In the following steps, we now define the key quantities used in this work. First, let us introduce a convenient notation for the differential decay rate

$$\frac{\Gamma}{d\boldsymbol{q}^2 d\omega} = \frac{G_F^2|V_{cs}|^2}{24\pi^3}\sqrt{\boldsymbol{q}^2} X(\boldsymbol{q}^2,\omega)\,, \tag{3.22}$$

where the definition of $X(\boldsymbol{q}^2,\omega)$ is given by comparison with (3.1)

$$X(\boldsymbol{q}^2,\omega) = \frac{3}{\sqrt{\boldsymbol{q}^2}}\int_{E_\ell^{\min}}^{E_\ell^{\max}} dE_\ell L_{\mu\nu} W^{\mu\nu}\,. \tag{3.23}$$

In the scope of this work we integrate over the whole energy region of the lepton energy allowed by the kinematics, i.e. we integrate from $E_\ell^{\min}$ to $E_\ell^{\max}$. A change to the limits of integrations, e.g. for the purpose of obtaining a better comparison with experimental results, can be implemented trivially and does not change the analysis strategy discussed going forward. We can also obtain a different representation for $X(\boldsymbol{q}^2,\omega)$ by subdividing it the following way

$$X(\boldsymbol{q}^2,\omega) = X^{(0)}(\boldsymbol{q}^2,\omega) + X^{(1)}(\boldsymbol{q}^2,\omega) + X^{(2)}(\boldsymbol{q}^2,\omega)\,, \tag{3.24}$$

where the superscript controls the power contribution in $q_0 = M_{D_s} - \omega$, i.e.

$$X^{(0)}(\boldsymbol{q}^2,\omega) = \boldsymbol{q}^2\left(W_{00} - \sum_i W_{ii}\right) + \sum_{i,j} q_i W_{ij} q_j\,, \tag{3.25}$$

$$X^{(1)}(\boldsymbol{q}^2,\omega) = -q_0 \sum_i q_i (W_{i0} + W_{0i})\,, \tag{3.26}$$

$$X^{(2)}(\boldsymbol{q}^2,\omega) = q_0^2 \sum_i W_{ii}\,. \tag{3.27}$$

We finally obtain the total decay rate by integrating over ω and $\boldsymbol{q}^2$

$$\Gamma = \frac{G_F^2|V_{cs}|^2}{24\pi^3}\int_0^{\boldsymbol{q}^2_{\max}} d\boldsymbol{q}^2 \sqrt{\boldsymbol{q}^2}\bar{X}(\boldsymbol{q}^2)\,. \tag{3.28}$$

Here, the enclosed expression for the energy integral ω is given by

$$\bar{X}(\boldsymbol{q}^2) = \sum_{l=0}^{2} \bar{X}^{(l)}(\boldsymbol{q}^2)\,, \quad \bar{X}^{(l)}(\boldsymbol{q}^2) \equiv \int_{\omega_{\min}}^{\omega_{\max}} d\omega X^{(l)}(\boldsymbol{q}^2, \omega)\,, \tag{3.29}$$

where we use the definitions

$$\begin{aligned} X^{(0)}(\boldsymbol{q}^2,\omega) &= \boldsymbol{q}^2 W_{00} + \sum_i (q_i^2 - \boldsymbol{q}^2) W_{ii} + \sum_{i\neq j} q^i W_{ij} q^j\,, \\ X^{(1)}(\boldsymbol{q}^2,\omega) &= -q_0 \sum_i q^i \left(W_{0i} + W_{i0}\right)\,, \\ X^{(2)}(\boldsymbol{q}^2,\omega) &= q_0^2 \sum_i W_{ii}\,. \end{aligned} \tag{3.30}$$

The integral limits are $\boldsymbol{q}^2_{\max} = (M_{D_s}^2 - M_\eta^2)^2/(4M_{D_S}^2)$, $\omega_{\min} = \sqrt{M_\eta^2 + \boldsymbol{q}^2}$ and $\omega_{\max} = M_{D_s} - \sqrt{\boldsymbol{q}^2}$, by imposing four-momentum conservation as well as fixing the lightest final state of this inclusive decay to the η-meson.

These equations present the central focus of this work, since they allow us to express the total decay rate through an integral over the energy ω of the hadronic final state, as well as the corresponding three-momentum $\boldsymbol{q}^2$, where all information is collected in the functions $X^{(l)}$. These functions themselves can be expressed through a linear combination of components of the hadronic tensor and some kinematical factors. This representation will prove useful in Ch. 4, when we address the lattice calculations of these quantities. Finally, let us address a way to expose the $V-A$ nature of the charged current in $X^{(l)}$. We start from the decomposition of the hadronic tensor $W^{\mu\nu} = W^{\mu\nu}_{VV} + W^{\mu\nu}_{AA} + W^{\mu\nu}_{VA} + W^{\mu\nu}_{AV}$. This allows us to rewrite $X^{(l)}$ in a similar fashion

$$X^{(l)} = X^{(l)}_{VV} + X^{(l)}_{AA} + X^{(l)}_{VA} + X^{(l)}_{AV} \tag{3.31}$$

where V and A denote vector and axial-vector currents, respectively. The decomposition for $\bar{X}^{(l)}$ follows in a similar way. This decomposition will come in handy when discussion the ground-state limit in sec. 3.1.2

3.1.1 Decomposition into longitudinal and transverse components

To extract additional information in the studies of inclusive decays, it proves useful to decompose $X(\boldsymbol{q}^2, \omega)$ into different contributions, i.e. its longitudinal and transverse components. This decomposition provides the possibility to isolate specific physical channels, e.g. the ground state limit which we will consider in the following section 3.1.2 but can also be used for comparison to predictions obtained from different approaches, such as OPE results [42]. To achieve this, we consider a basis in

three-dimensional space created by $e_\parallel$, e_1 and e_2, defined by

$$e_\parallel = \frac{\boldsymbol{q}}{\sqrt{\boldsymbol{q}^2}}\,, \quad e_i e_\parallel = 0\,, \quad e_i e_j = \delta_{ij}\,, \quad i = \{1,2\}\,. \tag{3.32}$$

These basis vectors enable us to construct the longitudinal ($\parallel$) and transverse ($\perp$) projectors

$$\Pi_\parallel^{ij} = \frac{q_i q_j}{\boldsymbol{q}^2}\,, \quad \Pi_\perp^{ij} = \sum_{a=1}^{2} e_a^i e_a^j = \delta^{ij} - \frac{q_i q_j}{\boldsymbol{q}^2}\,, \quad \delta^{ij} = \Pi_\parallel^{ij} + \Pi_\perp^{ij}\,. \tag{3.33}$$

Using these projectors $X(\boldsymbol{q}^2,\omega)$ defined throughout (3.24) - (3.27) is given by

$$\begin{aligned} X(\boldsymbol{q}^2,\omega) &= \boldsymbol{q}^2 W_{00} - q_0 \sum_i q_i (W_{i0} + W_{0i}) + (q_0^2 - \boldsymbol{q}^2) \sum_{i,j} \delta^{ij} W_{ij} + \boldsymbol{q}^2 \sum_{i,j} \frac{q_i W_{ij} q_j}{\boldsymbol{q}^2} \\ &= \boldsymbol{q}^2 W_{00} - q_0 \sum_i q_i (W_{i0} + W_{0i}) + (q_0^2 - \boldsymbol{q}^2) \sum_{i,j} \Pi_\parallel^{ij} W_{ij} + \boldsymbol{q}^2 \sum_{i,j} \Pi_\parallel^{ij} W_{ij} \\ &\quad + (q_0^2 - \boldsymbol{q}^2) \sum_{i,j} \Pi_\perp^{ij} W_{ij}\,. \end{aligned} \tag{3.34}$$

We can now single out the longitudinal and transverse projectors, so that $X(\boldsymbol{q}^2,\omega)$ can be written in terms of longitudinal and transverse contributions, $X_\parallel(\boldsymbol{q}^2,\omega)$ and $X_\perp(\boldsymbol{q}^2,\omega)$, as $X(\boldsymbol{q}^2,\omega) = X_\parallel(\boldsymbol{q}^2,\omega) + X_\perp(\boldsymbol{q}^2,\omega)$. The corresponding contributions read

$$X_\parallel(\boldsymbol{q}^2,\omega) = \boldsymbol{q}^2 W_{00} - q_0 \sum_i q_i (W_{i0} + W_{0i}) + \frac{q_0^2}{\boldsymbol{q}^2} \sum_{i,j} q_i W_{ij} q_j\,, \tag{3.35}$$

$$\begin{aligned} X_\perp(\boldsymbol{q}^2,\omega) &= (q_0^2 - \boldsymbol{q}^2) \sum_{i,j} \left[\delta^{ij} - \frac{q_i q_j}{\boldsymbol{q}^2}\right] W_{ij} \\ &= \left(1 - \frac{q_0^2}{\boldsymbol{q}^2}\right) \left[\sum_i (q_i^2 - \boldsymbol{q}^2) W_{ii} + \sum_{i \neq j} q_i W_{ij} q_j\right]\,. \end{aligned} \tag{3.36}$$

These can once again be expressed in terms of the structure functions,

$$X_\parallel(\boldsymbol{q}^2,\omega) = q^2 W_1 + \boldsymbol{q}^2 W_2\,, \tag{3.37}$$

$$X_\perp(\boldsymbol{q}^2,\omega) = 2 q^2 W_1\,. \tag{3.38}$$

We now obtain the expressions for the decomposition of $X(\boldsymbol{q}^2,\omega)$ into longitudinal and transverse components with respect to the three-momentum $\boldsymbol{q}^2$. The following section presents a practical application of this decomposition.

3.1.2 The ground-state contribution

Following the results obtained in the previous section, we now consider a practical application of the decomposition into longitudinal and transversal components, i.e. we consider the ground-state contribution, which is expected to give the major contribution to the inclusive rate. To this end, we consider a hypothetical case in which we only consider the contribution of the lowest lying energy state towards the inclusive rate, i.e.

$$W^{\mu\nu} \to \delta(\omega - H_{\rm GS}) \frac{1}{4E_{D_s} E_{H_{\rm GS}}} \langle D_s(\boldsymbol{p}_{D_s})|J_\mu^\dagger|H_{\rm GS}(\boldsymbol{p}_{H_{\rm GS}})\rangle \langle H_{\rm GS}(\boldsymbol{p}_{H_{\rm GS}})|J_\nu|D_s(\boldsymbol{p}_{D_s})\rangle \ , \tag{3.39}$$

where $J_\mu = V_\mu, A_\mu$ is either the vector- or axial-vector current, respectively and $H_{\rm GS}$ is the hadronic ground state for the corresponding current. This limit enables a reconstruction of the inclusive decay rate by employing lattice calculations performed for the exclusive decay form factors. The results obtained in this limit can be used as a consistency check on the setup employed for the inclusive decays. For the corresponding matrix elements, their parametrization in the HQET is given as

$$\frac{\langle \eta(v')|V^\mu|D_s(v)\rangle}{\sqrt{m_{D_s} m_\eta}} = h_+(\omega)(v+v')^\mu + h_-(v-v')^\mu \, , \tag{3.40}$$

$$\frac{\langle \phi(v')|V^\mu|D_s(v)\rangle}{\sqrt{m_{D_s} m_\phi}} = h_V(\omega)\epsilon^{\mu\nu\lambda\sigma} v_\mu v'_\lambda \varepsilon^*_\sigma \, , \tag{3.41}$$

$$\frac{\langle \phi(v')|A^\mu|D_s(v)\rangle}{\sqrt{m_{D_s} m_\phi}} = i h_{A_1}(\omega)(1+\omega)\varepsilon^{*\mu} - i\left[h_{A_2}(\omega) v^\mu + h_{A_3}(\omega) v'^\mu\right](\varepsilon^* \cdot v) \, , \tag{3.42}$$

where the kinematics is parametrized using four-velocities $v = p/m_{D_s}$ and $v' = p'/m_{\eta,\phi}$. Further, $h_i(\omega)$ with $i = +, -, V, A_1, A_2, A_3$ denote the form factors in HQET, η and ϕ denote the ground state meson for the corresponding channel and ε^* denotes the polarization vector of the ϕ meson.

Assuming the momentum $\boldsymbol{q}$ in z-direction, i.e. $\boldsymbol{q} = (0, 0, q_z)$, we specifically define longitudinal and transverse components as $p_\parallel = p_z$ and $p_\perp = p_x = p_y$. Similarly, we define all non-vanishing components of the hadronic tensor in the definitions (3.25) - (3.27) as $W_\perp = (W_{11} + W_{22})/2$, $W_\parallel = W_{33}$ and $W_{0\parallel,\parallel 0} = W_{03,30}$ and write

$$X^{(0)}(\boldsymbol{q}^2, \omega) = \boldsymbol{q}^2 \left(W_{00} - 2W_\perp\right) \, , \tag{3.43}$$

$$X^{(1)}(\boldsymbol{q}^2, \omega) = -q_0 q_\parallel (W_{\parallel 0} + W_{0\parallel}) \, , \tag{3.44}$$

$$X^{(2)}(\boldsymbol{q}^2, \omega) = q_0^2 (W_\parallel - 2W_\perp) \, . \tag{3.45}$$

The longitudinal and transverse contributions (3.37) and (3.38) read

$$X_\parallel(\boldsymbol{q}^2,\omega) = \boldsymbol{q}^2 W_{00} - q_0 q_\parallel (W_{\parallel 0} + W_{0\parallel}) + q_0^2 W_\parallel \,, \tag{3.46}$$

$$X_\perp(\boldsymbol{q}^2,\omega) = 2(q_0^2 - \boldsymbol{q}^2) W_\perp \,. \tag{3.47}$$

Combining this with the decomposition (3.31) and inserting the definitions (3.40) - (3.42) into (3.39), we obtain expressions for the longitudinal and transverse components for the vector (VV) or axial-vector (AA) insertions in the hadronic tensor

$$\bar{X}_\parallel^{VV} = \frac{\boldsymbol{q}^2}{4 m_\eta m_{D_s}} \left[h_+(w)(m_{D_s} + m_\eta) - h_-(w)(m_{D_s} - m_\eta) \right]^2 \,, \tag{3.48}$$

$$\bar{X}_\perp^{VV} = \frac{\boldsymbol{q}^2}{2 m_\phi E_\phi} \left[(m_{D_s} - m_\phi)^2 - 2 m_{D_s}(E_\phi - m_\phi) \right] h_V(w)^2 \,, \tag{3.49}$$

$$\begin{aligned} \bar{X}_\parallel^{AA} = \frac{1}{4 m_\phi E_\phi} \Big[& (m_{D_s} - E_\phi)(1+w) h_{A_1}(w) \\ & + \boldsymbol{q}^2 \left(h_{A_1}(w)(1+w) - h_{A_2}(w) - \frac{m_{D_s}}{m_\phi} h_{A_3}(w) \right) \Big]^2 \,, \end{aligned} \tag{3.50}$$

$$\bar{X}_\perp^{AA} = \left[(m_{D_s} - m_\phi)^2 - 2 m_{D_s}(E_\phi - m_\phi) \right] \frac{(1+w)^2}{2w} h_{A_1}(w)^2 \,. \tag{3.51}$$

For $\bar{X}_\parallel^{VV}$ we can simplify this expression to

$$\bar{X}_\parallel^{VV} = \frac{m_{D_s}}{E_\eta} \boldsymbol{q}^2 |f_+(\boldsymbol{q}^2)|^2 \,, \tag{3.52}$$

where we switched the HQET definition of the form factors with the more conventional definition $f_+(\boldsymbol{q}^2)$ defined through

$$\langle \eta(p') | V^\mu | D_s(p) \rangle = f_+(q^2)(p+p')^\mu + f_-(q^2)(p-p')^\mu \,, \tag{3.53}$$

and related to the HQET definition through the relation

$$h_\pm(\omega) = \frac{1}{2\sqrt{m_{D_s} m_\eta}} \left[(m_{D_s} \pm m_\eta) f_+(q^2) + (m_{D_s} \mp m_\eta) f_-(q^2) \right] \,. \tag{3.54}$$

With these expression we are now in a position to calculate the ground state contributions for the different types of current insertions depending on their projection into longitudinal and transversal components with respect to the three-momentum $\boldsymbol{q}^2$. The accuracy of these ground state estimates obviously depend on the precision and availability of the corresponding form factors which can be extracted from, e.g. lattice simulations of the corresponding exclusive modes. We will show some

comparisons between the inclusive and exclusive determination in chapter 4.

3.2 Inclusive decays on an Euclidean space-time lattice

Following the discussion on the continuum version of the inclusive decay rate and the introduction of the expression we try to approximate, i.e. the energy integral over hadronic final states $\bar{X}(\omega)$, the next step is to focus on the computation strategy of the inclusive decays on the lattice. This section follows [29, 42, 93, 98]. Towards this end, the key quantity that we consider is the hadronic tensor (3.3)

$$W^{\mu\nu}(q) = \frac{1}{M_{D_s}} \int d^4x e^{iqx} \langle D_s | J^{\mu\dagger}(x) J^{\nu}(0) | D_s \rangle \ . \tag{3.55}$$

On the lattice, as a counterpart to (3.55), we consider the time dependence of the Euclidean four-point function

$$C^{SJJS}_{\mu\nu}(\boldsymbol{q}, t_{\text{snk}}, t_2, t_1, t_{\text{src}}) \overset{t_2 \geq t_1}{=} \langle \mathcal{O}^S_{D_s}(x_{\text{snk}}) \tilde{J}^{\dagger}_{\mu}(\boldsymbol{q}, t_2) \tilde{J}_{\nu}(\boldsymbol{q}, t_1) \mathcal{O}^{S\dagger}_{D_s}(x_{\text{src}}) \rangle \ , \tag{3.56}$$

where $\mathcal{O}^S_{D_s}$ defines an interpolating operator possessing the quantum numbers of the D_s meson and $\tilde{J}_{\nu}(\boldsymbol{q}, t) = \sum_{\boldsymbol{x}} \exp(i\boldsymbol{q}\boldsymbol{x}) J_{\nu}(\boldsymbol{x}, t)$ is a discrete Fourier transform, projecting the currents onto three-momentum. This setup creates a D_s meson that carries zero momentum at source point x_{src} which is annihilated at sink point x_{snk}. The corresponding quark flow diagram is shown in Fig. 3.2 and can be understood in the following way. The propagator of the c quark from position x_1 to x_{src}, $G_c(x_{\text{src}}, x_1)$, is represented by the black line. The green line, $\Sigma_{scs}(x_1, x_{\text{src}})$, defines a sequential propagator, propagating the s quark from x_{src} to x_{snk}, the c quark from x_{snk} to x_2 and finally the s quark from x_2 to x_1.

Let us now turn towards an deeper understanding of the correlation between the matrix element (3.55) and the four-point function (3.56). To this end, let us start by first defining the window in which an extraction of (3.55) is possible. The conditions we have to satisfy are $t_{\text{snk}} - t_2 \gg 0$, $t_1 - t_{\text{src}} \gg 0$ and $t_2 > t_1$. This is to ensure that the excited states of the D_s meson have dumped sufficiently. To enlarge the applicable window we consider operator smearing, i.e. we increase the overlap of the operator $\mathcal{O}^S_{D_s}$ with the ground state D_s meson. This is specified by the superscripts S and L, denoting smeared and unsmeared operators, respectively. More details on the smearing will be given in Ch. 4.

Within the valid window for the ground-state saturation, the four-point function is expected to

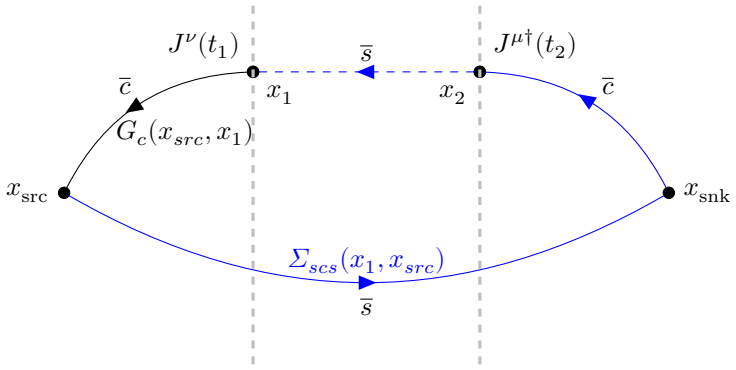

Figure 3.2: Schematic representation of the diagram for the four-point correlator. The contraction depicted here are based on two propagators. First, we have $G_c(x_{\rm src}, x_1)$ depicted by the black line, which propagates the c quark from x_1 to $x_{\rm src}$. Secondly, we have $\sum_{scs}(x_1, x_{\rm src})$ depicted by the blue line, is a sequential propagator used to propagate the s quark from $x_{\rm src}$ to $x_{\rm snk}$, the c quark from $x_{\rm snk}$ to x_2 and the s quark from x_2 to x_1.

take the form

$$C^{SJJS}_{\mu\nu}(\boldsymbol{q}, t_{\rm snk}, t_2, t_1, t_{\rm snk}) = \frac{1}{4M^2_{D_s}} \langle 0|\mathcal{O}^S_{D_s}|D_s\rangle \langle D_s|\tilde{J}^{\dagger}_{\mu}(\boldsymbol{q}, t_2)\tilde{J}_{\nu}(\boldsymbol{q}, t_1)|D_s\rangle \langle D_s|\mathcal{O}^{S\dagger}_{D_s}|0\rangle \ . \tag{3.57}$$

It is already possible to identify the forward-scattering matrix element (3.55) in (3.57). But a proper extraction requires us to cancel the smeared D_s wave function factors $\langle 0|\mathcal{O}^S_{D_s}|D_s\rangle$ and $\langle D_s|\mathcal{O}^{S\dagger}_{D_s}|0\rangle$. We achieve this by constructing suitable ratios with zero momentum two-point functions of the D_s meson

$$C^{SS}(t_2, t_1) = \sum_{x_1, x_2} \langle \mathcal{O}^S_{D_s}(x_2)\mathcal{O}^{S\dagger}_{D_s}(x_1)\rangle \tag{3.58}$$

$$\overset{t_2-t_1\gg 0}{=} \frac{1}{2M_{D_s}} \langle 0|\mathcal{O}^S_{D_s}|D_s\rangle \langle D_s|\mathcal{O}^{S\dagger}_{D_s}|0\rangle \, e^{-(t_2-t_1)M_{D_s}} \ . \tag{3.59}$$

We define a ratio

$$\frac{C^{SJJS}_{\mu\nu}(\boldsymbol{q}, t_{\rm snk}, t_2, t_1, t_{\rm snk})}{C^{SS}(t_{\rm snk}, t_2)C^{SS}(t_1, t_{\rm src})} \to \frac{\frac{1}{2M_{D_s}} \langle D_s|\tilde{J}^{\dagger}_{\mu}(\boldsymbol{q}, t_2)\tilde{J}_{\nu}(\boldsymbol{q}, t_1)|D_s\rangle}{\frac{1}{2M_{D_s}} \left|\langle 0|\mathcal{O}^S_{D_s}|D_s\rangle\right|^2} \ , \tag{3.60}$$

where the additional factor $\frac{1}{2M^2_{D_s}} \left|\langle 0|\mathcal{O}^S_{D_s}|D_s\rangle\right|^2$ appearing in the denominator on the r.h.s. of (3.60) can be evaluated from time-dependent fits to the C^{SL} and C^{LS} two-point functions. It is also possible to define different ratios, such as, e.g., employing a combination of C^{SL} and C^{LS}, as was

done in [93]. We then employ time invariance $t = t_2 - t_1$ to obtain

$$C_{\mu\nu}(\boldsymbol{q}, t) = \frac{1}{2M_{D_s}} \langle D_s | \tilde{J}^\dagger_\mu(\boldsymbol{q}, 0) e^{-\hat{H}t} \tilde{J}_\nu(\boldsymbol{q}, 0) | D_s \rangle \ . \tag{3.61}$$

We are now able to relate this quantity to the hadronic tensor (3.55) through a Laplace transform

$$\begin{aligned} C_{\mu\nu}(\boldsymbol{q}, t) &= \int_0^\infty d\omega \frac{1}{2M_{D_s}} \langle D_s | \tilde{J}^\dagger_\mu(\boldsymbol{q}, 0) \delta(\hat{H} - \omega) \tilde{J}_\nu(\boldsymbol{q}, 0) | D_s \rangle \, e^{-\omega t} \\ &= \int_0^\infty d\omega W_{\mu\nu}(\boldsymbol{q}, \omega) e^{-\omega t} \, . \end{aligned} \tag{3.62}$$

Here, we have

$$W_{\mu\nu} = \frac{1}{2M_{D_s}} \sum_{X_s} \delta(\omega - E_{X_s}) \langle D_s | \tilde{J}^\dagger_\mu(\boldsymbol{q}, 0) | X_s \rangle \langle X_s | \tilde{J}_\nu(\boldsymbol{q}, 0) | D_s \rangle \ , \tag{3.63}$$

which corresponds to the spectral representation of $C_{\mu\nu}(\boldsymbol{q}, t)$. The lattice determination of $C_{\mu\nu}$ is enabled through the definition (3.60), i.e. a combination of two- and four-point correlation functions with a finite and discrete set of Euclidean time t.

As mentioned in the introduction of this chapter, the extraction of hadronic spectral densities from hadronic correlators is an ill-posed problem, commonly referred to as the inverse problem, and the extraction of the hadronic tensor through inversion of the integral defined in (3.62) falls under the same category, i.e. the reconstruction of $C_{\mu\nu}$ is trivial if $W_{\mu\nu}$ is known, while the other way around is not straightforward at all.

Luckily, we are not required to calculate the hadronic tensor itself in order to compute the inclusive decay rate (3.28), but instead only require integrals $\bar{X}^{(l)}(\boldsymbol{q}^2)$ defined through Eqs. (3.28)-(3.30), in which the hadronic tensor is *smeared* with the leptonic tensor integrated over the lepton energy.

In a more general sense, the energy integral $\bar{X}^{(l)}(\boldsymbol{q}^2)$ can be written as

$$\bar{X}^{(l)}(\boldsymbol{q}^2) = \int_{\omega_{\min}}^{\omega_{\max}} d\omega W^{\mu\nu}(\boldsymbol{q}, \omega) k^{(l)}_{\mu\nu}(\boldsymbol{q}, \omega) \, , \tag{3.64}$$

where $k^{(l)}_{\mu\nu}(\boldsymbol{q}, \omega)$ is an analytically known function depending only on the three-momentum $\boldsymbol{q}$ and the energy ω. We manipulate the integral by shifting the limits of integration as $\omega_{\min} \to \omega_0$, with $\omega_0 \leq \omega_{\min}$ and $\omega_{\max} \to \infty$, introducing a step function $\theta(\omega_{\max} - \omega)$ to cut off all contributions above

$\omega_{\max}$:

$$\begin{aligned}\bar{X}^{(l)}(\boldsymbol{q}^2) &= \int_{\omega_0}^{\infty} d\omega W^{\mu\nu}(\boldsymbol{q},\omega) k^{(l)}_{\mu\nu}(\boldsymbol{q},\omega)\theta(\omega_{\max}-\omega) \\ &= \int_{\omega_0}^{\infty} d\omega W^{\mu\nu}(\boldsymbol{q},\omega) K^{(l)}_{\mu\nu}(\boldsymbol{q},\omega)\,,\end{aligned} \tag{3.65}$$

where in the second step we defined $K^{(l)}_{\mu\nu}(\boldsymbol{q},\omega) = k^{(l)}_{\mu\nu}(\boldsymbol{q},\omega)\theta(\omega_{\max}-\omega)$. We will refer to it as the *kernel function*. The lower limit ω_0 can be chosen freely in the range $0 \le \omega_0 \le \omega_{\min}$, because there is no state below the lowest lying energy state $\omega_{\min}$. In the case of $D_s \to X_s \ell \nu_\ell$, this corresponds to $\omega_{\min} = \sqrt{M_\eta^2 + \boldsymbol{q}^2}$. In Ch. 4, this freedom of ω_0 will be exploited further.

The next topic of interest is the determination of $\bar{X}^{(l)}$ using the lattice data for $C_{\mu\nu}(\boldsymbol{q},t)$ defined in (3.61). We replace the sharp cut of the step function $\theta(\omega_{\max}-\omega)$ by a smooth one in the form of a sigmoid function

$$\theta_\sigma(x) = \frac{1}{1+e^{-x/\sigma}}\,, \tag{3.66}$$

where the degree of smoothing is controlled by the smearing parameter σ. The $\sigma \to 0$ limit is needed to restore the physical decay rate, but the smearing is useful to gain a better control and understanding of the systematic effects involved in the computation strategy of the decay rate. In Sec. 3.4.1, we will discuss a method which allows us to estimate the corrections due to the $\sigma \to 0$ extrapolation. We now expand the kernel $K^{(l)}_{\sigma,\mu\nu}(\boldsymbol{q},\omega)$ in polynomials of $\exp(-a\omega)$ (for simplicity, we will set $a = 1$) up to some order N, following [29]

$$K^{(l)}_{\sigma,\mu\nu}(\boldsymbol{q},\omega) \simeq c^{(l)}_{\mu\nu,0}(\boldsymbol{q};\sigma) + c^{(l)}_{\mu\nu,1}(\boldsymbol{q};\sigma)e^{-\omega} + \cdots + c^{(l)}_{\mu\nu,N}(\boldsymbol{q};\sigma)e^{-N\omega}\,. \tag{3.67}$$

Our target quantity $\bar{X}^{(l)}(\boldsymbol{q}^2)$ can then be calculated following

$$\begin{aligned}\bar{X}^{(l)}_\sigma &= \int_{\omega_0}^{\infty} d\omega W^{\mu\nu}(\boldsymbol{q},\omega) e^{-2\omega t_0} K^{(l)}_{\sigma,\mu\nu}(\boldsymbol{q},\omega,t_0) \\ &\simeq c^{(l)}_{\mu\nu,0}\int_{\omega_0}^{\infty} d\omega W^{\mu\nu}(\boldsymbol{q},\omega) e^{-2\omega t_0} + c^{(l)}_{\mu\nu,1}\int_{\omega_0}^{\infty} d\omega W^{\mu\nu}(\boldsymbol{q},\omega) e^{-2\omega t_0} e^{-\omega} + \cdots \\ &+ c^{(l)}_{\mu\nu,N}\int_{\omega_0}^{\infty} d\omega W^{\mu\nu}(\boldsymbol{q},\omega) e^{-2\omega t_0} e^{-N\omega}\,,\end{aligned} \tag{3.68}$$

where we introduce an additional dependence on the smearing parameter σ. We have furthermore introduced the factor $e^{-2\omega t_0}$ in the first line of (3.68), which we compensate in the kernel function $K^{(l)}_{\sigma,\mu\nu}(\boldsymbol{q},\omega;t_0) = e^{2\omega t_0} K^{(l)}_{\sigma,\mu\nu}(\boldsymbol{q},\omega)$. The purpose of this term is to avoid the contact term of $t_1 = t_2$ appearing in (3.56), since this element receives contribution from the opposite time ordering

corresponding to unphysical $\bar{c}ss\bar{c}$ final states. Further details on the discussion of suitable choices of t_0 will follow in Ch. 4 together with a discussion on the actual analysis strategy of the lattice data. By comparing (3.62) and (3.68) we can write

$$\bar{X}_\sigma^{(l)}(\boldsymbol{q}^2) = \sum_{k=0}^{N} c_{\mu\nu,k}^{(l)} C^{\mu\nu}(\boldsymbol{q}, k + 2t_0)\,. \tag{3.69}$$

This expression finally gives a relation between $C^{\mu\nu}(\boldsymbol{q}, t)$, which is a quantity calculated on the lattice, and $\bar{X}_\sigma^{(l)}(\boldsymbol{q}^2)$ appearing in the total decay rate. (3.69) has to be understood as an approximation due to the truncation at a finite order N. Furthermore, with this new setup, the order N of the polynomial approximation is equal to the Euclidean time separation between the inserted currents in the four-point function (3.56). For any given value of σ, the only remaining task towards a determination of the decay rate is to perform the phase-space or $\boldsymbol{q}^2$ integration in Eq. (3.28).

Let us close this section by listing the explicit expression for the kernels $K_{\sigma,\mu\nu}^{(l)}$, where the kinematical factors can be extracted through comparison with the relations given in (3.30)

$$K_{\sigma,00}^{(0)}(\boldsymbol{q}, \omega; t_0) = e^{2\omega t_0} \boldsymbol{q}^2 \theta_\sigma(\omega_{\max} - \omega)\,, \tag{3.70}$$

$$K_{\sigma,ii}^{(0)}(\boldsymbol{q}, \omega; t_0) = e^{2\omega t_0} (q_i^2 - \boldsymbol{q}^2) \theta_\sigma(\omega_{\max} - \omega)\,, \tag{3.71}$$

$$K_{\sigma,ij}^{(0)}(\boldsymbol{q}, \omega; t_0) \overset{i\neq j}{=} e^{2\omega t_0} q_i q_j \theta_\sigma(\omega_{\max} - \omega)\,, \tag{3.72}$$

$$K_{\sigma,0i}^{(1)}(\boldsymbol{q}, \omega; t_0) = K_{\sigma,0i}^{(1)} = -e^{2\omega t_0} q_i q_0 \theta_\sigma(\omega_{\max} - \omega)\,, \tag{3.73}$$

$$K_{\sigma,ii}^{(2)}(\boldsymbol{q}, \omega; t_0) = e^{2\omega t_0} q_0^2 \theta_\sigma(\omega_{\max} - \omega)\,. \tag{3.74}$$

The logintudinal and transverse projections defined in Sec. 3.1.2 of $\boldsymbol{q}^2 \neq 0$ are then given by

$$K_{\sigma,00}^{\parallel}(\boldsymbol{q}, \omega; t_0) = e^{2\omega t_0} \boldsymbol{q}^2 \theta_\sigma(\omega_{\max} - \omega)\,, \tag{3.75}$$

$$K_{\sigma,0i}^{\parallel}(\boldsymbol{q}, \omega; t_0) = -e^{2\omega t_0} q_0 q_i \theta_\sigma(\omega_{\max} - \omega)\,, \tag{3.76}$$

$$K_{\sigma,ij}^{\parallel}(\boldsymbol{q}, \omega; t_0) = e^{2\omega t_0} \frac{q_0^2}{\boldsymbol{q}^2} \theta_\sigma(\omega_{\max} - \omega)\,, \tag{3.77}$$

and

$$K_{\sigma,ii}^{\perp}(\boldsymbol{q}, \omega; t_0) = e^{2\omega t_0} (q_i^2 - \boldsymbol{q}^2) \theta_\sigma(\omega_{\max} - \omega)\,, \tag{3.78}$$

$$K_{\sigma,ij}^{\perp}(\boldsymbol{q}, \omega; t_0) \overset{i\neq j}{=} e^{2\omega t_0} q_i q_j \left(1 - \frac{q_0^2}{\boldsymbol{q}^2}\right) \theta_\sigma(\omega_{\max} - \omega)\,, \tag{3.79}$$

respectively. All other combinations of indices not shown above vanish.

3.3 Lattice data analysis strategy

Following the discussion of the previous section, we have now developed a method that reduces the problem on the calculation of inclusive decay rate to the one that requires finding a suitable polynomial approximation for the kernel function $K^{(l)}_{\sigma,\mu\nu}(\boldsymbol{q},\omega;t_0)$. In the literature, there are two proposed methods to determine the expansion coefficients $c^{(l)}_{\mu\nu,k}$ through the ratio of lattice data defined in (3.60), namely the Backus-Gilbert method [42, 99–101] and the Chebyshev polynomial approach [29, 102, 103]. This work will employ the latter of these two, and we refer the interested reader to the aforementioned references for the Backus-Gilbert method.

Turning towards the analysis, there are two major obstacles that we have to deal with, i.e. statistical noise from the lattice data and systematic errors, e.g. those induced due to the finite order N in the polynomial approximation or finite-volume corrections. The topic on how to estimate the aforementioned two sources of systematic errors will be discussed in the following section. Since this work only employs lattice data generated at a single lattice spacing and volume, a discussion on discretization effects will not be addressed in this work, although they are expected to be well under control for the charm sector.

Before turning to the discussion on the polynomial approximation strategy let us picture our current situation. Naively, it should be possible to compute $\bar{X}^{(l)}_{\sigma}(\boldsymbol{q}^2)$, as given in (3.69), straightforwardly from lattice data for $C_{\mu\nu}(\boldsymbol{q},t)$. Since the kernel $K^{(l)}_{\sigma,\mu\nu}(\boldsymbol{q},\omega)$ is an analytically known object, it should be possible to determine the coefficients $c^{(l)}_{\mu\nu,k}$ appearing in the power series of the kernel through, e.g. a linear regression, enabling a reconstruction of $\bar{X}^{(l)}_{\sigma}(\boldsymbol{q}^2)$ through lattice data for $C_{\mu\nu}(\boldsymbol{q},t)$. The only limiting factor in such a scenario should be the order N of the expansion, since this number directly correspond to the number of available time slices in the window where $C_{\mu\nu}(\boldsymbol{q},t)$ can be extracted. Unfortunately, this naive scenario is rendered invalid by the fact that the signal-to-noise ratio deteriorates exponentially for increasing time separation in Euclidean time t, meaning that the extraction of a meaningful signal becomes difficult. This necessitates some kind of regulator controlling the trade-off between statistical noise and systematic error due to the truncation in the expansion. This is achieved by the previously mentioned Backus-Gilbert method and the Chebyshev polynomials.

Finally, let us close this introduction by introducing the following notation

$$\begin{aligned}\bar{X}^{(l)}_{\sigma}(\boldsymbol{q}^2) &= \int_{\omega_0}^{\infty} d\omega W^{\mu\nu}(\boldsymbol{q},\omega) e^{-2\omega t_0} K^{(l)}_{\sigma,\mu\nu}(\boldsymbol{q},\omega;t_0) \\ &= \frac{1}{2M_{D_s}} \int_{\omega_0}^{\infty} d\omega K^{(l)}_{\sigma,\mu\nu}(\boldsymbol{q},\omega;t_0) \, \langle D_s | \tilde{J}^{\mu\dagger}(\boldsymbol{q},0) e^{-\omega t_0} \delta(\hat{H}-\omega) e^{-\omega t_0} \tilde{J}^{\nu}(\boldsymbol{q},0) | D_s \rangle \\ &= \langle \psi^{\mu}(\boldsymbol{q}) | K^{(l)}_{\sigma,\mu\nu}(\boldsymbol{q},\hat{H};t_0) | \psi^{\nu}(\boldsymbol{q}) \rangle \ ,\end{aligned} \tag{3.80}$$

making use of (3.63) and introducing the definition $|\psi^{\nu}(\boldsymbol{q})\rangle = e^{-\hat{H}t_0 \tilde{J}^{\nu}(\boldsymbol{q},0)} |D_s\rangle / \sqrt{2M_{D_s}}$. In (3.80)

the kernel has been promoted to an operator, $K^{(l)}_{\sigma,\mu\nu}(\boldsymbol{q}, \hat{H}; t_0)$.

3.3.1 Chebyshev polynomial approximation

We now focus on the details of the Chebyshev polynomials. Chebyshev polynomials $T_k(x)$ with $x = \exp(-\omega)$ are a class of polynomials defined for $-1 \leq x \leq 1$ and provide an optimal approximation of functions under the L_∞-norm. We refer to app. A for a discussion on properties of the Chebyshev polynomials useful for this work. For the application considered in this work, we define shifted Chebyshev polynomials $\tilde{T}_k(x)$ defined in the interval $\omega_0 \leq \omega \leq \infty$. The shifted Chebyshev polynomials are related to the standard definition through $\tilde{T}_k(x) = T_k(h(x))$, where $h(x) = Ax + B$ is a mapping function $h : [\omega_0, \infty) \to [-1, 1]$. While a more detailed discussion on the coefficients A and B can be found in app. A, here we shall only give their dependence on the choice of ω_0

$$A = -2e^{\omega_0} \quad \text{and} \quad B = 1\,. \tag{3.81}$$

With this, we can expand the kernel function defined in the previous section as

$$K^{(l)}_{\sigma,\mu\nu}(\boldsymbol{q}, \hat{H}; t_0) = \frac{1}{2}\tilde{c}^{(l)}_{\mu\nu,0}\tilde{T}_0(x) + \sum_{k=1}^{N} \tilde{c}^{(l)}_{\mu\nu,k}\tilde{T}_k(x)\,, \tag{3.82}$$

up to order N. By definition, we have $\tilde{T}_0(x) = 1$ and the k-th term is given by

$$\tilde{T}_k(x) = \sum_{j=0}^{k} \tilde{t}^{(k)}_j x^j\,, \tag{3.83}$$

where we refer to (A.4) in the appendix for the detailed definitions of the coefficients $\tilde{t}^{(k)}_j$. By employing the orthogonality properties of the Chebyshev polynomials, the coefficients $\tilde{c}^{(l)}_{\mu\nu,k}$ are given by projections as shown in (A.6)

$$\tilde{c}^{(l)}_{\mu\nu,k} = \int_{\omega_0}^{\infty} d\omega K^{(l)}_{\sigma,\mu\nu}(\boldsymbol{q}, \omega; t_0)\tilde{T}_k(e^{-\omega})\Omega_h(\omega)\,. \tag{3.84}$$

The definition of the weight function $\Omega_h(\omega)$ depends on the choice of the map h and is given in App. A. Following this definition, the expectation value of the kernel operator can be written as

$$\langle\psi^\mu|K^{(l)}_{\sigma,\mu\nu}(\boldsymbol{q}, \hat{H}; t_0)|\psi^\nu\rangle = \frac{1}{2}\tilde{c}^{(l)}_{\mu\nu,0}\,\langle\psi^\mu|\tilde{T}_0(\hat{H})|\psi^\nu\rangle + \sum_{k=1}^{N} \tilde{c}^{(l)}_{\mu\nu,k}\,\langle\psi^\mu|\tilde{T}_k(\hat{H})|\psi^\nu\rangle\,. \tag{3.85}$$

Furthermore, the shifted Chebyshev polynomials are bounded $|\tilde{T}_k| \leq 1$ by definition, as can be seen through condition (A.9). This property will become an important ingredient in the data analysis,

and more details can be found in the discussions in Ch. 4. To actually employ this property, we normalize the terms $\langle\psi^\mu|\tilde{T}_k(\hat{H})|\psi^\nu\rangle$ by $\langle\psi^\mu|\psi\nu\rangle = C^{\mu\nu}(2t_0)$ and introduce the short-hand notation

$$\langle K_\sigma^{(l)}\rangle_{\mu\nu} \equiv \frac{\langle\psi^\mu|K^{(l)}_{\sigma,\mu\nu}(\boldsymbol{q},\omega;t_0)|\psi^\nu\rangle}{\langle\psi^\mu|\psi^\nu\rangle}\,, \quad \langle\tilde{T}_k\rangle_{\mu\nu} \equiv \frac{\langle\psi^\mu|\tilde{T}_k(\hat{H})|\psi^\nu\rangle}{\langle\psi^\mu|\psi^\nu\rangle}\,, \tag{3.86}$$

so that (3.85) can be rewritten as

$$\langle K_\sigma^{(l)}\rangle_{\mu\nu} = \frac{1}{2}\tilde{c}^{(l)}_{\mu\nu,0}\,\langle\tilde{T}_0\rangle_{\mu\nu} + \sum_{k=1}^{N}\tilde{c}^{(l)}_{\mu\nu,k}\,\langle\tilde{T}_k\rangle_{\mu\nu}\,. \tag{3.87}$$

No summation over μ,ν is assumed. The terms $\langle\tilde{T}_k\rangle_{\mu\nu}$ are referred to as *Chebyshev matrix elements*, which satisfy the condition $|\,\langle\tilde{T}_k\rangle_{\mu\nu}\,| \leq 1$. Moreover, the expression for $\bar{X}^{(l)}_\sigma(\boldsymbol{q}^2)$ can be given in terms of the Chebyshev expansion

$$\bar{X}^{(l)}_\sigma(\boldsymbol{q}^2) = \sum_{\{\mu,\nu\}}\langle\psi^\mu|\psi^\nu\rangle\,\langle K_\sigma^{(l)}\rangle_{\mu\nu}\,. \tag{3.88}$$

The explicit relation for each value of l then read

$$\bar{X}^{(0)}_\sigma(\boldsymbol{q}^2) = C_{00}(2t_0)\,\langle K_\sigma^{(0)}\rangle_{00} + \sum_i C_{ii}(2t_0)\,\langle K_\sigma^{(0)}\rangle_{ii} + \sum_{i\neq j}C_{ij}(2t_0)\,\langle K_\sigma^{(0)}\rangle_{ij}\,, \tag{3.89}$$

$$\bar{X}^{(1)}_\sigma(\boldsymbol{q}^2) = \sum_i\left(C_{0i}(2t_0)\,\langle K_\sigma^{(1)}\rangle_{0i} + C_{i0}(2t_0)\,\langle K_\sigma^{(1)}\rangle_{i0}\right)\,, \tag{3.90}$$

$$\bar{X}^{(2)}_\sigma(\boldsymbol{q}^2) = \sum_i C_{ii}(2t_0)\,\langle K_\sigma^{(2)}\rangle_{ii}\,. \tag{3.91}$$

It is possible to directly relate the lattice data to the Chebyshev matrix elements through the relation

$$\frac{\langle\psi^\mu|e^{-\hat{H}t}|\psi^\nu\rangle}{\langle\psi^\mu|\psi^\nu\rangle} = \frac{C_{\mu\nu}(t+2t_0)}{C_{\mu\nu}(2t_0)} \equiv \bar{C}_{\mu\nu}(t)\,. \tag{3.92}$$

We can then formulate a direct relation between the correlator $\bar{C}_{\mu\nu}(t)$ and the Chebyshev matrix elements $\langle\tilde{T}_k\rangle_{\mu\nu}$ by employing the properties of the shifted Chebyshev polynomials highlighted in

App. A.2

$$\begin{aligned}\langle \tilde{T}_k \rangle_{\mu\nu} &= \frac{\langle \psi^\mu | \tilde{T}_k(\hat{H}) | \psi^\nu \rangle}{\langle \psi^\mu | \psi^\nu \rangle} = \sum_{X_s} \frac{\langle \psi^\mu | \tilde{T}_k(\hat{H}) | X_s \rangle \langle X_s | \psi^\nu \rangle}{\langle \psi^\mu | \psi^\nu \rangle} \\ &= \sum_{X_s} \sum_{j=0}^{k} \tilde{t}_j^{(k)} e^{-jE_{X_s}} \frac{\langle \psi^\mu | X_s \rangle \langle X_s | \psi^\nu \rangle}{\langle \psi^\mu | \psi^\nu \rangle} \\ &= \sum_{j=0}^{k} \tilde{t}_j^{(k)} \bar{C}_{\mu\nu}(j) \,.\end{aligned} \tag{3.93}$$

Here, we have inserted $\mathbb{1} = \sum_{X_s} |X_s\rangle \langle X_s|$ and the $\tilde{t}_j^{(k)}$ are defined in (A.16).

Combining everything, the full expression of the kernel in terms of the Chebyshev expansion reads

$$\begin{aligned}\langle K_\sigma^{(l)} \rangle_{\mu\nu} &= \frac{1}{2} \tilde{c}_{\mu\nu,0}^{(l)} \langle \tilde{T}_0 \rangle_{\mu\nu} + \sum_{k=1}^{N} \tilde{c}_{\mu\nu,k}^{(l)} \langle \tilde{T}_k \rangle_{\mu\nu} \\ &= \sum_{k=0}^{N} \bar{C}_{\mu\nu}(k) \sum_{j=k}^{N} \tilde{c}_{\mu\nu,j}^{(l)} \left(1 - \frac{1}{2}\delta_{0j}\right) \tilde{t}_k^{(j)} \,,\end{aligned} \tag{3.94}$$

where the expressions for the coefficients $\tilde{c}_{\mu\nu,j}^{(l)}$ and $\tilde{t}_k^{(j)}$ are known and can be evaluated analytically. Finally, let us present a short-handed notation

$$\langle K_\sigma^{(l)} \rangle_{\mu\nu} = \sum_{k=0}^{N} \bar{c}_{\mu\nu,k}^{(l)} \bar{C}_{\mu\nu}(k) \,, \tag{3.95}$$

where we have combined the coefficient following the definition

$$\bar{c}_{\mu\nu,k}^{(l)} \equiv \sum_{j=k}^{N} \tilde{c}_{\mu\nu,j}^{(l)} \tilde{t}_k^{(j)} \left(1 - \frac{1}{2}\delta_{0j}\right) \,. \tag{3.96}$$

Let us close this section with some remarks. Although the coefficients $\bar{c}_{\mu\nu,k}^{(l)}$ can be obtained through solving the corresponding analytical expression, the lattice computation of $\bar{C}_{\mu\nu}(k)$ relies on Monte-Carlo simulations. This means that $\bar{C}_{\mu\nu}(k)$ is associated with an statistical error, which, in return, means that solving the linear system in (3.93) might result in violations of the bound $|\langle \tilde{T}_k \rangle_{\mu\nu}| \leq 1$. One viable option to avoid this problem during a Bayesian analysis of the correlator data is to introduce the bound through priors during the fitting procedure. One possibility to impose this constraint is to employ a Gaussian prior on some internal parameters $\langle \tilde{\tau} \rangle_{\mu\nu} \sim \mathcal{N}(0,1)$, which is then mapped into a flat prior in the interval $[-1,1]$ using $f(x) = \mathrm{erf}(x/\sqrt{2})$, so that $\langle \tilde{T}_k \rangle_{\mu\nu} = f\left(\langle \tilde{\tau} \rangle_{\mu\nu}\right)$.

3.4 Systematic errors in the inclusive decays

In this section we discuss the systematic errors associated with the inclusive analysis strategy. We analyze the systematic errors introduced by the approximation [104] and the error due to finite volume effects. The former is a combination of two effects: first, the smoothing of the kernel function requires the $\sigma \to 0$ limit and secondly, the truncation of the Chebyshev approximation at polynomial order N requires the $N \to \infty$ limit. We address this in sec. 3.4.1.

The error due to finite volume effects is a general problem for any calculations performed on the lattice. A famous example on these can be estimated is given by the Lellouch-Lüscher formula [105, 106] relating the finite-volume calculation of $K \to 2\pi$ matrix elements to their infinite-volume counterpart. Conventionally, the finite volume is estimated by extrapolating the results from the same calculation for different choices of finite volumes. We address the topic on how an estimate can be obtained if sufficient data is not available. While the reconstruction of spectral densities in inclusive decays has been addressed in [107], we develop a modeling strategy to estimate finite volume corrections under some assumptions. We discuss our motivations and methodology in sec. 3.4.2.

3.4.1 Corrections due to finite polynomial approximation

We discuss the systematic error associated with the Chebyshev approximation and the smearing of the kernel function which we addressed in [104]. The two relevant limits are the $\sigma \to 0$ and $N \to \infty$ limits. We consider the kernel function

$$K^{(l)}_{(\sigma)}(\boldsymbol{q}^2, \omega; t_0) = e^{2\omega t_0} \sqrt{\boldsymbol{q}^2}^{2-l} (m_{D_s} - \omega)^l \theta_{(\sigma)}(m_{D_s} - \sqrt{\boldsymbol{q}^2} - \omega)\,. \tag{3.97}$$

In the following we drop the dependence on $\boldsymbol{q}^2$ and t_0 for simplicity and ignore the term $\sqrt{\boldsymbol{q}^2}^{2-l}$ since it is a simple pre-factor, i.e. we consider $\bar{K}(\omega)$ defined through

$$K^{(l)}_{(\sigma)}(\omega) = \sqrt{\boldsymbol{q}^2}^{2-l} \bar{K}^{(l)}_{(\sigma)}(\omega)\,. \tag{3.98}$$

We further consider two cases on how the upper limit of the integration is implemented, i.e. a step function $\theta(x)$ or a sigmoid function $\theta_\sigma(x)$ with smearing σ. We refer to the kernel with a Heaviside function as the *unsmeared kernel* while the kernel with a sigmoid function will be referred to as the *smeared kernel*. As in sec. 3.1, the superscript l denotes the powers of $\boldsymbol{q}^2$ and $q_0 = m_{D_s} - \omega$.

In Fig. 3.3 we compare the smeared and unsmeared kernel for $l = 0, 2$. We include the region of allowed phase space by the gray-shaded area for $\boldsymbol{q}^2 = 0\,\mathrm{GeV}^2$. While we see non-negligible differences for $l = 0$ between the two choices, the differences for $l = 2$ seem to be negligible. The reason for this is obvious, while for $l = 0$ the unsmeared kernel possesses a sharp cut, the kinematical limit

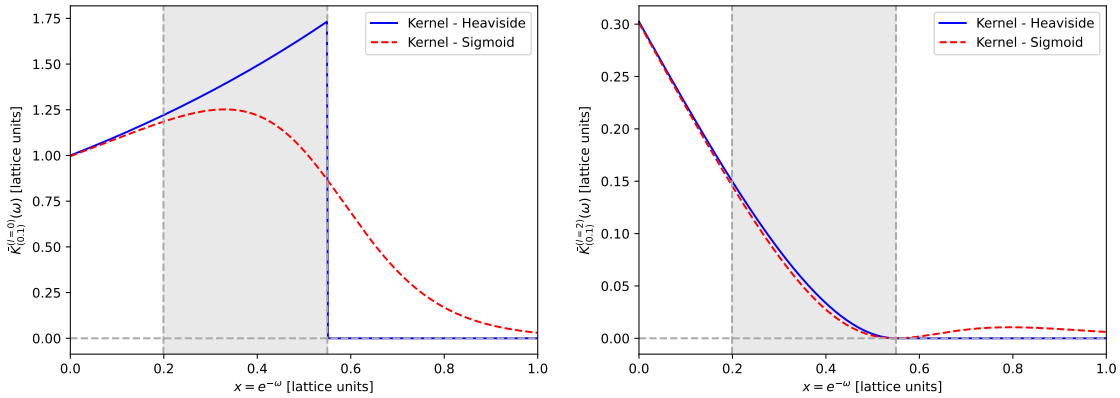

(a) $l = 0$. (b) $l = 2$.

Figure 3.3: Comparison to highlight the differences in the kernel function depending on the choice of the heaviside or sigmoid function. The heaviside function in both plots is represented by the solid line, while the sigmoid function uses the dashed line.

$\omega_{\max} = m_{D_s} - \sqrt{\boldsymbol{q}^2}$ for $l = 2$ is approached smoothly due to the kinematical factor $(m_{D_s} - \omega)^l$. Therefore, the expected systematic error due to the smearing depends on l.

Next, we consider the Chebyshev approximation of the smeared kernel which, in terms of the shifted Chebyshev polynomials, is defined as

$$\bar{K}^{(l)}_{(\sigma)}(\omega) \simeq \frac{\tilde{c}_0}{2} + \sum_{j=1}^{n} \tilde{c}^{(l)}_j \tilde{T}_j(e^{-\omega}) \,, \tag{3.99}$$

where the coefficients $\tilde{c}_j$ can be determined through

$$\tilde{c}^{(l)}_j = \frac{2}{\pi} \int_0^\pi d\theta \bar{K}^{(l)}_{(\sigma)} \left(-\ln\left(\frac{\cos\theta - 1}{-2} \right) \right) \cos\left(j\theta\right) \,. \tag{3.100}$$

Additional discussions on the Chebyshev approximation can be found in App. A. This section only considers the case $\omega_0 = 0$, i.e. we employ the map $h : [0, \infty) \to [-1, 1]$ so that the shifted Chebyshev polynomials are defined by

$$\tilde{T}_j(x) = T_j(-2x + 1) \,, \tag{3.101}$$

where $x = e^{-\omega}$, i.e. $0 \leq x \leq 1$. A comparison between different choices of ω_0 will be postponed to the next chapter.

We approximate the smeared kernel as shown in Fig. 3.4. We compare the approximation for $l = 0, 2$ with $\sigma = 0.1, 0.01$, while keeping the order $N = 10$ of the polynomial. The second row of Fig.

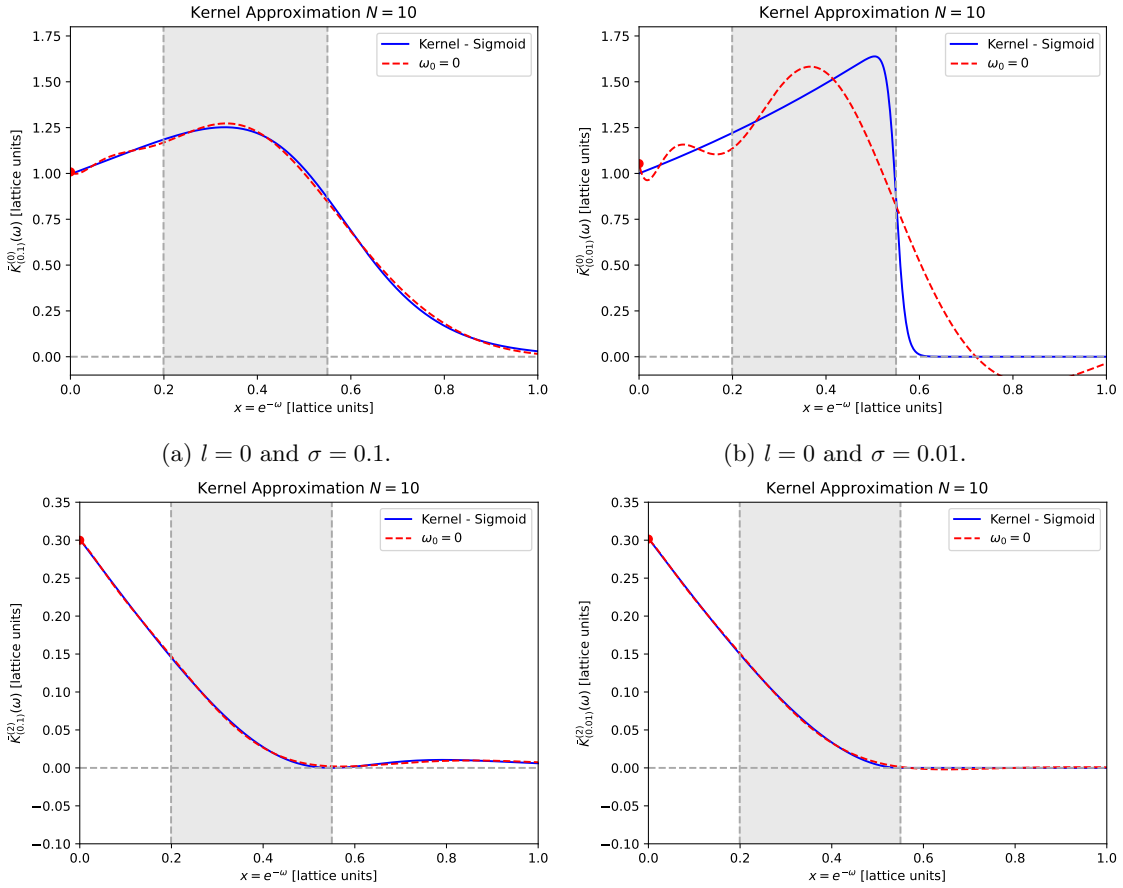

(a) $l = 0$ and $\sigma = 0.1$.

(b) $l = 0$ and $\sigma = 0.01$.

(c) $l = 2$ and $\sigma = 0.1$.

(d) $l = 2$ and $\sigma = 0.01$.

Figure 3.4: Approximation results for different choices of the smearing where the order of the polynomial approximation is kept constant at $N = 10$. The two values of the smearing are 0.1 shown on the left hand side and 0.01 shown on the right hand side. The difference between rows is the choice of l, which is $l = 0$ for the first row and $l = 2$ for the second row.

3.4, with $l = 2$, shows a mild dependence on the smearing. We thus expect that the dependence on the polynomial order N is also mild, which we confirm. In the first row, $l = 0$, a strong dependence on the smearing σ is observed. While $N = 10$ is sufficient to obtain a good approximation for $\sigma = 0.1$, it does not suffice when $\sigma = 0.01$. Depending on the kinematics determined by l, the dependence on the polynomial order of the Chebyshev approximation varies.

We now address how to estimate the corrections. Each order of the Chebyshev polynomials represents a frequency component of the function to be approximated. At the same time, we interpret the smearing as a sort of width of the kernel function. Therefore, we combine these two

representations and introduce a relation between the smearing and the polynomial order as

$$\sigma = \frac{1}{\alpha N}\,, \tag{3.102}$$

where α is a factor which we equal to one. We now have an expression combining the two limits, since the $N \to \infty$ limit now directly translates to the $\sigma \to 0$ limit. Nevertheless, we cannot reach arbitrarily small σ (or high N), since in a practical application, we reconstruct the Chebyshev matrix elements from lattice data, i.e. we are limited in our polynomial order N due to the finite time slices t as well as the statistical error of the correlator discussed for (3.95). We circumvent this problem by employing the property that the Chebyshev polynomials are bounded, i.e. $|\tilde{T}_j(x)| \leq 1$. We introduce a cut-off in the polynomial order N_{Cut} up to which we can properly reconstruct the Chebyshev matrix elements and for orders higher than the cut-off we assume a maximum error. Namely, we assume that the Chebyshev matrix elements are on the end of the bound, i.e. $\tilde{T}_j = \pm 1$ for $j > N_{\mathrm{Cut}}$. We add the absolute value of the coefficients $\tilde{c}_j$ onto an error of the approximation. We hence rewrite the approximation as

$$\bar{K}^{(l)}_{(\sigma)}(\omega) \simeq \frac{\tilde{c}_0}{2} + \sum_{j=1}^{N_{\mathrm{Cut}}} \tilde{c}_j \tilde{T}_j(e^{-\omega}) + \sum_{\substack{k= \\ N_{\mathrm{Cut}}+1}}^{N} |\tilde{c}_k|\,, \tag{3.103}$$

where the last term only contributes to the error. This error estimate depends only on the coefficients $\tilde{c}_k$. We consider the behavior of these coefficients, analytically known from (3.100). Additionally, for a fixed l, the only free parameter in the calculation of the coefficients is the smearing of the kernel function, i.e. for a fixed choice of the smearing we can calculate the coefficients up to any order. Figs. 3.5 and 3.6 show the coefficients for the same set-up as above, i.e. $l = 0, 2$ and $\sigma = 0.1, 0.01$, as a function of the polynomial order j, with j spanning from 0 to 20. Fig. 3.5 shows how the coefficients oscillate as a function of j, while Fig. 3.6 shows the absolute values of the coefficients on a logarithmic scale in order to visualize the exponential drop of their magnitude.

With the currently available lattice data, the polynomial order is limited to $N = 10$, with more details given in ch. 4. Figs. 3.5 and 3.6 then indicate that the kernel function with $l = 2$ does not receive major corrections when going to small σ (or consequently large N), since the coefficients of $j \sim 10$ have already dropped off by ~ 3 order of magnitude when compared to $j = 0$ and higher order continue to rapidly fall off. The kernel with $l = 0$ on the other hand will receive non-negligible corrections for $j > 10$. For $\sigma = 0.01$, Fig. 3.5 shows that the coefficients still oscillate for higher orders and Fig. 3.6 shows that their magnitude has decreased only by ~ 1 order of magnitude even at the highest order of $j = 20$ shown in the plot, confirming that the quality of the approximation depends on the choice l. These conclusions are found for $\boldsymbol{q}^2 = 0\,\mathrm{GeV}^2$, while lager corrections are expected for higher values of $\boldsymbol{q}^2$. For these values, the allowed phase space region becomes

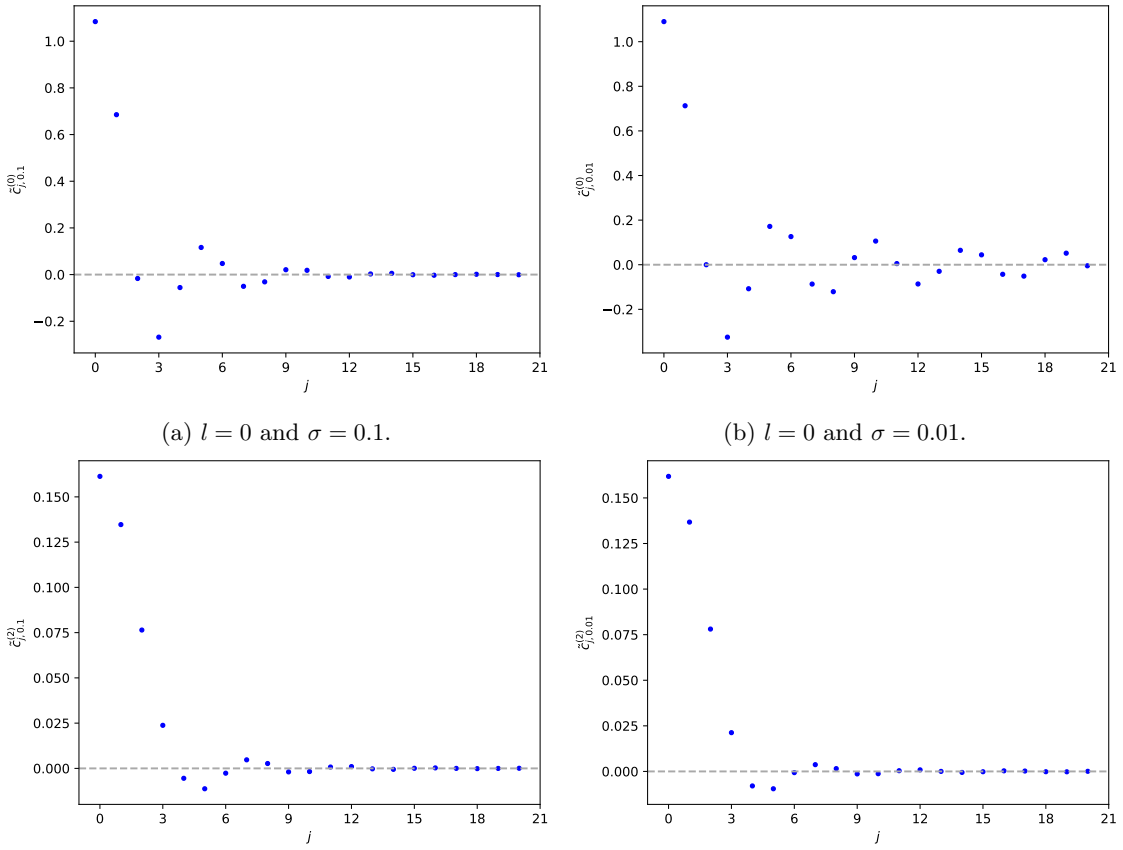

(a) $l = 0$ and $\sigma = 0.1$.

(b) $l = 0$ and $\sigma = 0.01$.

(c) $l = 2$ and $\sigma = 0.1$.

(d) $l = 2$ and $\sigma = 0.01$.

Figure 3.5: Coefficients in the Chebyshev approximation of the kernel for different choices of l and σ as a function of the polynomial order N. The different rows show the different choices of l, while the columns different values of the smearing.

narrower, meaning that smaller values of the smearing, or consequently higher polynomial order N, are required, resulting in larger corrections when taking the limits.

In summary, we introduced a method to combine the required limits to estimate the systematic error due to the approximation. We verified that the expected corrections depend on the kinematical factors in the kernel function controlled by the parameter l. In addition, we have shown indications that higher values of the momentum transfer $\boldsymbol{q}^2$ will result in larger corrections, as a consequence of the reduced phase space and will show more details in the discussion of the kernel function in ch. 4. Finally, while the method discussed above is mathematically solid, it may give a too conservative estimate and the the real error is expected to be in between the errors indicated by our analysis, which we show in ch. 4.

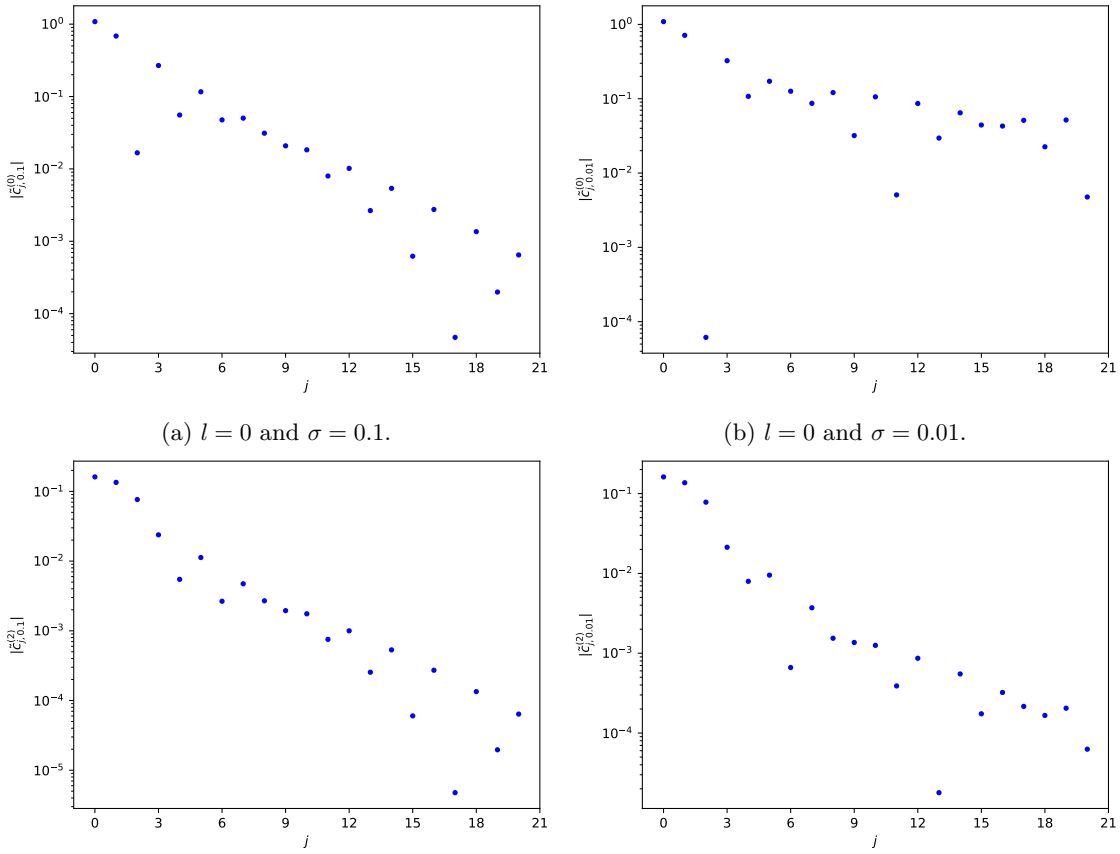

(a) $l = 0$ and $\sigma = 0.1$.

(b) $l = 0$ and $\sigma = 0.01$.

(c) $l = 2$ and $\sigma = 0.1$.

(d) $l = 2$ and $\sigma = 0.01$.

Figure 3.6: Absolute values of the coefficients in the Chebyshev approximation of the kernel on a logarithmic scale. The different rows show the different choices of l, while the columns different values of the smearing.

3.4.2 Corrections due to finite volume effects

In this section we discuss the finite-volume effects. As discussed in sec. 3.2, specifically Eq. (3.62), the reconstruction of spectral densities from correlators $C_{\mu\nu}(t)$ with a finite set of discrete time slices t poses an ill-posed inverse problem. Even if the inverse problem could be solved for a correlator in finite-volume, $C_{V,\mu\nu}(t)$ and hence the corresponding spectral density, $\rho_V(\omega)$ is obtained, it still qualitatively differs from the infinite volume counterpart $\rho(\omega)$. While the infinite volume spectral density $\rho(\omega)$ is a smooth function, $\rho_V(\omega)$ is given by a sum of δ-functions corresponding to allowed states in a finite-volume. Fig. 3.7 visualizes the situation for two-body states in a finite-volume. By introducing the smearing σ discussed in sec. 3.2 this problem can be avoided, since by increasing the

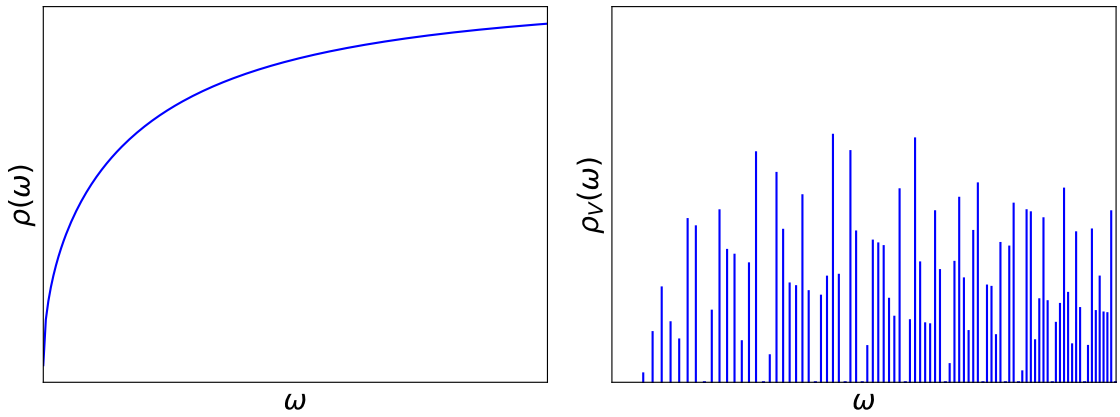

(a) $\rho(\omega)$ (b) $\rho_V(\omega)$

Figure 3.7: Sketch of the infinite-volume spectral density $\rho(\omega)$ (left) and the finite-volume $\rho_V(\omega)$ for a specific volume V (right). The height of $\rho_V(\omega)$ corresponds to the multiplicity of the states for each energy ω.

smearing width σ, the inverse problem is made arbitrarily mild and the smeared spectral density $\rho_{\sigma,V}$ approaches its infinite volume counterpart smoothly. The inclusive decay rate is then recovered by taking the ordered double limit of $V \to \infty$ and vanishing smearing width.

Since the allowed states are controlled by the boundary condition, finite volume effects for the spectral density can be sizeable for multi-hadron states. For instance, the energy spectrum of two-body states receive corrections of $\mathcal{O}(1/L^3)$. While for the smeared spectral density this would be reduced significantly, its size and scaling in the $V \to \infty$ limit may be non-trivial. We therefore introduce a model to investigate the volume dependence. In ch. 4, we verify that the model gives a good description of the finite volume data, and use it for an estimate of the finite volume effects.

Among various multi-hadron states, our model considers the two-body final states, specifically $K\bar{K}$ final states, which are expected to give the dominant contribution. The derivation of the spectral density is based on the vacuum-polarization function at one-loop level shown in Fig. 3.8. We consider the imaginary part

$$\text{Im } \mathcal{M}_{\text{Diagram}} = \pi \int \frac{d^3\boldsymbol{q}}{(2\pi)^3} \int dq_0 \delta\left((p+q)^2 - m_K^2\right) \theta(p_0+q_0) \delta(q^2 - m_K^2) \theta(-q_0)\,. \tag{3.104}$$

Assuming the rest frame in which $p = (p_0, 0, 0, 0)$, we perform the q_0 integration to arrive at

$$\rho(p_0) = \pi \int \frac{d^3\boldsymbol{q}}{(2\pi)^3} \frac{1}{(2\epsilon_{\boldsymbol{q}})^2} \delta(p_0 - 2\epsilon_{\boldsymbol{q}})\,, \tag{3.105}$$

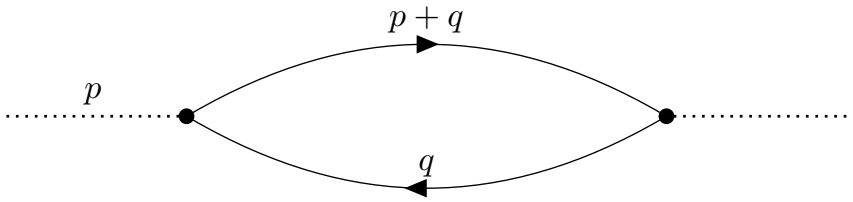

Figure 3.8: Feynman diagram representing the vacuum production of the two-body final state assumption used to derive the spectral density.

where we introduce the short-hand notation $\epsilon_{\boldsymbol{q}}^2 = \boldsymbol{q}^2 + m_K^2$. Within this free particle model, the infinite volume spatial integral in (3.105) is written as

$$\rho(\omega) = \frac{1}{2\pi}\int_0^\infty dq \frac{q^2}{4(q^2+m_K^2)}\delta(\omega - 2\sqrt{q^2+m_K^2})\,. \tag{3.106}$$

This expression corresponds to the vacuum production of a $K\bar{K}$ state through an operator $\mathcal{O}$, which is assumed as either the scalar density ($J=0$) or the vector current ($J=1$). It models the two-body decay of the D_s meson assuming that the wave function of the D_s meson only results in negligible effects, which we incorporate through the introduction of a form factor in ch. 4. Performing the final integration, we arrive at an expression for the spectral density in the infinite volume which we write as

$$\rho(\omega) = \frac{1}{16\pi}\sqrt{1-\frac{4m_K^2}{\omega^2}}\,, \tag{3.107}$$

reproducing the well-known formula that has been derived, e.g. in [108]. The finite volume representation of the spectral density from (3.105) is straightforward by replacing the integral with a sum $1/V\sum_{\boldsymbol{q}}$, i.e.

$$\rho_V(\omega) = \frac{\pi}{V}\sum_{\boldsymbol{q}} \frac{1}{4(\boldsymbol{q}^2+m_K^2)}\delta\left(\omega - 2\sqrt{\boldsymbol{q}^2+m_K^2}\right)\,. \tag{3.108}$$

The possible values of $\boldsymbol{q}^2$ for a fixed volume V are given by $\boldsymbol{q} = 2\pi/L\boldsymbol{l}$, where L is the spatial extent of the lattice and $\boldsymbol{l} = (l_1, l_2, l_3)$ is a vector where l_i can take any integer in $L/2 < l_i \leq L/2$. The spectral density shown above corresponds to the scalar case ($J=0$). We follow a similar calculation for the vector current ($J=1$) where additional details on the calculation can be found in [108] and arrive at the following expressions for the spectrum in the infinite volume

$$\rho(\omega) = \frac{1}{64\pi}\omega^2\left(1-\frac{4m_K^2}{\omega^2}\right)^{3/2}\,, \tag{3.109}$$

whereas the finite volume expression is given by

$$\rho_V(\omega) = \frac{\pi}{V}\sum_{\boldsymbol{q}} \frac{\boldsymbol{q}^2}{4(\boldsymbol{q}^2+m_K^2)}\delta\left(\omega - 2\sqrt{\boldsymbol{q}^2+m_K^2}\right) . \tag{3.110}$$

In the following, we consider the reconstruction of the infinite volume limit for

$$\bar{X}^{(l)}(\omega_{\mathrm{th}}) = \int_0^{\omega_{\mathrm{th}}} d\omega \rho_{(V)}(\omega) \times K^{(l)}(\omega) , \tag{3.111}$$

which corresponds to the definition of the $\bar{X}^{(l)}$ given in (3.25) - (3.27) as a convolution between the kernel function and the spectral density. In the integral above we have introduced a dependence of $\bar{X}^{(l)}$ on a variable ω_{th}. Let us take a look at the kernel defined in (3.98)

$$\bar{K}^{(l)}_{(\sigma)}(\omega) = e^{2\omega t_0}(m_{D_s}-\omega)^l \theta_{(\sigma)}(m_{D_s}-\sqrt{\boldsymbol{q}^2}-\omega) . \tag{3.112}$$

Here, the upper limit of integration is fixed through the term $\theta(m_{D_s}-\sqrt{\boldsymbol{q}^2}-\omega)$ for the physical semileptonic decay process. But, in theory we are free to choose a general threshold away from the physical one. We employ this freedom in order to study to which degree our model is able to describe the lattice data. We define this general threshold as ω_{th} and the physical threshold as $\omega_{\mathrm{th}}^{\mathrm{Phys}} = m_{D_s} - \sqrt{\boldsymbol{q}^2}$, and modify the kernel function

$$\bar{K}^{(l)}_{(\sigma)}(\omega,\omega_{\mathrm{th}}) = e^{2\omega t_0}\left(m_{D_s} - \frac{\omega_{\mathrm{th}}^{\mathrm{Phys}}}{\omega_{\mathrm{th}}}\omega\right)^l \theta_{(\sigma)}(\omega_{\mathrm{th}}-\omega) . \tag{3.113}$$

The term $\omega_{\mathrm{th}}^{\mathrm{Phys}}/\omega_{\mathrm{th}}$ is introduced to ensure the kernel is always positive. In Fig. 3.9 we show $\bar{X}^{(l)}(\omega_{\mathrm{th}})$ for two choices of the finite volume $V = 48^3$ and 256^3, in addition to the infinite volume limit. We show the scalar case ($J = 0$) in the first row and the vector case ($J = 1$) in the second row. We show both choices of $l = 0$ (left) and $l = 2$ (right). We observe that the scaling on the volume depends on the contribution of l in the kernel function. The kernel with $l = 0$ shows a strong volume dependence as a function of ω_{th}. Due to the sharp drop in the kernel function, the discrete nature of the spectral density for the volume of $V = 48^3$ results in a step function-like behavior. By increasing the volume, the step sizes become smaller and we obtain a near reproduction of the infinite volume limit for $V = 256^3$. In the case of $l = 2$, the kernel function smoothly approaches zero when approaching the threshold value resulting in a mild volume dependence and a good reproduction already at $V = 48^3$.

Next, we address how the model can be combined with the lattice data, since the pre-factors appearing in the finite volume spectral densities defined in (3.108) and (3.110) do not correspond to actual physical values. We rewrite our finite volume notation to fit our upcoming purposes. We

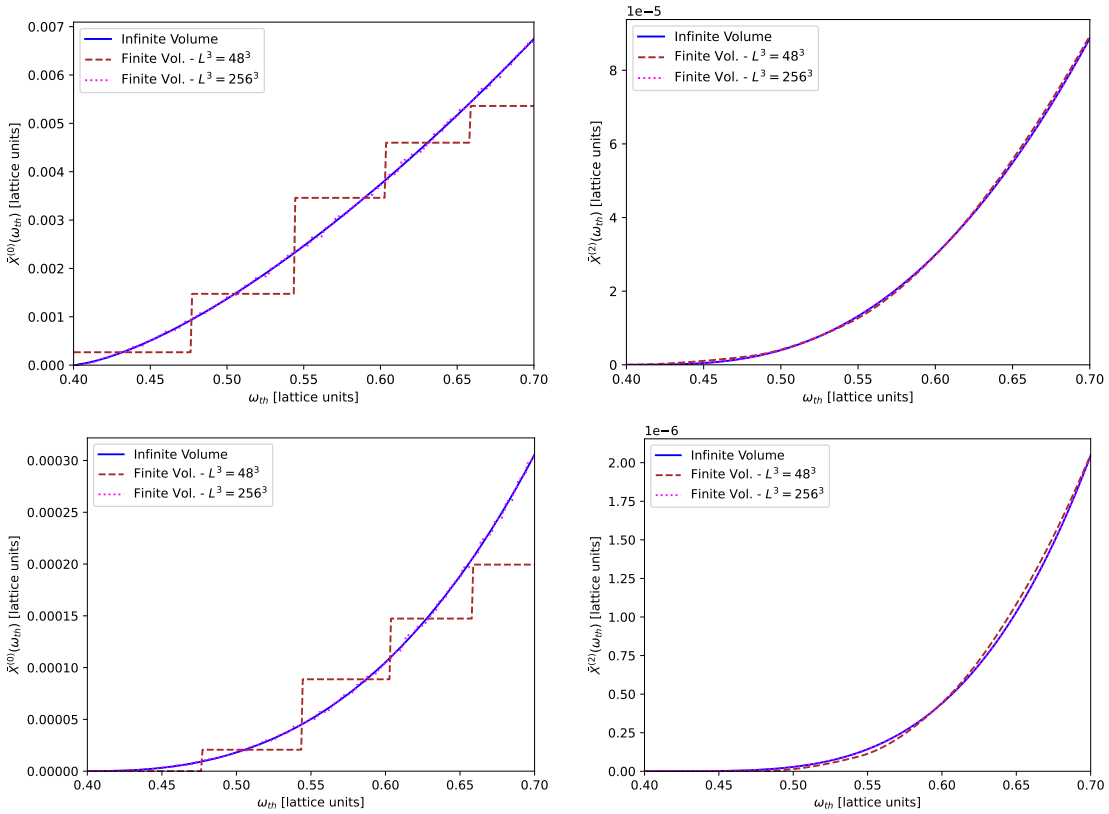

Figure 3.9: Infinite volume limit (solid line) using the finite volume expressions for the spectral densities defined for $J = 0$ (first row) and $J = 1$ (second row) as a function of the threshold energy $\omega_{\rm th}$. We show $l = 0$ (first column) and $l = 2$ (second row). The choices of the finite volume correspond to $V = 48^3$ (dashed line) and $V = 256^3$ (dash-dotted line) lattices.

present the arguments and calculations only for the vector case of the spectral density, and only show the final result for the scalar case, which follows the same logic. Let us first rewrite the finite volume version of the spectral density as

$$\rho(\omega) = \frac{\pi}{V} \sum_{n=0}^{(L/2)^2} \left(\frac{2\pi}{L}\right)^2 \frac{n\eta_n}{4\left[\left(\frac{2\pi}{L}\right)^2 n + m_K^2\right]} \delta\left(\omega - 2\sqrt{\left(\frac{2\pi}{L}\right)^2 n + m_K^2}\right) , \tag{3.114}$$

where we change the index of the sum to run over all possible values of $\boldsymbol{q}^2$. We use the finite volume definition of $\boldsymbol{q}^2 = (2\pi/L)^2 \boldsymbol{l}^2$, where $\boldsymbol{l} = (l_1, l_2, l_3)$ and $-L/2 < l_i \leq L/2$. We also define $n = l_1^2 + l_2^2 + l_3^2$, as there are several configurations of $\boldsymbol{l}$ that give the same n, e.g. $n = 1$ is fulfilled by $(1, 0, 0)$, $(0, 0, 1)$, $(0, -1, 0)$ and so on. All of these configurations are equivalent and the total

number of these configurations is collected in the multiplicity factor η_n. The first several values for η_n are given by

$$\eta_n = \{1, 6, 12, 8, 6, 24, \cdots\} \ , \quad n = \{0, 1, 2, 3, 4, 5, \cdots\} \ . \tag{3.115}$$

Since it is not possible to determine the contribution of each state by itself we implement a reference state, i.e. we normalize the pre-factors to the lowest energy state, i.e. $n = 1$. We rewrite the spectral density as

$$\begin{aligned}
\rho(\omega) &= \frac{\pi}{V}\left(\frac{2\pi}{L}\right)^2 \frac{\eta_1}{4\left[\left(\frac{2\pi}{L}\right)^2 + m_K^2\right]} \left[\delta\left(\omega - 2\sqrt{\left(\frac{2\pi}{L}\right)^2 + m_K^2}\right)\right. \\
&\quad \left. + \sum_{n=2}^{(L/2)^2} \frac{4\left[\left(\frac{2\pi}{L}\right)^2 + m_K^2\right]}{\eta_1} \frac{n\eta_n}{4\left[n\left(\frac{2\pi}{L}\right)^2 + m_K^2\right]} \delta\left(\omega - 2\sqrt{n\left(\frac{2\pi}{L}\right)^2 + m_K^2}\right)\right] \\
&= s(V)\left[\delta\left(\omega - 2\sqrt{\left(\frac{2\pi}{L}\right)^2 + m_K^2}\right)\right. \\
&\quad \left. + \sum_{n=2}^{(L/2)^2} \frac{4\left[\left(\frac{2\pi}{L}\right)^2 + m_K^2\right]}{\eta_1} \frac{n\eta_n}{4\left[n\left(\frac{2\pi}{L}\right)^2 + m_K^2\right]} \delta\left(\omega - 2\sqrt{n\left(\frac{2\pi}{L}\right)^2 + m_K^2}\right)\right] ,
\end{aligned} \tag{3.116}$$

where we introduce the short-hand notation $s(V)$ in the second line which controls the total contributions. The term in the square-brackets now contains the relative magnitude among excited states with $n \geq 2$. The volume dependence of $s(V)$ for any volume V' is given by

$$\begin{aligned}
\frac{s(V')}{s(V)} &= \frac{V}{V'}\left(\frac{L}{L'}\right)^2 \frac{\left(\frac{2\pi}{L}\right)^2 + m_K^2}{\left(\frac{2\pi}{L'}\right)^2 + m_K^2} \\
&= \left(\frac{L}{L'}\right)^5 \frac{\left(\frac{2\pi}{L}\right)^2 + m_K^2}{\left(\frac{2\pi}{L'}\right)^2 + m_K^2} ,
\end{aligned} \tag{3.117}$$

where in the second line we have only used $V = L^3$ and $s(V)$ is considered a reference value that needs to be extracted from a fit to lattice data. In ch. 4, we discuss a fitting procedure used to extract $s(V)$. For the scalar case, the aforementioned expression (3.117) reads

$$\frac{s(V')}{s(V)} = \left(\frac{L}{L'}\right)^5 . \tag{3.118}$$

We postpone additional details on the construction of the fit and the resulting infinite volume extrapolation to ch. 4.

In the next chapter we discuss the analysis using the ideas and techniques developed in this chapter.

Chapter 4

Numerical Analysis of Inclusive Decays on the Lattice

We apply the techniques discussed in the last chapter to analyze the data obtained from lattice simulations.

This chapter is structured as follows. In section 4.1 we discuss the lattice setup used to generate the data used in the analysis. Following this we verify the simulation results by checking the two- and four-point correlators and discuss our choices for the parameters used in the four-point functions in sec. 4.2. In sec. 4.3 we discuss the approximation of the kernel function using the Chebyshev approximation, although at this stage the discussion will not include any connection to the data. Sec. 4.3.1 then discusses how the data is used in practice to determine the Chebyshev matrix elements needed in the analysis and further discusses the limitations in what can be achieved with the current data set. Following this, in sec. 4.4 we discuss and present the main results, i.e. we determine $\bar{X}(\boldsymbol{q}^2)$ from the lattice data and calculate $\Gamma/|V_{cs}|^2$ to determine the CKM matrix element which is then compared to experimental results from the BESIII collaboration [109] for the inclusive semielectronic decay of the D_s meson. Finally, in secs. 4.4.4 and 4.4.5 we discuss our methods on how we estimate the systematic errors from the approximation and finite volume effects, respectively, as well as show applications for a set of examples.

4.1 Numerical Setup

Our study employs gauge ensembles generated by the JLQCD collaboration including $2+1$ flavors of dynamical quarks in lattice QCD. Our simulations are performed on a $48^3 \times 96$ lattice, corresponding to a lattice spacing of $a \simeq 0.055\,\mathrm{fm}$ or a lattice cut-off of $a^{-1} \sim 3.610(9)\,\mathrm{GeV}$. These parameters

are determined by employing the Yang-Mills gradient flow [110]. To achieve better control over the discretization errors we employ the tree-level Symanzik improved gauge action and we also apply stout smearing [111] to the gauge field when coupled to fermions. We further use the Möbius domain-wall action [76, 83] for both heavy and light quarks. For additional information on the practical implementation and formulation of the quark action in five dimensions we refer to [83, 90, 112]. The choice of light quark masses used in this work corresponds to a pion mass of $M_\pi \simeq 300\,\mathrm{MeV}$. Our ensemble further satisfies the condition $M_\pi L > 4$, where L is the spatial extent of the lattice. This condition is generally required to reach a sufficient suppression of finite volume effects to a regime below the percent level for, e.g. meson masses and form factors. Due to the introduction of the finite fifth dimension L_5, Möbius domain-wall fermions have no exact chiral symmetry. A measure for the violation of chiral symmetry is the residual quark mass, which for the lattice employed in this work is below the level of 0.2 MeV and hence significantly smaller than the physical masses of the up and down quarks. For our simulations, we average over 50 statistically independent gauge configurations. Furthermore, we perform our measurements for each configuration on 8 evenly distributed choices of the time source. We induce four different momenta in the four point function defined in (3.56). Following the definition $\boldsymbol{q} = 2\pi/L\boldsymbol{l}$, we choose $\boldsymbol{l} = (0,0,0),(0,0,1),(0,1,1),(1,1,1)$. All correlation functions analyzed in this work have been simulated using the Grid [113–115] and Hadrons [116] software packages. For most of the fits shown in this section we have employed lsqfit [117, 118].

4.2 Behavior of two- and four-point correlation functions

In this section we consider the basic outline on how the ratio of the two- and four-point correlation functions defined in (3.60) is constructed. We discuss how the necessary parameters are extracted from two-point correlation functions of the D_s meson. Following this, we discuss how the four-point correlation functions are constructed based on (3.60).

4.2.1 Two-point correlation function

The two-point correlation functions of the D_s meson depicted in Fig. 4.1 is needed for the denominator of (3.60) in the analysis of the four-point correlation functions. We consider all cases of different

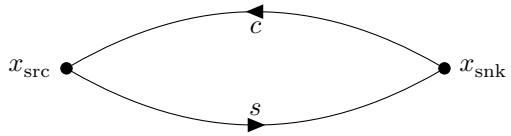

Figure 4.1: Schematic representation of the valence quarks in the two point correlation function for the meson interpolators (4.1).

combinations of the smearing for the zero momentum correlator $C^{LL}_{D_s}(t, t_{\text{src}})$, $C^{LS}_{D_s}(t, t_{\text{src}})$, $C^{SL}_{D_s}(t, t_{\text{src}})$ and $C^{SS}_{D_s}(t, t_{\text{src}})$, where the superscripts L and S specify local or smeared operators defined through

$$\mathcal{O}^X_{D_s}(x_{\text{src}}) = \bar{c}^X(x_{\text{src}})\Gamma_{\text{src}}s^X(x_{\text{src}})\,, \quad \mathcal{O}^X_{D_s}(x_{\text{snk}}) = \bar{c}^X(x_{\text{snk}})\Gamma_{\text{snk}}s^X(x_{\text{snk}})\,, \tag{4.1}$$

where $X = L, S$ and $\Gamma_{\text{src}} = \Gamma_{\text{snk}} = \gamma_5$. The fit function for the two-point correlator can be written as

$$C_P(t) = \sum_n a_{n,P}b^*_{n,P}\left(e^{-E_{n,P}t} + e^{-E_{n,p}(T-t)}\right) \tag{4.2}$$

where the subscript P, n corresponds to the n-th state of pseudoscalar P, so that $n = 0$ corresponds to the ground state and T is the extent of the lattice in temporal direction. In case where the interpolating operators at source and sink are both smeared or local, the amplitudes $a_{n,P}$ and $b^*_{n,P}$ are identical, or different otherwise. To extract the amplitude $\langle 0|\mathcal{O}^S_{D_s}|D_s\rangle$ appearing in the denominator of (3.60) we perform a combined fit of all correlators except for the local-local operator combination. We do so in order to increase the accuracy with which we can determine the ground state energy. Since we are only interested in the ground state energy we only fit to a single exponential in the fit prescription shown above. We fit in the range $t \in [20, 28]$ and arrive at the following results for our fit

$$\begin{aligned} &a^L_{D_s} = 6.648(21) \times 10^{-2}\,, \quad b^S_{D_s} = 1.1975(31) \times 10^{-5}\,, \\ &E_{D_s} = 0.549\,86(27)\,, \quad \chi^2/\text{dof} = 1.2 \end{aligned} \tag{4.3}$$

given in lattice units. This corresponds to a D_s mass of

$$M_{D_s} = 1.9845(1)\,\text{GeV}\,, \tag{4.4}$$

which is in reasonable agreement with the value given in the PDG $M^{\text{PDG}}_{D_s} = 1968.35(7)\,\text{MeV}$. To verify that our fit produces results which is consistent with the expected D_s meson mass for our lattice configuration, we look at the effective mass plot of the two-point correlation function, which is defined by the following relation

$$\frac{C(t)}{C(t+1)} = \frac{\cosh\left(m_{\text{eff}}\left(t - \frac{T}{2}\right)\right)}{\cosh\left(m_{\text{eff}}\left(t+1 - \frac{T}{2}\right)\right)}\,, \tag{4.5}$$

and has to be solved for m_{eff} at each value of t. A plateau in the effective mass plot corresponds to a dominance of the ground state energy, i.e. $m_{\text{eff}} = E_{D_s}$. In Fig. 4.2 we show the effective mass determined from the correlator for the combinations of interpolating operators used in the fit, i.e. SL, LS and SS as well as the effective mass calculated from our fit results. We observe a good

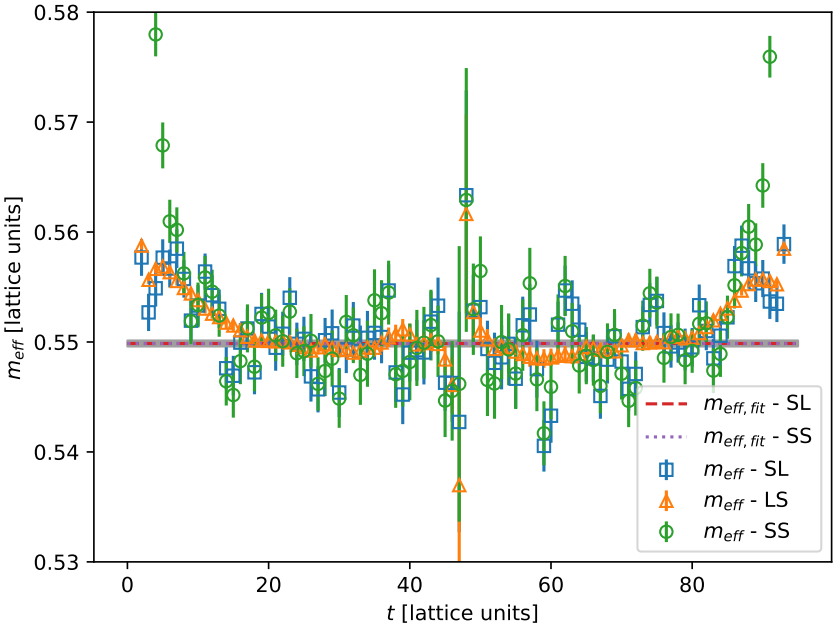

Figure 4.2: Effective mass calculated for two-point correlation functions for different combinations of interpolating operators. We show the effective mass determined for all combinations used in our fit: SL (blue), LS (orange) and SS (green). We also show the effective mass calculated from our fit results and they are represented by the dashed and dotted lines, depending on whether the SL or LS case is considered.

agreement between our fit results and the behavior indicated by the correlator, so that we adapt the value for the denumerator in (3.60) using $b^S_{D_s}$.

4.2.2 Four-point correlation function

We now turn towards the four-point correlation function defined in (3.60), which constitutes the main tool in the treatment of inclusive processes. In our simulation we use a source-sink separation of $T = t_{\text{snk}} - t_{\text{src}} = 42$ given in lattice units. In the construction of the lattice data we have the freedom to either keep t_1 or t_2 constant and vary its corresponding counterpart (see Fig. 3.2). We simulate both cases and average over them. The choices of t_1 and t_2 have to be made in such a way that a sufficient ground state saturation has been achieved in the two-point correlation function. For one case, we keep the current $J^\dagger_\mu$ fixed at time slice $t_2 = t_{\text{src}} + 26$, so that the time dependence is defined in the range $0 \leq t \leq 26$, where $t = t_2 - t_1$. This choice of time separation requires a sufficient ground state saturation at $t' = t_{\text{snk}} - t_2 = 16$ which can be confirmed by comparison with the effective mass plot shown in Fig. 4.2. In case where we keep the current J_ν at time slice

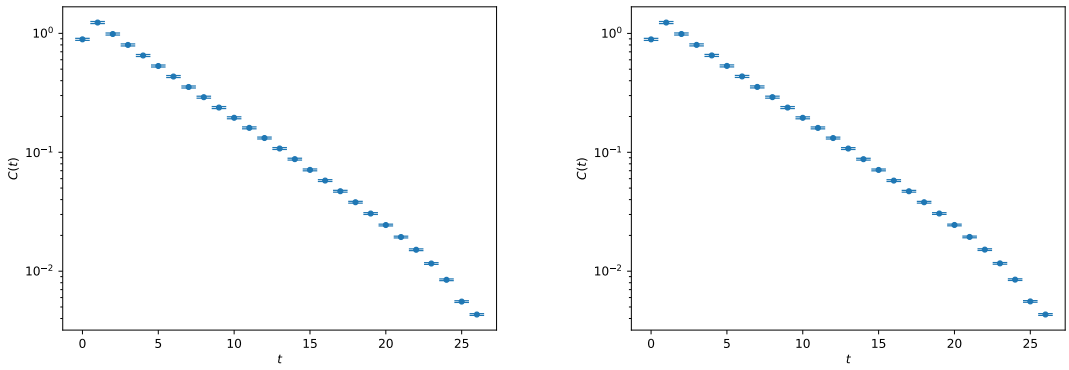

(a) t_2 fixed (b) t_1 fixed

Figure 4.3: Comparison of the correlator ratio defined in (3.60), where we keep either t_2 (left) or t_1 (right) fixed. Both of them show the same behavior. The final correlator used is the average over both of these results.

$t_1 = t_{\text{src}} + 16$ fixed, we find the same time dependence $0 \leq t \leq 26$, where this time $t = t_{\text{snk}} - t_1 - t_2$. The same argument for ground state saturation in the the two-point correlation function holds where this time $t' = t_1 - t_{\text{src}} = 16$. We show the correlators evaluated for both choices of the fixed currents in Fig. 4.3 for the specific choice where both currents correspond to the temporal component of the vector current. Since the currents at hand in this work possess a $(V-A)$ structure, we consider all possible combinations of $J_\nu(x_1)$ and $J^\dagger_\mu(x_2)$, namely $V^\dagger_\mu V_\nu$, $V^\dagger_\mu A_\nu$, $A^\dagger_\mu V_\nu$ and $A^\dagger_\mu A_\nu$. But, since we are working in the limit of massless leptons, i.e. $m_\ell = 0$, current combinations of the type $V^\dagger_\mu A_\nu$ and $A^\dagger_\mu V_\nu$ do not contribute to the total decay rate. Considering (3.6), we see that this type of current combinations are related to the structure function W_3 through the relation $W^{AV}_{ij} + W^{VA}_{ij} = i\epsilon_{ij0k} q^k W_3$ which, in the case of massless leptons, do not contribute due to parity. In our simulations, the induced momentum $\boldsymbol{q}$ is carried by the s quark shown in Fig. 3.2.

4.3 Polynomial approximation of the kernel function

This section discusses details on the polynomial approximation of the kernel function. As mentioned in the previous chapter, in this work we focus solely on the approximation through the Chebyshev polynomials. We refer to [99] for details on the Backus-Gilbert approach and [100, 101] for its practical application. We analyze the difference in the approximation of the kernel function depending on the choice of the lower limit ω_0. The additional parameter t_0 which appears in the exponential $\exp(2\omega t_0)$, is chosen to be $t_0 = 1/2$ to minimize the exponential growth of the kernel function and to maximize the number of available data points in the analysis. In Fig. 4.4 we show the approximation

of the kernel function $K^{(l)}_{\mu\nu,\sigma}$ for $l = 0, 1, 2$. We compare two choices of $\boldsymbol{q}^2$, $\boldsymbol{q}^2 = 0.22\,\mathrm{GeV}^2$ and $\boldsymbol{q}^2 = 0.67\,\mathrm{GeV}^2$, representing the momentum choices of $\boldsymbol{q} = (0, 0, 1)$ and $\boldsymbol{q} = (1, 1, 1)$ used in our simulations. The smearing of the kernel function is $\sigma = 0.02$. The polynomial order used in the approximation is given by $N = 10$ which coincides with the maximal number of data points available in our analysis. For our lattice the number of available time slices is $2t_0 \leq t < t_2 - t_{\mathrm{src}}$, which translates to $1 \leq t < 26$. We further have to satisfy the condition $t \ll t_2 - t_{\mathrm{src}}$ or equivalently $t_1 - t_{\mathrm{src}} \gg 0$. By setting $N = 10$ this then corresponds to $t_1 - t_{\mathrm{src}} = 16$, which reasonably satisfies the aforementioned constraint. An improvement in the available data sets would enable larger choices for the polynomial order N and hence reduce the differences between the approximation and kernel function. The kernel functions shown in Fig. 4.4 reaffirm our conclusions in the previous chapter concerning the challenges in estimating the systematic error originating from the approximation, i.e. the kernel with $l = 0$ requires the most attention, since it possesses the sharpest drop to zero around the threshold. Shifting our focus to the quality of the approximation, depending on the choice of ω_0, we find that shifting the starting point of the approximation as close as possible to ω_{min} yields the best results. This is seen by the agreement between the interpolating function and the target function in the region of the allowed phase space (highlighted by the gray-shaded area) being better compared to the case of the approximation starting from zero. This becomes more evident in cases where ω_{min} is moved farther away from zero, i.e. for higher values of $\boldsymbol{q}^2$. This region will hence result in larger deviations for the values of $\bar{X}^{(l)}(\boldsymbol{q}^2)$ depending on the choice of ω_0. The choice of $\omega_0 = 0.9\omega_{\mathrm{min}}$, i.e. a value slightly below ω_{min}, is to avoid potential statistical fluctuations of the η meson mass.

We now have an understanding to what extent we can approximate the kernel function using the Chebyshev polynomials, although the discussion conducted in this section focuses only on the strategy with no inclusion of the lattice data. As mentioned in sec. 3.3, once we include lattice data we see a violation of the bounds of the Chebyshev polynomials $|\tilde{T}_k(x)| \leq 1$. The following section focuses on the strategy on how the Chebyshev matrix elements can be determined from lattice data.

4.3.1 Practical application of the Chebyshev polynomial approximation

We now discuss the idea behind the data analysis strategy introduced in sec. 3.3 for the case of the Chebyshev polynomial approach. We employ a fitting strategy that trades the correlator data with the fitted Chebyshev matrix elements

$$\bar{C}_{\mu\nu}(t) = \sum_{j=0}^{t} \tilde{a}_j^{(t)} \left\langle \tilde{T}_j \right\rangle_{\mu\nu} , \tag{4.6}$$

where the coefficients $\tilde{a}_j^{(t)}$ can be determined through the power representation of the Chebyshev polynomials. We refer to app. A for more details. We follow the same logic as in (3.95) and write

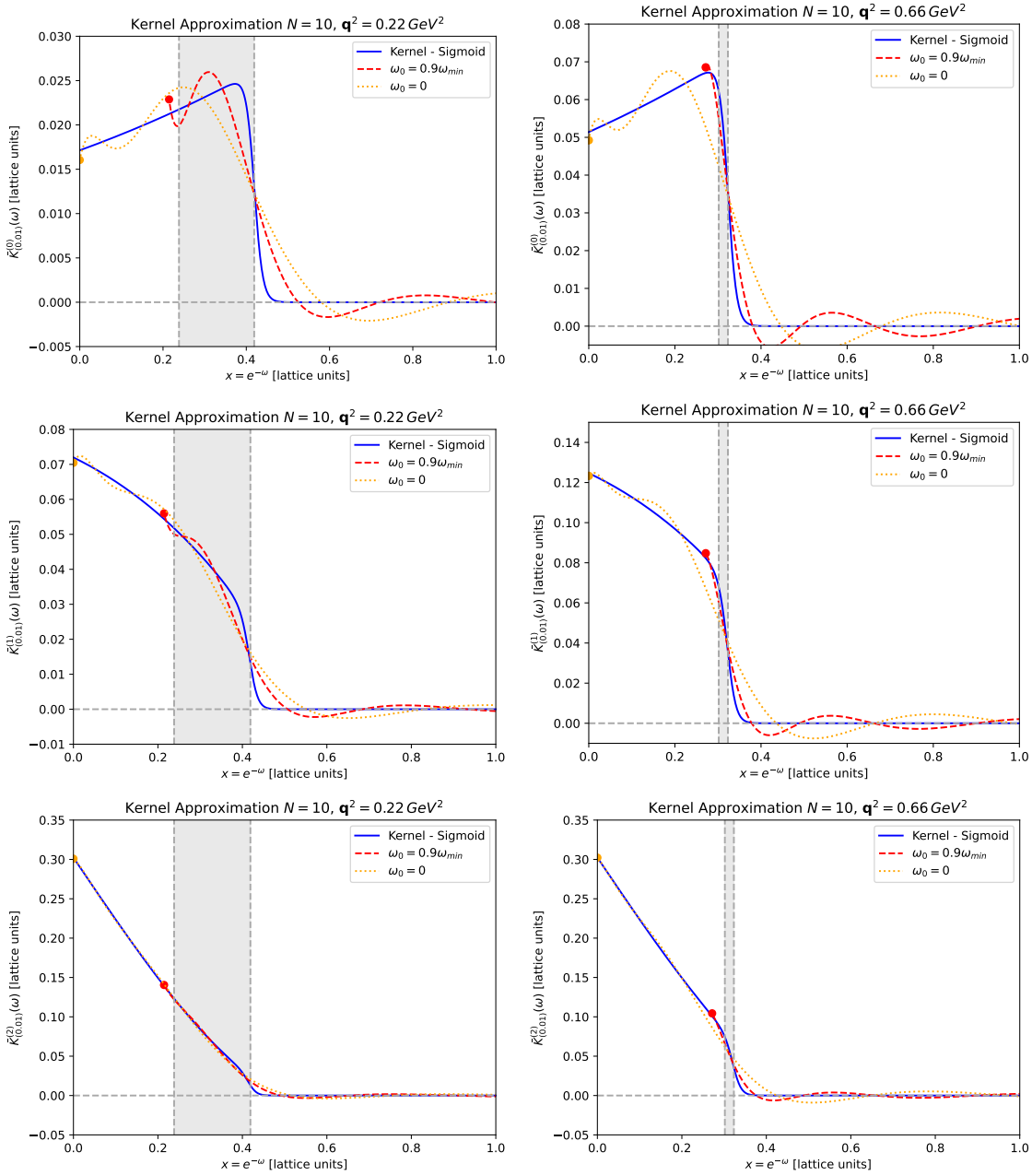

Figure 4.4: Polynomial approximation of the kernel $K^{(l)}_{\mu\nu,\sigma}$ for all values of $l = 0$ (first row), $l = 1$ (second row), $l = 2$ (third row). The column on the left corresponds to the case of $\boldsymbol{q}^2 = 0.22\,\mathrm{GeV}^2$, while the right colums shows the momentum choice of $\boldsymbol{q}^2 = 0.67\,\mathrm{GeV}^2$. We further show the kinematically allowed region $\omega_{\min} \leq \omega \leq \omega_{\max}$ for each $\boldsymbol{q}^2$ represented by the gray shaded area. The solid line represents the target function of the Chebyshev approximation, i.e. the kernel function, while the dashed and dash-dotted line represent the approximation depending on the starting point $\omega_0 = 0$ and $\omega_0 = 0.9\omega_{\min}$, respectively.

the kernel in terms of the fitted Chebyshev matrix elements

$$\langle K_\sigma^{(l)} \rangle = \frac{\tilde{c}_{\mu\nu,0}^{(l)}}{2} \langle \tilde{T}_0 \rangle_{\mu\nu} + \sum_{k=1}^{N} \tilde{c}_{\mu\nu,k}^{(l)} \langle \tilde{T}_k \rangle_{\mu\nu} = \sum_{k=0}^{N} \bar{c}_{\mu\nu,k}^{(l)} \bar{C}_{\mu\nu}(k) \,. \tag{4.7}$$

We show examples for the cases of the V_iV_i and V_iV_j channels with $i \neq j$ in Fig. 4.5, while Fig. 4.6 shows the case for the A_iA_i and A_iA_j channels. In both cases we show the extracted Chebyshev matrix elements for two choices of the inserted momentum $\boldsymbol{q}^2$, $\boldsymbol{q}^2 = 0\,\mathrm{GeV}^2$ and $\boldsymbol{q}^2 = 0.67\,\mathrm{GeV}^2$.

We compare the results for two choices of the starting value ω_0 of the Chebyshev approximation. We find that the V_iV_j and A_iA_j channels are a lot noisier, meaning that the order at which the Chebyshev matrix elements can be extracted meaningfully is a lot lower. Further, we conclude that by setting $\omega_0 = 0.9\omega_{\min}$ more Chebyshev matrix elements can be extracted in a meaningful way compared to $\omega_0 = 0$. A possible explanation is given by the relation (A.46)

$$\tilde{a}_j^{(k)}|_{\omega_0=0} = e^{-0.9\omega_{\min}} \tilde{a}_j^{(k)}|_{\omega_0=0.9\omega_{\min}} \,.$$

The additional exponential factor on the r.h.s. results in a cancellation of the exponential decay of the ground-state contributing in (4.6). This means that we have less structure to describe and hence higher order terms become less relevant. Nonetheless, both choices of the starting point result in acceptable χ^2 and the reconstructed data following (4.6) gives comparable results. We can now reconstruct the Chebyshev matrix elements from a fit to the data to create the approximation of the kernel function. In sec. 4.4.4, we address the task on how the systematic error due to the limitation in the polynomial order N of the Chebyshev approximation, as a result of the limited number of time slices available from the correlators, can be estimated.

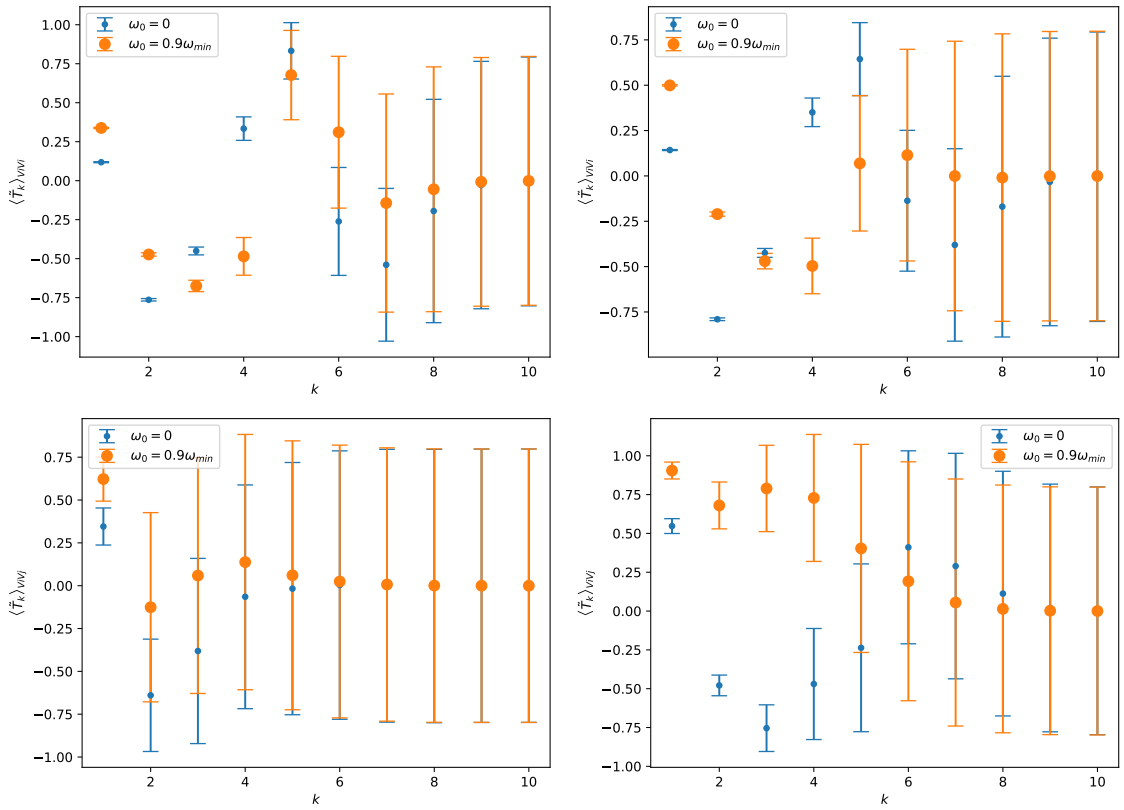

Figure 4.5: Extracted Chebyshev matrix elements for $\langle \tilde{T}_k \rangle_{V_i V_i}$ (first row) and $\langle \tilde{T}_k \rangle_{V_i V_j}$ (second row) for $i \neq j$ and $k = 1, 2, \cdots, N$ with $N = 10$. Since $\langle \tilde{T}_0 \rangle = 1$ per definition, it is not included for any of the cases shown above. We compare two cases of $\boldsymbol{q}^2 = 0\,\mathrm{GeV}^2$ (left column) and $\boldsymbol{q}^2 = 0.67\,\mathrm{GeV}^2$ (right column). We show a comparison between two choices of the starting point of the approximation $\omega_0 = 0$ (blue dots) and $\omega_0 = 0.9\omega_{\mathrm{min}}$ (orange dots).

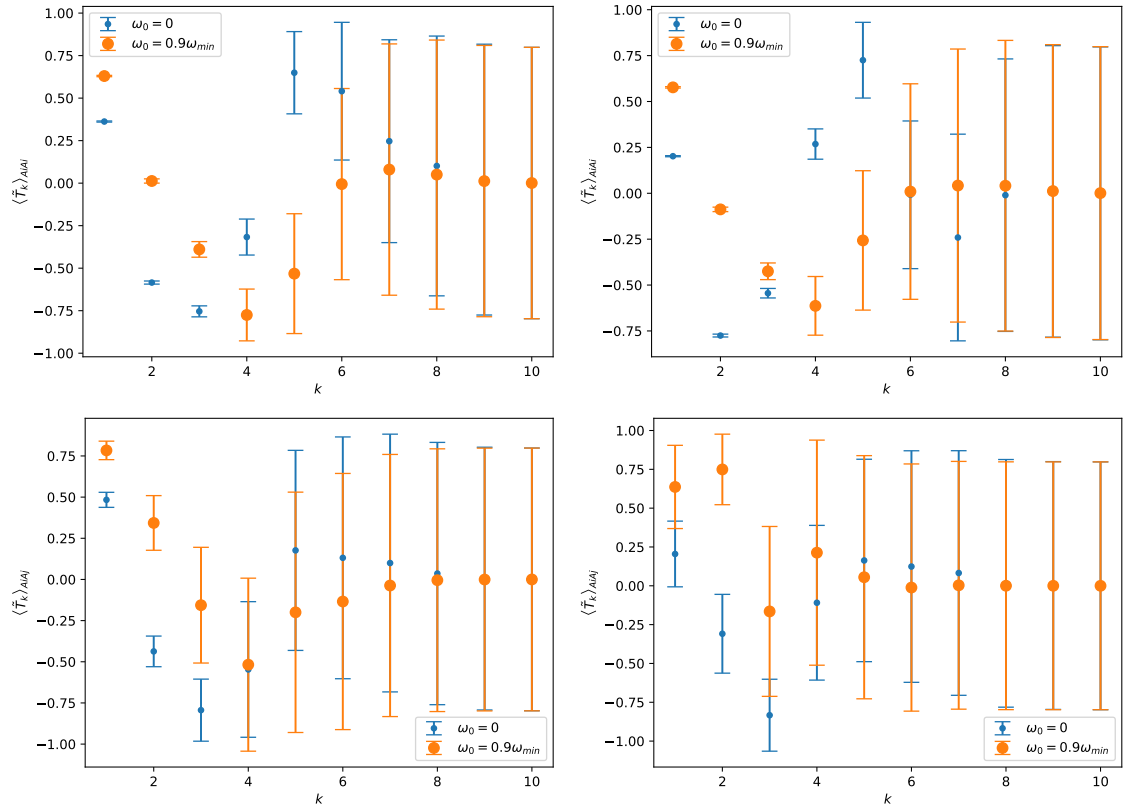

Figure 4.6: Same as Fig. 4.5, but for $\langle \tilde{T}_k \rangle_{A_i A_i}$ (first row) and $\langle \tilde{T}_k \rangle_{A_i A_j}$ (second row).

4.4 Results

In this section we combine everything discussed in the previous sections to present the main results of this work. We discuss all the necessary contributions to determine $\bar{X}(\boldsymbol{q}^2)$ for all simulated values of $\boldsymbol{q}^2$, before performing an interpolation of these results and perform the final integration over $\boldsymbol{q}^2$ to arrive at the final prediction for the total decay rate of the inclusive semileptonic decay of the D_s meson. We also discuss the methodology on how the systematic errors due to the finite order N in the Chebyshev polynomials and the smearing of the kernel function can be estimated. We further discuss the systematic error due to finite volume effects.

4.4.1 Determination of the inclusive decay rate

As defined in (3.31), we decompose $\bar{X}(\boldsymbol{q}^2)$ into components to expose the $V-A$ structure of the charged currents. As we have discussed previously, in the case of massless leptons the channels $A_\mu^\dagger V_\nu$ and $V_\mu^\dagger A_\nu$ do not contribute, leaving us with the combinations of the type $V_\mu^\dagger V_\nu$ and $A_\mu^\dagger A_\nu$. We have further discussed the decomposition into longitudinal and transversal components in sec. 3.1.1, to compare them to the ground state limit. In this way, we determine the contributions $\bar{X}^{\mathcal{P}}_{\mathcal{J}\mathcal{J}}(\boldsymbol{q}^2)$, with $\mathcal{J}$ either V or A and $\mathcal{P}$ either $\parallel$ or $\perp$ for each value of $\boldsymbol{q}^2$.

The results are shown in Fig. 4.7, where we compare the results for the two choices of the starting point of the approximation $\omega_0 = 0$ and $\omega_0 = 0.9\omega_{\text{min}}$. We find a good agreement between each set of points between the two choices of ω_0, although we observe slight deviations as the values of $\boldsymbol{q}^2$ increase. This is a result of the polynomial approximation of the kernel function discussed in the previous section and can be understood as follows: the increase of $\boldsymbol{q}^2$ results in a smaller phase space in ω and the quality of the approximation depending on the choice of ω_0 starts increasing. As indicated in Fig. 4.4 our data shows that the approximation favors $\omega \to \omega_{\text{min}}$. For the approximation using different ω_0 to become comparable, we require higher orders in the polynomial approximation for the lower choice of ω_0. Another possibility for the deviations could be of systematic nature, such as finite volume or cut-off effects. While we do not discuss cut-off effects in the scope of this work, in the following section, we address the estimated corrections due to the finite volume effects

4.4.2 Ground state contribution to the inclusive rate

In this section, we discuss the ground state contribution defined in sec. 3.1.2, which serves as an important cross-check for our analysis strategy for the inclusive decays. Here, we limit ourselves to the VV channel for which we construct the ground state by considering the exclusive decay $D_s \to \eta \ell \nu_\ell$. In terms of the four-point function this translates to restricting the correlator to

$$C^{GS}_{\mu\nu}(t;\boldsymbol{q}) = \frac{1}{4M_{D_s}E_\eta} \langle D_s|V_\mu^\dagger|\eta\rangle \langle \eta|V_\nu|D_s\rangle \, e^{-E_\eta t}\,, \tag{4.8}$$

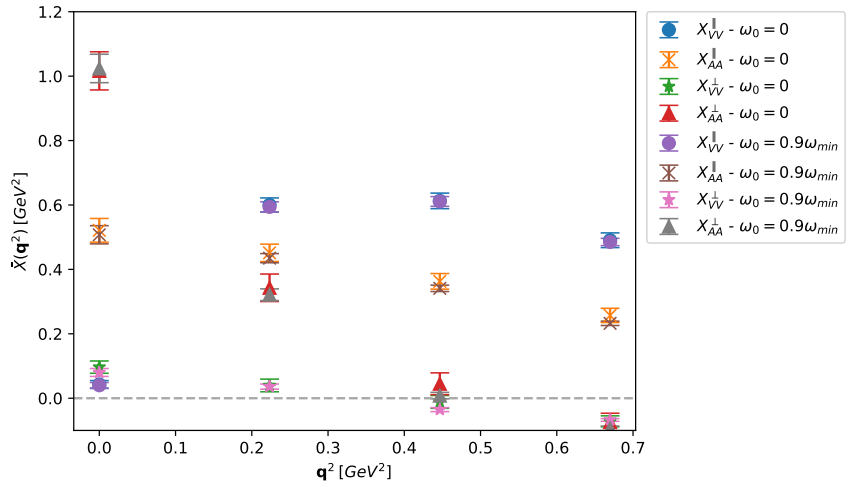

Figure 4.7: Contributions to the total $\bar{X}(\boldsymbol{q}^2)$ decomposed into longitudinal and transverse components of the channels $V_\mu^\dagger V_\mu$ and $A_\mu^\dagger A_\mu$. We compare the values for two choices of the starting point of the Chebyshev approximation.

where the superscript GS denotes the ground state limit. This correlator can be reconstructed from two- and three-point function through the ratio

$$R_{D_s\eta,\mu}(t;\boldsymbol{q}) = \sqrt{4M_{D_s}E_\eta}\sqrt{\frac{C^{SS}_{D_s\eta,\mu}(\boldsymbol{q},t_{\text{snk}},t,t_{\text{src}})C^{SS}_{\eta D_s,\mu}(\boldsymbol{q},t_{\text{snk}},t,t_{\text{src}})}{C^{SS}_{D_s}(t_{\text{snk}},t_{\text{src}})C^{SS}_{D_s}(\boldsymbol{q},t_{\text{snk}},t_{\text{src}})}} \tag{4.9}$$

which, for $t \gg t_{\text{src}}$ and $t \ll t_{\text{snk}}$, converges to $\mathcal{M}_\mu \equiv \langle\eta|V_\mu|D_s\rangle$. To continue, we consider the decomposition of the matrix element into form factors following

$$\mathcal{M}_\mu = f_+(q^2)(p_{D_s} + p_\eta)_\mu + f_-(p_{D_s} - p_\eta)_\mu\,. \tag{4.10}$$

We work in the rest frame of the D_s meson, i.e. $\boldsymbol{p}_{D_s} = \boldsymbol{0}$. Further, since we know that $R_{D_s\eta,0}(t;\boldsymbol{q}) \to \mathcal{M}_\mu$ we construct a fit prescription

$$R_{f_+}(t;\boldsymbol{q}) \overset{\boldsymbol{q}\neq\boldsymbol{0}}{=} \frac{1}{2M_{D_s}}\left(R_{D_s\eta,0}(t;\boldsymbol{q}) + (M_{D_s} - E_\eta)\frac{\sum_{i=1}^3 R_{D_s\eta,i}(t;\boldsymbol{q})}{\sum_{i=1}^3 q_i}\right), \tag{4.11}$$

which allows us to extract $f_+(q^2)$. This method has been applied in [93], where a good agreement between the expected exclusive contribution based on $f_+(q^2)$ extracted from the method described above and the ground state saturation assumption (4.8) for the inclusive data set has been found. The necessary correlation functions are not available for the current analysis of the D_s meson,

Table 4.1: Summary table for the values of $f_+(q^2)$ and $f_0(q^2)$ for the exclusive $D \to K\ell\nu_\ell$ decay for different values of q^2.

q^2 [GeV^2]	$f_+(q^2)$	$f_0(q^2)$
1.83(1)		1.00(2)
1.161(8)	1.06(2)	0.87(2)
0.627(7)	0.86(3)	0.78(3)
0.167(7)	0.74(4)	0.72(4)

and we limit ourselves to a comparison for the ground state using form factors determined for the exclusive $D \to K\ell\nu_\ell$ decay. The values for the form factors $f_+(q^2)$, obtained from lattice simulations using the same ensemble are summarized in tab. 4.1[1]. We perform an interpolation of these form factors and then use (3.52) in order to obtain the expected ground state contribution at the $\boldsymbol{q}^2$ values employed in the simulations and compare those to the results obtained for the inclusive analysis. We further determine the expected ground state contribution based on the interpolation for the whole $\boldsymbol{q}^2$ region available in the simulations. This is shown in Fig. 4.8.

[1]These numbers have not officially appeared in a publication but were handed to me following a private discussion with Prof. Takashi Kaneko who performed the analysis to extract the numbers shown in table 4.1. A discussion on the prospect of a $D \to K$ analysis has been discussed in [119]

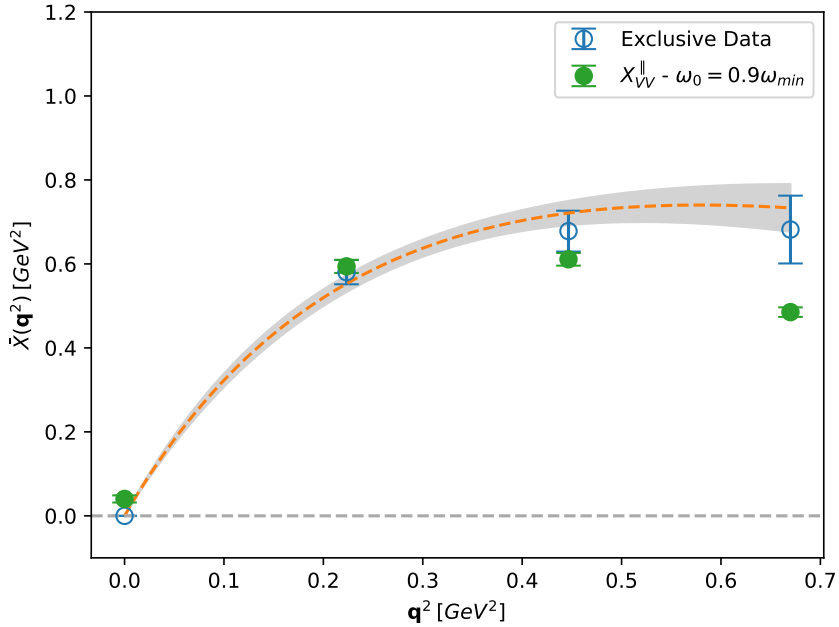

Figure 4.8: We show the $\bar{X}^{VV}_{\parallel}(\boldsymbol{q}^2)$ contribution to the total $\bar{X}(\boldsymbol{q}^2)$ in order to analyze the ground state contribution to the inclusive decay rate. Using the values for $f_+(q^2)$ shown in tab. 4.1 we determine the expected exclusive contribution using (3.52) for the $\boldsymbol{q}^2$ values used in the simulations (blue circles). We further employ a polynomial fit to $f_+(q^2)$ in order to include the estimated ground state contribution covering the whole $\boldsymbol{q}^2$ region (dashed line). We only show the results of the inclusive analysis obtained for the starting point $\omega_0 = 0.9\omega_{\min\, min}$ for the Chebyshev approximation.

We observe a reasonably good agreement between our inclusive analysis and the ground state contribution for the two smaller values of $\boldsymbol{q}^2$, while the discrepancy between the two increases for the two larger $\boldsymbol{q}^2$. It turned out that the inclusive process is largely dominated by its ground state contribution. Concerning the observed discrepancy for larger values of $\boldsymbol{q}^2$, they are partly a consequence of the degrading signal-to-noise ratio for larger values of $\boldsymbol{q}^2$. Further contributions to the discrepancy could originate from systematic effects such as those from the Chebyshev approximation. Nonetheless, this cross-check allows us to conclude that our results seem to be in the right ballpark and give us confidence in our analysis strategy.

4.4.3 Finalizing the analysis for $\Gamma/|V_{cs}|^2$

After this short excursion we continue our analysis of the inclusive decays. The next step is to sum all contributions of $\bar{X}^{\mathcal{P}}_{\mathcal{J}\mathcal{J}}(\boldsymbol{q}^2)$ for each $\boldsymbol{q}^2$ to obtain the values for $\bar{X}(\boldsymbol{q}^2)$, which is shown in Fig. 4.9. We perform a polynomial fit of order two to $\bar{X}(\boldsymbol{q}^2)$. In Fig. 4.9 we show the total $\sqrt{\boldsymbol{q}^2}\bar{X}(\boldsymbol{q}^2)$ for

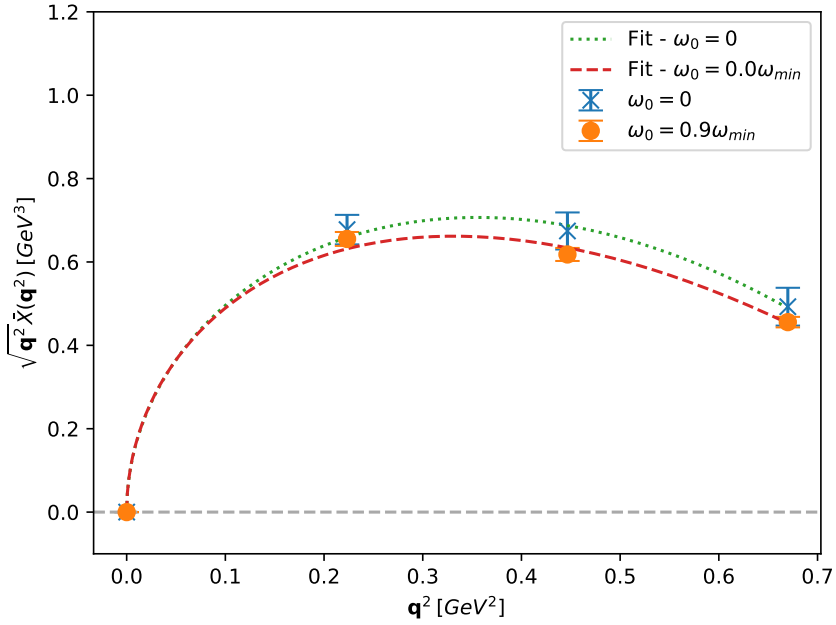

Figure 4.9: Integrand $\sqrt{\boldsymbol{q}^2}\bar{X}(\boldsymbol{q}^2)$ of (3.28) reconstructed from the lattice data for each value of $\boldsymbol{q}^2$ used in the lattice simulations.

Table 4.2: Extracted parameters for the fit to $\bar{X}(\boldsymbol{q}^2)$.

ω_0	α	β	γ	χ^2/dof
0	−0.65(43)	−1.20(33)	1.695(84)	0.62
$0.9\omega_{\text{min}}$	−0.07(22)	−1.69(20)	1.717(55)	2.5

each value of $\boldsymbol{q}^2$ while also including the results from our fit. Including the additional prefactor $\sqrt{\boldsymbol{q}^2}$ our total fit prescription is given by

$$f(\boldsymbol{q}^2) = (\alpha(\boldsymbol{q}^2)^2 + \beta\boldsymbol{q}^2 + \gamma)\sqrt{\boldsymbol{q}^2}\,. \tag{4.12}$$

The fitted parameters for both choices of the starting point of the approximation are shown in tab. 4.2. From here, it is straightforward to perform the $\boldsymbol{q}^2$ integration in (3.28) and we obtain

$$\Gamma/|V_{cs}|^2 = 7.9(15) \times 10^{-14}\,\text{GeV}\,, \tag{4.13}$$

and

$$\Gamma/|V_{cs}|^2 = 7.40(91) \times 10^{-14}\,\text{GeV}\,, \tag{4.14}$$

for $\omega_0 = 0$ and $0.9\omega_{\min}$, respectively. While we discuss methods towards estimating the systematical error in the following sections, here, we limit ourselves to only citing the statistical error.

To extract the CKM matrix element we now include the experimental data from the BESIII collaboration [109] of the inclusive semielectronic measurements of the D_s meson:

$$\Gamma(D_s^+ \to Xe^+\nu_e) = 8.23(31) \times 10^{-14}\,\text{GeV}\,. \tag{4.15}$$

Combining this result with our analysis, we can determine the CKM matrix element $|V_{cs}|$ for both choices of the starting point of the approximation

$$|V_{cs}| = 1.02(10) \tag{4.16}$$

and

$$|V_{cs}| = 1.055(68)\,, \tag{4.17}$$

where the former is determined for the choice of $\omega_0 = 0$ and the latter from $\omega_0 = 0.9\omega_{\min}$. We observe that the result for $\omega_0 = 0$ is associated with a larger error when compared to the number obtained from setting ω_0 closer to $\omega_{\min}$, which is in accordance with our conclusions from previous sections. Nonetheless, when compared to the value given in the PDG [120]

$$|V_{cs}| = 0.975(6)\,, \tag{4.18}$$

we observe an agreement on a $\sim 1\sigma$ level, indicating that our method is in the right ballpark.

4.4.4 Systematic error from the Chebyshev approximation

As we discussed in the previous section and in [104], high orders of the Chebyshev matrix elements simply reflect the prior distribution in $[-1, 1]$, due to the statistical fluctuation in the lattice data, limiting the polynomial order N usable in the approximation. Furthermore, in order to restore the physical result, we need to estimate the effect of the smearing applied to the kernel function, and we take the limits, i.e. the $N \to \infty$ and $\sigma \to 0$ limit, by considering (3.102). In this section we investigate possible corrections for the case of $\bar{X}^{\parallel}_{VV}(\boldsymbol{q}^2)$ for values of $\boldsymbol{q}^2$ corresponding to the smallest and largest values available in our simulations, i.e. $\boldsymbol{q}^2 = 0\,\text{GeV}^2$ and $0.67\,\text{GeV}^2$, before extending the analysis towards the full data set. We show how the method affects the final results based on the example of the spatial component V_iV_i, which only contribute with $l = 2$ in the kernel function. These two cases correspond to the kernel functions shown in the third row in Fig. 4.4.

In Fig. 4.10 we show how the coefficients of the Chebyshev approximation evolve when changing our setup from $N = 10$ and $\sigma = 0.1$ to $N = 100$ and $\sigma = 0.01$, while Fig. 4.11 shows the absolute

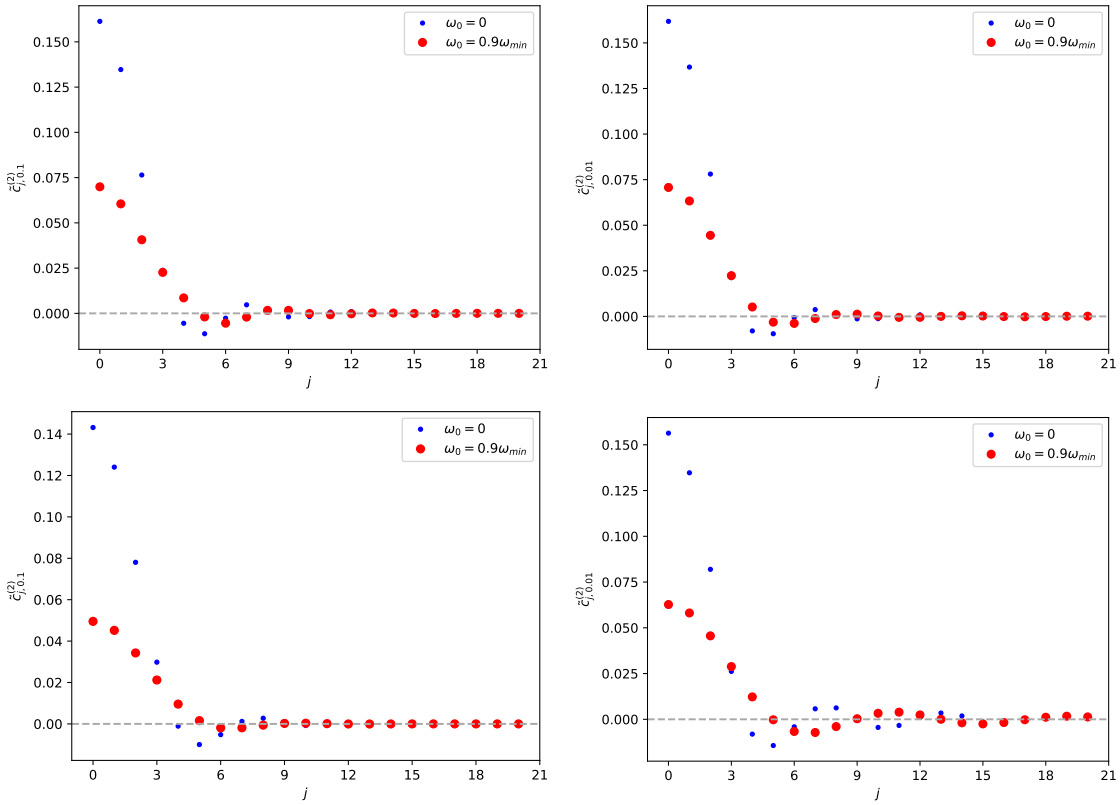

Figure 4.10: Coefficients $\tilde{c}_j^{(2)}$ for two choices of the smearing $\sigma = 0.1$ (left column) and $\sigma = 0.01$ (right column) in the kernel function calculated for two values of $\boldsymbol{q}^2 = 0\,\mathrm{GeV}^2$ (first row) and $0.67\,\mathrm{GeV}^2$ (second row). We compare the coefficients for both choices of the starting value ω_0.

value of the coefficients on a logarithmic scale. For all cases, we compare both choices of ω_0 and show the coefficients up to $j = 20$. From Fig. 4.10 we observe that the change of the smearing enhances the oscillating behavior of the coefficients, with this being more prominent for higher $\boldsymbol{q}^2$. Combining this with Fig. 4.11, we obtain an estimate on how strong the effect in the final contribution to the error will be: for $\boldsymbol{q}^2 = 0\,\mathrm{GeV}^2$ the effect is expected to be small since the change of the the smearing only has negligible effects on the exponential fall off of the magnitude of the coefficients, while for $\boldsymbol{q}^2 = 0.67\,\mathrm{GeV}^2$ the change in the smearing is sizable. For $\sigma = 0.1$ the coefficients drop off ~ 6 orders of magnitude, while for $\sigma = 0.01$ they only drop off ~ 2 orders of magnitude.

We then use (3.103), setting $N_{\mathrm{Cut}} = 10$, to obtain an error estimate by adding the absolute values of the Chebyshev coefficients above the cut-off as error bars to our value for the spatial current contribution. In Fig. 4.12 we show how $\bar{X}_\sigma^{(2)}$ evolves as a function of $1/N$. We observe that higher values of $\boldsymbol{q}^2$ receive much larger corrections, while small $\boldsymbol{q}^2$ values are quite stable in the limit.

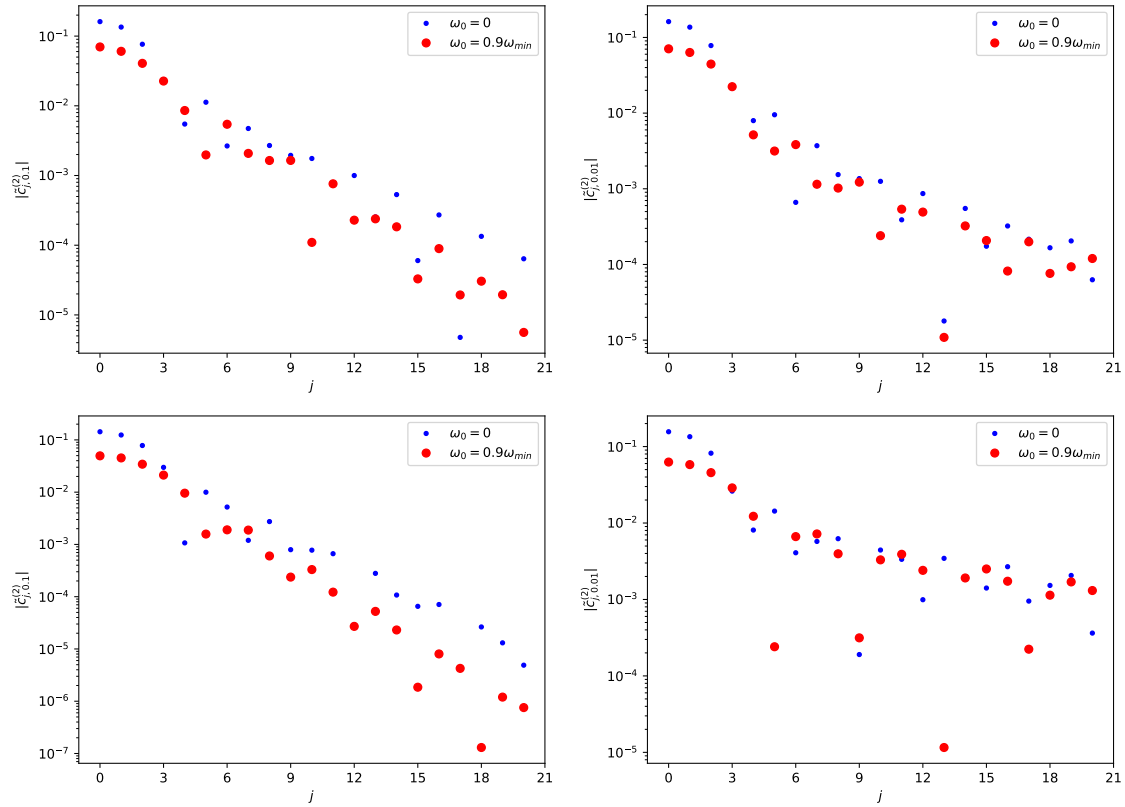

Figure 4.11: Absolute values of coefficients $\tilde{c}_j^{(2)}$ for two choices of the smearing $\sigma = 0.1$ (left column) and $\sigma = 0.01$ (right column) in the kernel function calculated for two values of $\boldsymbol{q}^2 = 0\,\mathrm{GeV}^2$ (first row) and $0.67\,\mathrm{GeV}^2$ (second row) on a logarithmic scale. We compare the coefficients for both choices of the starting value ω_0.

We see how our method, combining the $N \to \infty$ and $\sigma \to 0$ limit, affects our final results. For $\boldsymbol{q}^2 = 0\,\mathrm{GeV}^2$, we find a small increase in the error bars for $N = 20$ which stays constant for higher orders of N. The kernel function only possesses a very mild dependence on the smearing and that we already obtain a good approximation at order $N = 10$. This is verified by the first rows in Figs. 4.10 and 4.11, where we observe only minor changes in the coefficients and confirm that the magnitude of the coefficients drop off by at least 3 orders of magnitude for both choices of the smearing and between the two choices of ω_0. A different picture is seen in the case of $0.67\,\mathrm{GeV}^2$. While we observe that the mean value is relatively stable, i.e. the total contribution up to $N = 10$ is roughly the same, the error bars keep increasing as a function of $1/N$ and at $N = 100$ we are dominated by the error. Once again, we verify this from the corresponding coefficients in the second rows of Figs. 4.10 and 4.11. In the right panel, which shows the result for of $\sigma = 0.01$, or consequently $N = 100$, 4.10

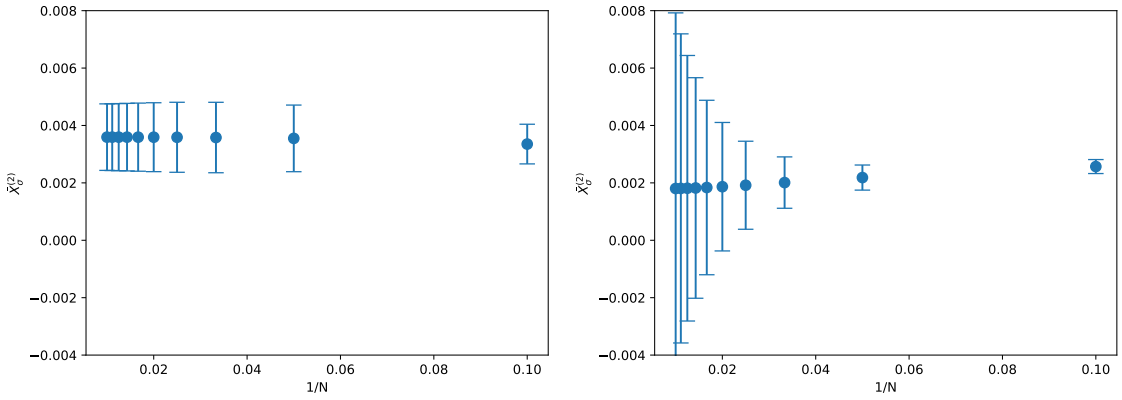

Figure 4.12: Evolution of the errorbars for the spatial current contribution of V_iV_i to the total value of $\bar{X}^{\parallel}_{VV}(\boldsymbol{q}^2)$ for $\boldsymbol{q}^2 = 0\,\mathrm{GeV}^2$ (left) and $0.67\,\mathrm{GeV}^2$ (right) as a function of $1/N$. The contribution shown corresponds to the $l = 2$ insertion in the kernel function.

shows that the coefficients are still fluctuating around zero and in 4.11 we observe that while the coefficients drop off ~ 6 orders of magnitude for $\sigma = 0.1$, they only fall off ~ 2 orders of magnitude for $\sigma = 0.01$ at the highest order shown. This results in larger contributions to the error following (3.103).

We now apply the method to determine all contributions shown in Fig. 4.7. In Fig. 4.13 we show the results where we expand our analysis to $N = 100$ and $\sigma = 0.01$. For the sake of visibility, we limit ourselves to the results for $\omega_0 = 0.9\omega_{\mathrm{min}}$.

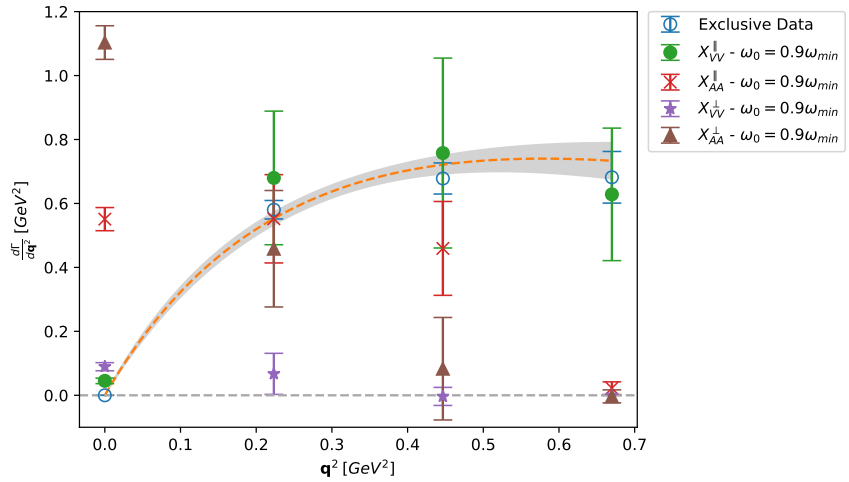

Figure 4.13: Contributions to the total $\bar{X}(\boldsymbol{q}^2)$ decomposed into longitudinal and transverse components of the channels $V_\mu^\dagger V_\mu$ and $A_\mu^\dagger A_\mu$. We apply our method into taking the limits needed to estimate the approximation error due to the smearing and the Chebyshev approximation. The parameters used in here correspond to $N = 100$ and $\sigma = 0.01$ and we set $N_{\text{Cut}} = 10$. We show the results obtained from setting the staring point of the approximation to $\omega_0 = 0.9\omega_{\text{min}}$.

By comparing Figs. 4.7 and 4.13, we observe a shift in the mean values for all data points. This is a consequence of the smaller smearing, as the kernel function is now approaching the unsmeared kernel. Combining this with our findings from Fig. 4.10, i.e. the exponential drop off of the coefficients, and we conclude that a reasonably precise approximation of the kernel function already at the cut-off order $N_{\text{Cut}} = 10$. Nonetheless, we also observe a substantial increase in the error bars from coefficients with $N > N_{\text{Cut}}$, making a phenomenological prediction challenging. This is a result of the way the estimate is constructed, since we assume to live on the mathematically allowed limits defined by the properties of the Chebyshev polynomial approach.

4.4.5 Systematic error from finite volume

This section addresses the estimation of the systematic error due to finite volume effects. Following the discussion from sec. 3.4.2, we use the model (3.116) and combine it with the lattice data to study the infinite volume extrapolation.

We consider the spectral density of the final state hadrons sketched in Fig. 4.14

$$\rho(\omega) = A\delta(\omega - m_X) + \rho_{\text{Ex}}(\omega)\,, \tag{4.19}$$

where we treat the ground state separately and $\rho_{\text{Ex}}(\omega)$ is the spectral function representing the

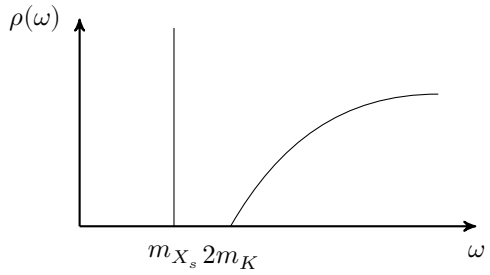

Figure 4.14: Spectral density $\rho(\omega)$ including the ground state $\omega = m_X$.

two-body excited states, i.e. (3.107) or (3.109). As mentioned in 3.4.2, the finite volume expressions of the spectrum is significantly different from its infinite volume counterpart. We define the fitting function to fit the lattice data

$$\bar{C}(t) = A_0 e^{-E_0 t} + s(L) \sum_i A_i e^{-E_i t} F(E_i)\,, \tag{4.20}$$

where we specifically pick out the ground state contribution and collect all excited state contributions into the sum of the second term. To obtain a more realistic picture we also include an additional factor $F(E_i)$ which is motivated by the time-like kaon form factor as

$$F(\epsilon) = \frac{1}{\epsilon^2 - m_J^2}\,, \tag{4.21}$$

where the mass m_J depends on whether $J = 0$ or $J = 1$ is considered. In the case of $J = 1$, corresponding to the insertion of the spatial components of the axial-vector current in the four-point function, the ground state is given by the ϕ meson with $J^P = 1^-$ and hence $m_J = m_\phi$. In the case of $J = 0$, i.e. the four-point function has the temporal components of the axial-vector currents inserted, we need to consider a ground state with $J^P = 0^+$ which decays into an $K\bar{K}$ state, for which we assume the f_0 meson, hence $m_J = m_{f_0}$. The ground state energy E_0 and its amplitude A_0 are determined through a preceding fit to the lattice data using a fit prescription similar to (4.2) to extract the corresponding quantities and are then included in the fit as a constraint through a prior. The excited states E_i and their amplitudes A_i are fixed through the model. The E_i are calculated straightforward through the energy dispersion relation $E_i = 2\sqrt{m_K^2 + \boldsymbol{q}^2}$, given that the values of $\boldsymbol{q}^2$ for a fixed volume L are known. As for the A_i's, they contain the relative difference in magnitude among each excited state in comparison to the lowest energy state, i.e. A_i is simply an array of integers with no direct physical meaning. The actual contribution is controlled by the pre-factor $s(L)$. To summarize, the parameters we extract from our fit are E_0, A_0 and $s(L)$. Following the fit, we can then determine $s(L')$ for any volume L' using the extracted value of $s(L)$ as a reference value

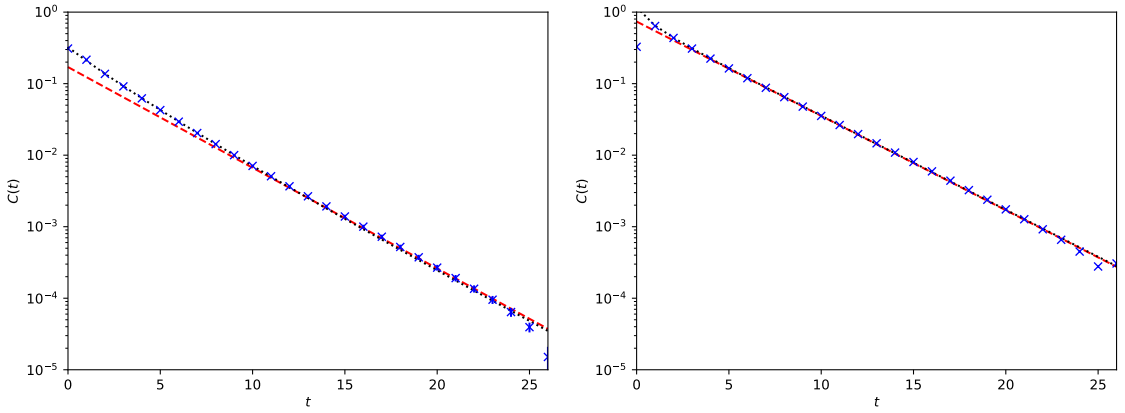

Figure 4.15: Four-point correlation function for the temporal current insertion of the axial channel (left) and the spatial components (right). For both plots we fit the correlator directly to extract the ground state contribution needed to fix the prior in our model. This fit is represented by the red dashed line. The black dash-dotted line represents the fit results obtained from a fit to our model using the fit prescription (4.20).

using (3.117). Before that, we investigate whether our model is able to reproduce the lattice data.

As a case study let us consider $\bar{X}^{\perp}_{AA}(\boldsymbol{q}^2)$ with $\boldsymbol{q}^2 = 0\,\mathrm{GeV}^2$, which only receives contributions from the spatial currents $A_i^\dagger A_i$. For the case of zero momentum insertion the $\parallel$ and $\perp$ contributions only differ by a constant factor of 2. We also study the case of two temporal current insertions $A_0 A_0$ contributing to $\bar{X}^{\parallel}_{AA}(\boldsymbol{q}^2)$. This contribution vanishes for $\boldsymbol{q}^2 = 0\,\mathrm{GeV}^2$ since the kernel (3.70) has a pre-factor of $\boldsymbol{q}^2$. The lightest hadronic states for the two cases considered correspond to $J^P = 0^+$ and 1^- for the temporal and spatial current insertions, respectively, and we can apply our model for both cases of the spectral density discussed in sec. 3.4.2.

In Fig. 4.15 we show the four-point correlation functions for both cases and include the fit functions obtained from the direct fit to the data used to extract the ground state as well as the one using the model (4.20). First, we confirm that the direct fit describes the ground state in the region of large time separations. Second, in case of the reconstructed fit, we obtain a good approximation of the correlator for short separations which contains contributions from excited states.

We now estimate the corrections due to the infinite volume. We consider two choices of the finite volume $L = 48^3$, which corresponds to the lattice data used to fixed the fit parameters and $L = 256^3$ which we set as the proxy for the infinite volume limit. The results as a function of the upper limit of the integral ω_{th} are shown in Figs. 4.16 and 4.17. We use the kernel (3.113) to take the change of ω_{th} into account. On the left hand side we combine our fitted data with the kernel function with the Heaviside function to determine the contribution to $\bar{X}^{\perp,\parallel}_{AA}(\boldsymbol{q}^2)$. On the right hand side we show the same contribution assuming a smeared kernel where we set the smearing to $\sigma = 0.1$. For the latter,

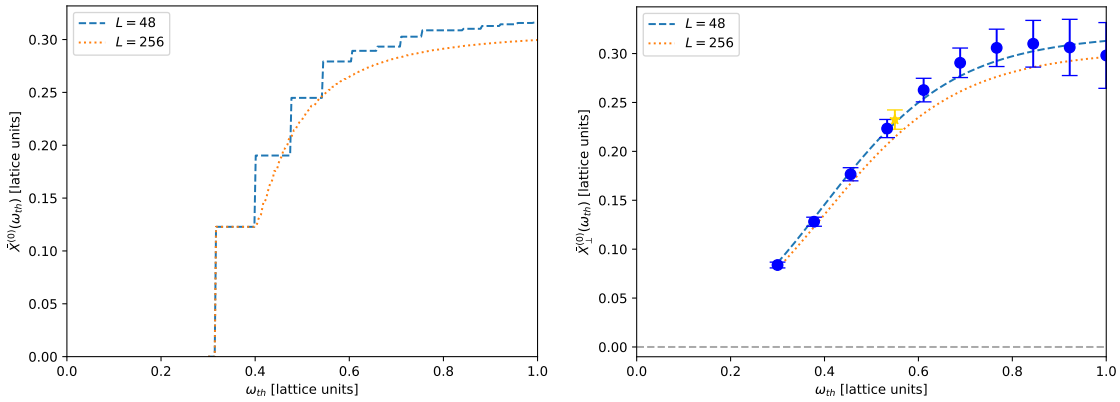

Figure 4.16: Contribution of temporal currents to $\bar{X}^{\parallel}_{AA}(\boldsymbol{q}^2)$ at $\boldsymbol{q}^2 = 0\,\mathrm{GeV}^2$. The left panel shows the infinite volume approximation where we assume the cut-off in the kernel function to be a sharp cut through a heaviside function. The right panel shows the infinite volume approximation under the assumption of the smeared kernel. Here, we also compare the results with those obtained from the Chebyshev analysis of our lattice data evaluated for different choices of the threshold ω_{th} represented by the blue dots. We further include the point of $\omega_{\mathrm{th}} = \omega_{\mathrm{th}}^{\mathrm{Phys}}$, i.e. the physical value of the threshold for a given momentum $\boldsymbol{q}$, denoted by the star symbol. In both cases the two volumes we use are $L = 48^3$ and 256^3. Due to the pre-factor of $\boldsymbol{q}^2$ appearing for the kernel function of $l = 0$, this does not result in an actual contribution in $\bar{X}^{\parallel,\parallel}_{AA}(\boldsymbol{q}^2)$.

we include a comparison to the results obtained from the Chebyshev approximation, repeating the analysis for each value of ω_{th}. We highlight the value at $\omega_{\mathrm{th}} = \omega_{\mathrm{th}}^{\mathrm{Phys}}$. Since an approximation of the kernel with a Heaviside function in terms of Chebyshev polynomials is not possible, it is not included for the unsmeared kernel. Nonetheless, this allows us to estimate the $\sigma \to 0$ limit. The picture confirms our conclusion from the previous chapter, the temporal component of $\bar{X}^{\parallel}_{AA}$, which only contributes with $l = 0$ in the kernel function receives larger corrections due to finite volume effects because of the sharp drop in the kernel, which is confirmed on the left hand side of Fig. 4.16. For the smeared kernel we find a relatively good agreement with the data but there is a visible volume dependence. We stress that in the case considered here, i.e. $\boldsymbol{q}^2 = 0$, the contribution of the temporal component vanishes. On the other hand, we concluded that for $l = 2$ we do not expect large corrections due to finite volume effects, which is the case for the spatial components contributing to $\bar{X}^{\perp}_{AA}$. The difference between the right and left hand side is marginal and we see virtually no dependence on the volume in the case of the smeared kernel. We also observe that our model based results are in good agreement with the data, as the lattice result nicely follows the model prediction.

We now construct an estimate of the corrections for our final value of $\bar{X}^{\perp}_{AA}(\mathbf{0}^2)$. We write the

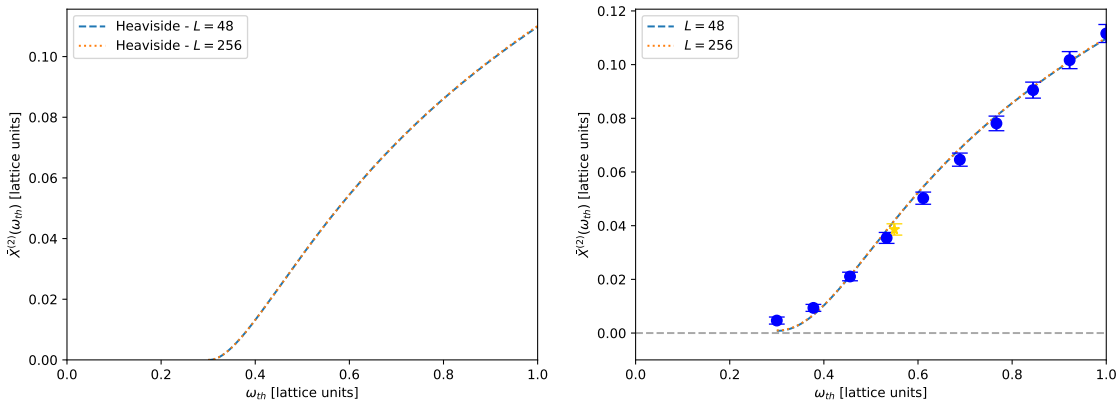

Figure 4.17: Contribution of spatial currents to $\bar{X}^{\perp}_{AA}(\boldsymbol{q}^2)$ at $\boldsymbol{q}^2 = 0\,\mathrm{GeV}^2$. The left panel shows the infinite volume approximation where we assume the cut-off in the kernel function to be a sharp cut through a heaviside function. The right panel shows the infinite volume approximation under the assumption of the smeared kernel. Here, we also compare the results with those obtained from the Chebyshev analysis of our lattice data evaluated for different choices of the threshold ω_{th} represented by the blue dots. We further include the point of $\omega_{\mathrm{th}} = \omega_{\mathrm{th}}^{\mathrm{Phys}}$, i.e. the physical value of the threshold for a given momentum $\boldsymbol{q}$, denoted by the star symbol. In both cases the two volumes we use are $L = 48^3$ and 256^3.

corrections in the following way

$$\begin{aligned}\bar{X}^{\perp}_{AA}(\mathbf{0}^2) = \bar{X}^{(2),\mathrm{Data}}_{A_iA_i}(\mathbf{0}^2;\omega_{\mathrm{th}} = \omega_{\mathrm{th}}^{\mathrm{Phys}}, L = 48^3, \sigma = 0.1) \\ + \underbrace{\bar{X}^{(2),\mathrm{Model}}_{A_iA_i}(\mathbf{0}^2;\omega_{\mathrm{th}}^{\mathrm{Phys}}, 256^3, 0.1) - \bar{X}^{(2),\mathrm{Model}}_{A_iA_i}(\mathbf{0}^2;\omega_{\mathrm{th}}^{\mathrm{Phys}}; 48^3, 0.1)}_{\text{Finite volume correction}} \\ + \underbrace{\bar{X}^{(2),\mathrm{Model}}_{A_iA_i}(\mathbf{0}^2;\omega_{\mathrm{th}}^{\mathrm{Phys}}, 256^3, 0) - \bar{X}^{(2),\mathrm{Model}}_{A_iA_i}(\mathbf{0}^2;\omega_{\mathrm{th}}^{\mathrm{Phys}}; 256^3, 0.1)}_{\text{Finite smearing correction}}\,.\end{aligned} \tag{4.22}$$

Translating this into numbers we obtain

$$\begin{aligned}\bar{X}^{\perp}_{AA}(\mathbf{0}^2) &= \underbrace{0.0786(31)}_{\text{Data}} + \underbrace{0.0001(0)}_{\text{Finite volume correction}} + \underbrace{0.0055(1)}_{\text{Finite smearing correction}} \\ &= 0.0843(31)\,.\end{aligned} \tag{4.23}$$

We find that the correction from the infinite volume limit are negligible, while the $\sigma \to 0$ limit gives a correction of the order $\sim 7\,\%$.

The small corrections from the finite volume are not to be understood as generally expected. The estimated corrections depend on the value of l in the kernel function and these can result in substantial corrections. Furthermore, the case discussed here is for the safe choice of zero momentum

insertion. For higher momentum insertion we expect larger corrections, due to the reduction in the allowed phase space. Additionally, in Fig. 4.15, the case of $\boldsymbol{q}^2 = 0$, we do not find significant contributions of excited states in the short distance behavior of the correlator, meaning that we cannot extract a lot of information even through our model.

Chapter 5

Conclusions and Outlook

In this work, we have extended the idea presented in [29] and applied it to the studies of the inclusive semileptonic decay of the charmed D_s mesons from lattice correlators using a full and flexible lattice setup. For analyzing the inclusive process we employ the Chebyshev polynomials with a trade off between the data and the Chebyshev matrix elements to account for the bounds on the Chebyshev polynomials. While not discussed in this work, a comparison with the Backus-Gilbert approach has been performed in [93]. We confirmed that the Chebyshev approximation enables an accurate and efficient way to determine the inclusive decay rate. By comparing our results with experimental data taken from the BESIII collaboration, we conclude that our prediction for the CKM matrix element $|V_{cs}|$ is in the right ballpark compared to the PDG value, although our analysis only includes the statistical error at this stage. Furthermore, we improved the approximation through Chebyshev polynomials by introducing a set of generic shifted polynomials in terms of $e^{-\omega}$. In the scope of this analysis we also compared our inclusive determination with the ground state limit using form factors taken from the exclusive $D \to K\ell\nu$ decay data. This analysis serves as an important cross-check of the inclusive analysis and enables the estimation of excited states contributions in the inclusive decay. We found a good agreement between inclusive and exclusive determination indicating a dominance of the ground state contribution in the inclusive rate. Larger discrepancies for higher values of $\boldsymbol{q}^2$ are likely due to the reduction of the phase space ω and the consequently required higher polynomial order in the approximation.

Additionally, we presented a first study of the systematic effects in the inclusive analysis of lattice data. The effects addressed in this work are the error due to the smearing of the kernel function in combination with the limited order of the polynomial approximation, as well as an estimate of the contribution from finite volume effects. For the error introduced by the smearing and approximation, we combined the two limits, namely the $\sigma \to 0$ and $N \to \infty$ limit, to obtain an estimate. Depending on the shape of the kernel function we encounter delicate cases, and higher

values of $\boldsymbol{q}^2$ require more attention since the available phase space in ω becomes smaller, requiring higher polynomial orders and smaller values of the smearing, to obtain a good estimate. To estimate the corrections for finite volume, we introduce a model. We found that the model reproduces our lattice correlators, we also have a dependence on the shape of the kernel function. In the case presented in this work, i.e. $\bar{X}_{\perp}^{AA}(\boldsymbol{q}^2)$ at $\boldsymbol{q}^2 = 0\,\mathrm{GeV}^2$, we found that the correction for the infinite volume limit are negligibly small, although we stress that this is not to be understood that finite volume corrections are expected to be small for all cases.

The methods to estimate the systematic errors still requires a lot of work in the future. Our error estimate due to our approximation is very conservative, since it comes from the mathematical bounds of the Chebyshev polynomials. Future studies for more realistic and stringent estimate on higher orders in the polynomials are required. As for the model used to estimate the finite volume effects, further studies to obtain a proper estimate are also required here. As discussed in this work, the model as it stands now is only applicable for the case of $\bar{X}_{\perp}^{AA}(\boldsymbol{q}^2)$ and the model would have to be adjusted for the different channels, which we are aiming to develop going forward. Furthermore, it is imperative to verify how our error estimate depends on the model to give a proper estimate of the systematic error associated. In the scope of this work, we based our model on the production of a two-body state from the vacuum. And although our model seems to result in a good reproduction of the lattice data, some tasks still remain. Some questions that have to be tackled going forward include but are not limited to: how does the result change when an initial state is included into the model? To what degree will introducing interactions affect the final result? In addition to these questions, at the end of the day what we have at hand right now is only a model and we plan to supplement this by increasing the amount of available data. This will not only enable us to perform the infinite volume limit based on an approach using lattice data, providing an important cross-check on the viability of our model, but by increasing the quality of the data we will also be able to increase the amount of data points that can be used in the determination of the Chebyshev matrix elements, which is also a potential prospect into obtaining a better understanding of the systematic error associated with the approximation.

Finally, this work has build a solid foundation in applying the techniques introduced in this work towards the inclusive decay. We have pushed the analysis forward by presenting first steps into understanding and estimating the systematic errors associated with our method and the more general topic of finite volume effects. Other than further developing the methods and ideas introduced in this work, there are further issues that we did not have the time to address in this work and will have to be postponed to future studies, such as discretization errors and the continuum limit. The plan for the near future is to generate additional data by repeating our computation for different ensembles before extending this analysis towards the inclusive decay of $B_{(s)}$ mesons where a preliminary study has been conducted by our friends from the UK [93]. We plan to verify whether our methods towards estimating the systematic errors discussed in this work can straightforwardly be applied in the case

of the bottom sector. The final goal is then to give a new and independent determination of the CKM matrix elements for both the charm and bottom sector, with the hope to shine a new light into the still unresolved discrepancy between exclusive and inclusive determination of the CKM matrix elements in the bottom sector.

Appendix A

Chebyshev Polynomials

This section focuses on the introduction and discussion of important properties of the standard Chebyshev polynomials relevant to this work. Furthermore, we put a special emphasis on the generalization for the shifted Chebyshev polynomials which play an integral role in the results presented in this work. Nonetheless, we are not able to give a full review on this topic and refer to [121] for more details.

A.1 Standard Polynomials

First, let us start by giving the definition of the first kind of Chebyshev polynomials

$$T_k : [-1,1] \to [-1,1]\,, \quad T_k(x) = \cos\left(k \cos^{-1}(x)\right)\,, \quad k \in \mathbb{N}\,. \tag{A.1}$$

By definition, they are orthogonal with respect to the scalar product

$$\int_{-1}^{1} T_r(x) T_s(x) \Omega(x) dx = \frac{\pi}{2} \delta_{rs}(1 + \delta_{r0})\,, \tag{A.2}$$

where $\Omega(x) = 1/\sqrt{1-x^2}$ defines a weight function. In terms of x^k, the polynomial expansion is defined as

$$T_n(x) = \sum_{k=0}^{n} t_k^{(n)} x^k\,, \tag{A.3}$$

where the definition of the coefficients $t_k^{(n)}$ is given by

$$\begin{aligned} t_0^{(n)} &= (-1)^{n/2} && \text{if } n \text{ even}\,, \\ t_k^{(n)} &= 0 && \text{if } n-k \text{ odd}\,, \\ t_k^{(n)} &= (-1)^{(n-k)/2} 2^{k-1} \frac{n}{\frac{n+k}{2}} \binom{\frac{n+k}{2}}{\frac{n-k}{2}} && \text{if } k \neq 0 \text{ and } n-k \text{ even}\,. \end{aligned} \tag{A.4}$$

Another useful property involves the reverse formula, i.e. the representation of x^k in terms of the standard Chebyshev polynomials

$$\begin{aligned} p_n(x) \equiv x^k &= 2^{1-n} \left[\frac{1}{2} \binom{n}{\frac{n}{2}} T_0(x) + \sum_{\substack{k=1 \\ n-k \text{ even}}}^{n} \binom{n}{\frac{n-k}{2}} T_k(x) \right] \\ &= \sum_{\substack{k=1 \\ n-k \text{ even}}}^{n}{}' \binom{n}{\frac{n-k}{2}} T_k(x)\,, \end{aligned} \tag{A.5}$$

where in the second line we absorb the first term into the sum and highlight the fact that it has to be halved by the prime, unless it is skipped.

A.1.1 Approximation using Chebyshev expansion

For a function $f : [-1, 1] \to \mathbb{R}$, the Chebyshev polynomials provide the best approximation for any given order N of the approximation in terms of the L_∞ norm. It is commonly referred to as an *minmax* approximation, i.e. the error between the reconstructed function and the target function is minimized. A convenient feature for the functions considered in this work is the fact that the Chebyshev approximation is guaranteed to converge for the $n \to \infty$ limit. The actual application of the Chebyshev polynomial approximation is given through

$$f(x) \simeq \frac{1}{2} c_0 T_0(x) + \sum_{j=0}^{N} c_j T_j(x)\,, \quad c_j = \frac{1}{\pi} \int_{-1}^{1} dx f(x) T_j(x) \Omega(x)\,, \tag{A.6}$$

where $T_0(x) = 0$ by definition. Furthermore, as can be seen in their definition, the coefficients are given by the projection of the target function f onto the basis of Chebyshev polynomials.

A.2 Shifted Chebyshev polynomials

In this work, instead of the standard Chebyshev polynomial approach discussed previously, we consider generic functions $f(x)$ defined in an interval $[a, b]$, which we approximate through Chebyshev polynomials in e^{-x}. This requires us to define shifted polynomials $\tilde{T}_j(x)$ with $x \in [a, b]$, so that their

domain and the one of the target function matches. The standard polynomials and their shifted variant are related through

$$\tilde{T}_j(x) = T_j(h(x))\,. \tag{A.7}$$

Here, $h : [a, b] \to [-1, 1]$ is an invertible function which maps the domain $[a, b]$ onto the domain where the standard Chebyshev polynomials are defined

$$h(x) = Ae^{-x} + B\,. \tag{A.8}$$

We now impose the conditions $h(a) = -1$ and $h(b) = 1$ to obtain expression for the coefficients A and B

$$A = -\frac{2}{e^{-a} - e^{-b}}\,, \quad B = \frac{e^{-a} + e^{-b}}{e^{-a} - e^{-b}}\,. \tag{A.9}$$

Furthermore, the orthogonality relation in (A.2) is now given by

$$\int_a^b dx\tilde{T}_r(x)\tilde{T}_s(x)\Omega_h(x) = \int_a^b dxT_r(h(x))T_s(h(x))\Omega_h(x)\,, \tag{A.10}$$

where the map dependent weight for the shifted $\tilde{T}_k(x)$ is given by $\Omega_h(x)$. The original integral (A.2) can be recovered by setting $x = h^{-1}(x)$ and $dx = 1/h'(h^{-1}(x))dy$, so that the integral (A.10) becomes

$$\int_{h(a)}^{h(b)} dyT_r(y)T_s(y)\frac{\Omega_h(h^{-1}(y))}{h'(h^{-1}(y))}\,. \tag{A.11}$$

To continue, we write the weight as

$$\Omega_h(x) = \Omega(h(x))|h'(x)|\,, \tag{A.12}$$

so that we finally arrive at

$$\int_a^b dx\tilde{T}_r(x)\tilde{T}_s(x)\Omega_h(x) = \int_{-1}^1 dyT_r(y)T_s(y)\Omega(y)\,. \tag{A.13}$$

The next step is to generalize the polynomial expression and their properties. The generalized

polynomial expression of (A.3) can be written as

$$\tilde{T}_n(x) = \sum_{j=0}^{n} t_j^{(n)} h(x)^j = \sum_{j=0}^{n} t_j^{(n)} (Ae^{-x} + B)^j = \sum_{j=0}^{n} t_j^{(n)} \sum_{k=0}^{j} \binom{j}{k} A^k B^{j-k} e^{-kx} \tag{A.14}$$

We can furthermore isolate the coefficients of $\exp(-kx)$ by expanding this sum explicitly and re-summing

$$\begin{aligned}
\tilde{T}_n(x) &= A^n e^{-nx} \left[\binom{n}{n} t_n^{(n)} \right] + A^{n-1} e^{-(n-1)x} \left[\binom{n-1}{n-1} t_{n-1}^{(n)} + \binom{n}{n-1} t_n^{(n)} B^1 \right] \\
&\quad + A^{n-2} e^{-(n-2)x} \left[\binom{n-2}{n-2} t_{n-2}^{(n)} + \binom{n-1}{n-2} t_{n-1}^{(n)} B + \binom{n}{n-2} t_n^{(n)} B^2 \right] + \cdots \\
&\quad + A^1 e^{-x} \left[\binom{1}{1} t_1^{(n)} + \binom{2}{1} t_2^{(n)} B + \binom{3}{1} t_3^{(n)} B^2 + \cdots + \binom{n}{1} t_n^{(n)} B^{n-1} \right] \\
&\quad + \left[\binom{0}{0} t_0^{(n)} + \binom{1}{0} t_1^{(n)} B + \cdots + \binom{n}{0} t_n^{(n)} B^n \right] \\
&= \sum_{k=0}^{n} e^{-kx} A^k \sum_{j=k}^{n} \binom{j}{k} t_j^{(n)} B^{j-k} \\
&= \sum_{k=0}^{n} \tilde{t}_k^{(n)} e^{-kx} \,,
\end{aligned} \tag{A.15}$$

where in the last step we introduce the short-hand notation for the coefficients $\tilde{t}_k^{(n)}$ given by

$$\tilde{t}_k^{(n)} = A^k \sum_{j=k}^{n} \binom{j}{k} t_j^{(n)} B^{j-k} = \left(\frac{A}{B}\right)^k \sum_{j=k}^{n} \binom{j}{k} t_j^{(n)} B^j \,. \tag{A.16}$$

In a similar vein, we can also generalize the inverse formula defined in (A.5)

$$\tilde{p}(x) \equiv h(x)^n = 2^{1-2n} \sum_{\substack{j=0 \\ n-j \text{ even}}}^{n}{}' \binom{n}{\frac{n-j}{2}} \tilde{T}_j(x) \,, \quad x \in [a, b] \,, \tag{A.17}$$

where, once again, the prime denotes that the term at $j = 0$ has to be halved.

We may also define an iterative expression through which we can generally determine expressions for $\exp(-nx)$. For this, we assume $\tilde{p}_0(x) = 1$ and

$$\tilde{p}_n(x) = (Ae^{-x} + B)^n = \sum_{k=0}^{n} A^k B^{n-k} e^{-kx} \,, \tag{A.18}$$

so that our expression for $\exp(-nx)$ reads

$$e^{-nx} = \frac{1}{A^n}\left[\tilde{p}_n(x) - \sum_{k=0}^{n-1} A^k B^{n-k} e^{-kx}\right] . \tag{A.19}$$

As a final step, we rewrite everything in terms of the shifted Chebyshev polynomials by collecting all the numerical coefficients

$$e^{-nx} = \sum_{j=0}^{n} \tilde{a}_j^{(n)} \tilde{T}_j(x) , \tag{A.20}$$

where we introduce a set of coefficients $\{\tilde{a}_0^{(n)}, \tilde{a}_1^{(n)}, \cdots, \tilde{a}_n^{(n)}\}$, which can be straightforwardly determined numerically for each value of n. We will give some additional information on these coefficients in Sec. A.2.2

A.2.1 Chebyshev expansion with exponential map

Following the previous section, we now have all necessary tools to formulate the polynomial approximation of a generic function in $\exp(-x)$, similar to Sec. A.1.1. To stay true to the application in this work, we will only consider the case of $f : [x_0, \infty) \to \mathbb{R}$, for which the approximation reads

$$f(x) \simeq \frac{1}{2}\tilde{c}_0 \tilde{T}_0(x) + \sum_{k=1}^{N} \tilde{c}_k \tilde{T}_k(x) , \quad \tilde{c}_k = \frac{2}{\pi}\int_{\omega_0}^{\infty} dx f(x) \tilde{T}_k(x) \Omega_h(x) . \tag{A.21}$$

In a more explicit way, the coefficients can be rewritten as

$$\tilde{c}_k = \frac{2}{\pi}\int_{\omega_0}^{\infty} d\theta f(h^{-1}(\cos\theta))(\cos k\theta) = \frac{2}{\pi}\int_{\omega_0}^{\infty} d\theta f\left(-\ln\left(\frac{\cos\theta - B}{A}\right)\right)(\cos k\theta) , \tag{A.22}$$

where in the second step we set $y = h(x)$, so that through inversion

$$x = h^{-1}(y) = -\log\left(\frac{y - B}{A}\right) . \tag{A.23}$$

For this specific choice of the limits $[x_0, \infty)$ the coefficients defined in (A.9) read

$$A = -2e^{x_0} , \quad B = 1 \tag{A.24}$$

An example using shifted Chebyshev Polynomials

In this section we consider a short example on a practical representation of the Chebyshev polynomials. Here, we will consider the case of $x_0 = 0$, so that the coefficients A and B for our map $h(\omega)$:

$[0, \infty) \to [-1, 1]$ defined in (A.8) are given by

$$A = -2 \quad \text{and} \quad B = 1\,. \tag{A.25}$$

The definition of the shifted Chebyshev polynomials is hence given by

$$\tilde{T}_k = T(h(x)) = T(-2x + 1)\,, \tag{A.26}$$

where we defined $x = e^{-\omega}$. The next step is to consider the analytical form of the Chebyshev polynomials. Let us start by giving the expression for the standard, unshifted Chebyshev polynomials which are defined through a recursive relation

$$T_0(x) = 1\,, \quad T_1(x) = x\,, \quad T_j(x) = 2xT_{j-1}(x) - T_{j-2}(X)\,. \tag{A.27}$$

We can hence define the shifted Chebyshev polynomials as

$$\tilde{T}_0(x) = 1\,, \quad \tilde{T}_1(x) = -2x + 1\,, \quad \tilde{T}_j(x) = 2(-2x + 1)\tilde{T}_{j-1}(x) - \tilde{T}_{j-2}(x)\,. \tag{A.28}$$

Using this relation we can give the first few shifted polynomials with $j \geq 2$

$$\tilde{T}_2 = 8x^2 - 8x + 1 \tag{A.29}$$

$$\tilde{T}_3 = -32x^3 + 48x^2 - 18x + 1 \tag{A.30}$$

$$\tilde{T}_4 = 128x^4 - 256x^3 + 160x^2 - 32x + 1 \tag{A.31}$$

$$\vdots \tag{A.32}$$

We show them in Fig. A.1

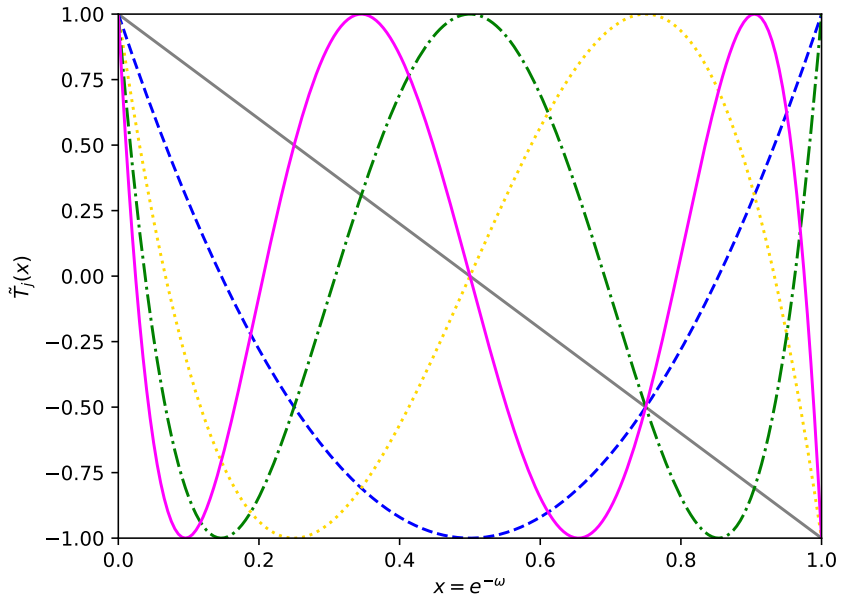

Figure A.1: Shifted Chebyshev polynomials $\tilde{T}_j(x)$ for $j = 1$ (solid gray), $j = 2$ (dashed blue), $j = 3$ (dotted gold), $j = 4$ (dash-dot green) and $j = 4$ (solid magenta) as a function of $x = e^{-\omega}$.

We now have one possible representation of the shifted Chebyshev approximation. In the next section we discuss how the Chebyshev matrix elements necessary for the analysis of the inclusive decays can be extracted based on this representation.

Extracting Chebyshev matrix elements

This section presents a short discussion on how the Chebyshev matrix elements can be extracted based on the representation of the Chebyshev matrix elements discussed in the previous section.

Towards this end, let us shortly recount the necessary information required to do so, which we discussed in Sec. 3. We remember the definition on how the Chebyshev matrix elements are defined

$$\langle \tilde{T}_k \rangle_{\mu\nu} \equiv \frac{\langle \psi^\mu | \tilde{T}_k(\hat{H}) | \psi^\nu \rangle}{\langle \psi^\mu | \psi^\nu \rangle} \,, \tag{A.33}$$

as well as how they are related to the correlator data obtained from lattice simulations

$$\frac{\langle \psi^\mu | e^{-\hat{H}t} | \psi^\nu \rangle}{\langle \psi^\mu | \psi^\nu \rangle} = \frac{C_{\mu\nu}(t + 2t_0)}{C_{\mu\nu}(2t_0)} \equiv \bar{C}_{\mu\nu}(t) \,, \tag{A.34}$$

where the definition of the correlator $C_{\mu\nu}(t)$ is given in (3.60) and (3.61). We also recall how the

approximation of the kernel function is defined based on (3.94)

$$\langle K_\sigma^{(l)} \rangle_{\mu\nu} = \frac{1}{2} \tilde{c}^{(l)}_{\mu\nu,0} \langle \tilde{T}_0 \rangle_{\mu\nu} + \sum_{k=1}^{N} \tilde{c}^{(l)}_{\mu\nu,k} \langle \tilde{T}_k \rangle_{\mu\nu} \,. \tag{A.35}$$

By the definition (A.34) it then becomes clear that the r.h.s. of (A.35) is nothing but a linear combination of those terms at different time slices t. If we now consider our representation of the Chebyshev matrix element introduced in the previous section, we an give the first couple of terms following

$$\langle \tilde{T}_0(x) \rangle = 1 \,, \tag{A.36}$$
$$\langle \tilde{T}_1(x) \rangle = -2\bar{C}(1) + 1 \,, \tag{A.37}$$
$$\langle \tilde{T}_2(x) \rangle = 8\bar{C}(2) - 8\bar{C}(1) + 1 \,, \tag{A.38}$$
$$\langle \tilde{T}_2(x) \rangle = -32\bar{C}(3) + 48\bar{C}(2) - 18\bar{C}(1) + 1 \tag{A.39}$$
$$\vdots \,, \tag{A.40}$$

which allows us to essentially determine the Chebyshev matrix elements to arbitrary order N, limited only by the available time slices of the lattice data. We have additionally dropped the subscript $\mu\nu$ in this notation for simplicity, since the strategy applies the same independent of those indices.

As we previously discussed in Sec. 3.3.1, the lattice data is associated with an statistical error which results in a violation of the bound $|\langle \tilde{T}_k \rangle| \leq 1$. As a result, instead of solving the linear system mentioned above, we define Chebyshev matrix elements $\bar{T}_k \equiv \langle \tilde{T}_k(x) \rangle$ which we then extract from a fit by using the inverse formula of the shifted Chebyshev polynomials (A.17) which in our case reads as

$$\bar{C}(t) = (-1)^t 2^{1-2t} \left[\frac{1}{2} \binom{2t}{t} + \sum_{r=0}^{t} \binom{2t}{t-r} \bar{T}_r \right] \,, \tag{A.41}$$

where we can now introduce the bound $|\bar{T}_k| \leq 1$ through the use of priors following the procedure layed out in sec. 3.3.1.

A.2.2 Matrix relations

As previously discussed, in this work we only consider the case in which the domain of the target function is given by $[x_0, \infty)$. For this case we have given the definition of the coefficients A and B in (A.24). We will now discuss some useful properties that arise by setting $x_0 \neq 0$ and then apply those to the case relevant for this work, although a generalization is trivial.

Towards this end, let us start by expressing (A.15) in matrix notation

$$\begin{pmatrix} \tilde{T}_0(x) \\ \tilde{T}_1(x) \\ \vdots \\ \vdots \\ \tilde{T}_n(x) \end{pmatrix} = \begin{pmatrix} \tilde{t}_0^{(0)} & 0 & \cdots & \cdots & 0 \\ \tilde{t}_0^{(1)} & \tilde{t}_1^{(1)} & 0 & \cdots & 0 \\ \vdots & \vdots & \ddots & \ddots & \vdots \\ \vdots & \vdots & & \ddots & 0 \\ \tilde{t}_0^{(n)} & \tilde{t}_1^{(n)} & \cdots & \cdots & 0 \end{pmatrix} \begin{pmatrix} 1 \\ e^{-x} \\ \vdots \\ \vdots \\ e^{-nx} \end{pmatrix} . \tag{A.42}$$

Additionally, the same representation can be written for (A.20)

$$\begin{pmatrix} 1 \\ e^{-x} \\ \vdots \\ \vdots \\ e^{-nx} \end{pmatrix} = \begin{pmatrix} \tilde{a}_0^{(0)} & 0 & \cdots & \cdots & 0 \\ \tilde{a}_0^{(1)} & \tilde{a}_1^{(1)} & 0 & \cdots & 0 \\ \vdots & \vdots & \ddots & \ddots & \vdots \\ \vdots & \vdots & & \ddots & 0 \\ \tilde{a}_0^{(n)} & \tilde{a}_1^{(n)} & \cdots & \cdots & 0 \end{pmatrix} \begin{pmatrix} \tilde{T}_0(x) \\ \tilde{T}_1(x) \\ \vdots \\ \vdots \\ \tilde{T}_n(x) \end{pmatrix} . \tag{A.43}$$

By comparing these two $(n+1) \times (n+1)$ matrices T_M with $(T_M)_{ij} = \tilde{t}_j^{(i)}$ and A_M with $(A_M)_{ij} = \tilde{a}_j^{(i)}$, it becomes obvious that they are related through

$$T_M = A_M^{-1} , \tag{A.44}$$

i.e. the two matrices are the inverse of each other. We can also obtain an additional decomposition of the matrix T_M by looking at (A.15) and (A.16)

$$T_M = APt , \tag{A.45}$$

where we introduce the diagonal matrix $A_{kk} = A^k = (-2e^{x_0})^k$, the lower triangular Pascal matrix $P_{jk} = \binom{j}{k}$ and the matrix t which follows from the definition given in (A.4). This decomposition allows to easily visualize the effect of changing the lower bound of the domain x_0. By setting $A_{kk}|_{x_0 \neq 0} = e^{x_0 k} \, A_{kk}|_{x_0=0}$, it follows

$$(T_M)_{nk}|_{x_0 \neq 0} = \tilde{t}_k^{(n)}\Big|_{x_0 \neq 0} = e^{x_0 n} \, \tilde{t}_k^{(n)}\Big|_{x_0=0} \quad , \quad (A_M)_{nk}|_{x_0 \neq 0} = \tilde{a}_k^{(n)}\Big|_{x_0 \neq 0} = e^{-x_0 n} \, \tilde{a}_k^{(n)}\Big|_{x_0=0} . \tag{A.46}$$

Bibliography

[1] The ATLAS Collaboration. *Observation of a new particle in the search for the Standard Model Higgs boson with the ATLAS detector at the LHC*. 2012. arXiv: 1207.7214 [hep-ex].

[2] Michael E. Peskin and Daniel V. Schroeder. *An Introduction to quantum field theory*. Reading, USA: Addison-Wesley, 1995. ISBN: 9780201503975, 0201503972. URL: http://www.slac.stanford.edu/~mpeskin/QFT.html.

[3] M. et al. Tanabashi. "Review of Particle Physics." In: *Phys. Rev. D* 98 (3 Aug. 2018), p. 030001. DOI: 10.1103/PhysRevD.98.030001. URL: https://link.aps.org/doi/10.1103/PhysRevD.98.030001.

[4] John F Donoghue, Eugene Golowich, and Barry R Holstein. *Dynamics of the Standard Model*. Cambridge monographs on particle physics, nuclear physics, and cosmology. Includes exercises. Cambridge: Cambridge Univ. Press, 1992. DOI: 10.1017/CBO9780511524370. URL: https://cds.cern.ch/record/238727.

[5] David J Griffiths. *Introduction to elementary particles; 2nd rev. version*. Physics textbook. New York, NY: Wiley, 2008. URL: https://cds.cern.ch/record/111880.

[6] O. Nachtmann. *Phänomene und Konzepte der Elementarteilchenphysik*. Vieweg, 1986.

[7] Gerard 't Hooft and M. J. G. Veltman. "Regularization and Renormalization of Gauge Fields." In: *Nucl. Phys.* B44 (1972), pp. 189–213. DOI: 10.1016/0550-3213(72)90279-9.

[8] Gerard 't Hooft and M. J. G. Veltman. "Combinatorics of gauge fields." In: *Nucl. Phys.* B50 (1972), pp. 318–353. DOI: 10.1016/S0550-3213(72)80021-X.

[9] David J. Gross and Frank Wilczek. "Ultraviolet Behavior of Nonabelian Gauge Theories." In: *Phys. Rev. Lett.* 30 (1973). [,271(1973)], pp. 1343–1346. DOI: 10.1103/PhysRevLett.30.1343.

[10] H. David Politzer. "Asymptotic Freedom: An Approach to Strong Interactions." In: *Phys. Rept.* 14 (1974), pp. 129–180. DOI: 10.1016/0370-1573(74)90014-3.

[11] S. L. Glashow. "Partial Symmetries of Weak Interactions." In: *Nucl. Phys.* 22 (1961), pp. 579–588. DOI: 10.1016/0029-5582(61)90469-2.

[12] Steven Weinberg. "A Model of Leptons." In: *Phys. Rev. Lett.* 19 (1967), pp. 1264–1266. DOI: 10.1103/PhysRevLett.19.1264.

[13] Abdus Salam. "Weak and Electromagnetic Interactions." In: *Conf. Proc.* C680519 (1968), pp. 367–377. DOI: 10.1142/9789812795915_0034.

[14] H. Georgi. "LIE ALGEBRAS IN PARTICLE PHYSICS. FROM ISOSPIN TO UNIFIED THEORIES." In: *Front. Phys.* 54 (1982), pp. 1–255.

[15] C. S. Wu et al. "Experimental Test of Parity Conservation in Beta Decay." In: *Phys. Rev.* 105 (1957), pp. 1413–1414. DOI: 10.1103/PhysRev.105.1413.

[16] J. H. Christenson et al. "Evidence for the 2π Decay of the K_2^0 Meson." In: *Phys. Rev. Lett.* 13 (1964), pp. 138–140. DOI: 10.1103/PhysRevLett.13.138.

[17] Nicola Cabibbo. "Unitary Symmetry and Leptonic Decays." In: *Phys. Rev. Lett.* 10 (1963). [,648(1963)], pp. 531–533. DOI: 10.1103/PhysRevLett.10.531.

[18] Makoto Kobayashi and Toshihide Maskawa. "CP Violation in the Renormalizable Theory of Weak Interaction." In: *Prog. Theor. Phys.* 49 (1973), pp. 652–657. DOI: 10.1143/PTP.49.652.

[19] Lincoln Wolfenstein. "Parametrization of the Kobayashi-Maskawa Matrix." In: *Phys. Rev. Lett.* 51 (21 Nov. 1983), pp. 1945–1947. DOI: 10.1103/PhysRevLett.51.1945. URL: https://link.aps.org/doi/10.1103/PhysRevLett.51.1945.

[20] Taizo Muta. *Foundations of Quantum Chromodynamics: An Introduction to Perturbative Methods in Gauge Theories, (3rd ed.)* Vol. 78. World scientific Lecture Notes in Physics. Hackensack, N.J.: World Scientific, 2010. ISBN: 9789812793539. URL: http://www-spires.fnal.gov/spires/find/books/www?cl=QC793.3.Q35M88::2010.

[21] W. Greiner and A. Schäfer. *Quantum chromodynamics*. Theoretische Physik. Springer-Verlag, 1994. ISBN: 9783540571032.

[22] Alexander Khodjamirian. "Quantum chromodynamics and hadrons: An Elementary introduction." In: *High-energy physics. Proceedings, European School, Tsakhkadzor, Armenia, August 24-September 6, 2003*. 2004, pp. 173–222. arXiv: hep-ph/0403145 [hep-ph]. URL: http://doc.cern.ch/yellowrep/2005/2005-007/p173.pdf.

[23] Hans Frauenfelder and Ernest M. Henley. *Teilchen und Kerne. subatomare Physik; 40 Tab.* ger. 2. Aufl. München ; Wien: Oldenbourg, 1987, 630 S. ISBN: 3-486-20334-7 and 978-3-486-20334-9.

[24] Fyodor Tkachov. "A Contribution to the history of quarks: Boris Struminsky's 1965 JINR publication." In: (2009). arXiv: 0904.0343 [physics.hist-ph].

[25] M. Y. Han and Yoichiro Nambu. "Three Triplet Model with Double SU(3) Symmetry." In: *Phys. Rev.* 139 (1965). [,187(1965)], B1006–B1010. DOI: 10.1103/PhysRev.139.B1006.

[26] O. W. Greenberg. "Spin and Unitary Spin Independence in a Paraquark Model of Baryons and Mesons." In: *Phys. Rev. Lett.* 13 (1964), pp. 598–602. DOI: 10.1103/PhysRevLett.13.598.

[27] H. David Politzer. "Reliable Perturbative Results for Strong Interactions?" In: *Phys. Rev. Lett.* 30 (1973). [,274(1973)], pp. 1346–1349. DOI: 10.1103/PhysRevLett.30.1346.

[28] Alexander Khodjamirian. *Hadron Form Factors: From Basic Phenomenology to QCD Sum Rules*. Boca Raton, FL, USA: CRC Press, Taylor & Francis Group, 2020. ISBN: 978-1-138-30675-2, 978-1-315-14200-5.

[29] Paolo Gambino and Shoji Hashimoto. "Inclusive Semileptonic Decays from Lattice QCD." In: *Phys. Rev. Lett.* 125.3 (2020), p. 032001. DOI: 10.1103/PhysRevLett.125.032001. arXiv: 2005.13730 [hep-lat].

[30] Yasmine Sara Amhis et al. "Averages of b-hadron, c-hadron, and τ-lepton properties as of 2021." In: *Phys. Rev. D* 107.5 (2023), p. 052008. DOI: 10.1103/PhysRevD.107.052008. arXiv: 2206.07501 [hep-ex].

[31] Aneesh V. Manohar and Mark B. Wise. "Inclusive semileptonic B and polarized Lambda(b) decays from QCD." In: *Phys. Rev. D* 49 (1994), pp. 1310–1329. DOI: 10.1103/PhysRevD.49.1310. arXiv: hep-ph/9308246.

[32] B. Blok et al. "Differential distributions in semileptonic decays of the heavy flavors in QCD." In: *Phys. Rev. D* 49 (1994). [Erratum: Phys.Rev.D 50, 3572 (1994)], p. 3356. DOI: 10.1103/PhysRevD.50.3572. arXiv: hep-ph/9307247.

[33] Ikaros I. Y. Bigi, N. G. Uraltsev, and A. I. Vainshtein. "Nonperturbative corrections to inclusive beauty and charm decays: QCD versus phenomenological models." In: *Phys. Lett. B* 293 (1992). [Erratum: Phys.Lett.B 297, 477–477 (1992)], pp. 430–436. DOI: 10.1016/0370-2693(92)90908-M. arXiv: hep-ph/9207214.

[34] Ikaros I. Y. Bigi et al. "QCD predictions for lepton spectra in inclusive heavy flavor decays." In: *Phys. Rev. Lett.* 71 (1993). Ed. by Ikaros I Bigi, Paolo Gambino, and Thomas Mannel, pp. 496–499. DOI: 10.1103/PhysRevLett.71.496. arXiv: hep-ph/9304225.

[35] Junegone Chay, Howard Georgi, and Benjamin Grinstein. "Lepton energy distributions in heavy meson decays from QCD." In: *Phys. Lett. B* 247 (1990), pp. 399–405. DOI: 10.1016/0370-2693(90)90916-T.

[36] Kenneth G. Wilson. "Nonlagrangian models of current algebra." In: *Phys. Rev.* 179 (1969), pp. 1499–1512. DOI: 10.1103/PhysRev.179.1499.

[37] Leo P. Kadanoff and Horacio Ceva. "Determination of an opeator algebra for the two-dimensional Ising model." In: *Phys. Rev. B* 3 (1971), pp. 3918–3938. DOI: 10.1103/PhysRevB.3.3918.

[38] Paolo Gambino, Kristopher J. Healey, and Sascha Turczyk. "Taming the higher power corrections in semileptonic B decays." In: *Phys. Lett. B* 763 (2016), pp. 60–65. DOI: 10.1016/j.physletb.2016.10.023. arXiv: 1606.06174 [hep-ph].

[39] Matteo Fael, Thomas Mannel, and K. Keri Vos. "V_{cb} determination from inclusive $b \to c$ decays: an alternative method." In: *JHEP* 02 (2019), p. 177. DOI: 10.1007/JHEP02(2019)177. arXiv: 1812.07472 [hep-ph].

[40] Thomas Mannel. "Operator product expansion for inclusive semileptonic decays in heavy quark effective field theory." In: *Nucl. Phys. B* 413 (1994), pp. 396–412. DOI: 10.1016/0550-3213(94)90625-4. arXiv: hep-ph/9308262.

[41] Matteo Fael, Thomas Mannel, and K. Keri Vos. "The Heavy Quark Expansion for Inclusive Semileptonic Charm Decays Revisited." In: *JHEP* 12 (2019), p. 067. DOI: 10.1007/JHEP12(2019)067. arXiv: 1910.05234 [hep-ph].

[42] Paolo Gambino et al. "Lattice QCD study of inclusive semileptonic decays of heavy mesons." In: *JHEP* 07 (2022), p. 083. DOI: 10.1007/JHEP07(2022)083. arXiv: 2203.11762 [hep-lat].

[43] Mikhail A. Shifman, A. I. Vainshtein, and Valentin I. Zakharov. "QCD and Resonance Physics. Theoretical Foundations." In: *Nucl. Phys.* B147 (1979), pp. 385–447. DOI: 10.1016/0550-3213(79)90022-1.

[44] A. Khodjamirian and R. Ruckl. "QCD sum rules for exclusive decays of heavy mesons." In: *Adv. Ser. Direct. High Energy Phys.* 15 (1998). [,345(1998)], pp. 345–401. DOI: 10.1142/9789812812667_0005. arXiv: hep-ph/9801443 [hep-ph].

[45] Eduardo de Rafael. "An Introduction to sum rules in QCD: Course." In: *Probing the standard model of particle interactions. Proceedings, Summer School in Theoretical Physics, NATO Advanced Study Institute, 68th session, Les Houches, France, July 28-September 5, 1997. Pt. 1, 2.* 1997, pp. 1171–1218. arXiv: hep-ph/9802448 [hep-ph].

[46] Pietro Colangelo and Alexander Khodjamirian. "QCD sum rules, a modern perspective." In: (2000), pp. 1495–1576. DOI: 10.1142/9789812810458_0033. arXiv: hep-ph/0010175 [hep-ph].

[47] A. Khodjamirian et al. "Predictions on B —> pi anti-l nu(l), D —> pi anti-l nu(l) and D —> K anti-l nu(l) from QCD light cone sum rules." In: *Phys. Rev.* D62 (2000), p. 114002. DOI: 10.1103/PhysRevD.62.114002. arXiv: hep-ph/0001297 [hep-ph].

[48] A. Khodjamirian et al. "Semileptonic charm decays $D \to \pi\ell\nu_\ell$ and $D \to K\ell\nu_\ell$ from QCD Light-Cone Sum Rules." In: *Phys. Rev.* D80 (2009), p. 114005. DOI: 10.1103/PhysRevD.80.114005. arXiv: 0907.2842 [hep-ph].

[49] Kenneth G. Wilson. "Confinement of Quarks." In: *Phys. Rev. D* 10 (1974). Ed. by J. C. Taylor, pp. 2445–2459. DOI: 10.1103/PhysRevD.10.2445.

[50] M. Creutz. "Monte Carlo Study of Quantized SU(2) Gauge Theory." In: *Phys. Rev. D* 21 (1980), pp. 2308–2315. DOI: 10.1103/PhysRevD.21.2308.

[51] Don Weingarten. "Monte Carlo Evaluation of Hadron Masses in Lattice Gauge Theories with Fermions." In: *Phys. Lett. B* 109 (1982). Ed. by J. Julve and M. Ramón-Medrano, p. 57. DOI: 10.1016/0370-2693(82)90463-4.

[52] H. Hamber and G. Parisi. "Numerical Estimates of Hadronic Masses in a Pure SU(3) Gauge Theory." In: *Phys. Rev. Lett.* 47 (1981). Ed. by J. Julve and M. Ramón-Medrano, p. 1792. DOI: 10.1103/PhysRevLett.47.1792.

[53] S. Duane et al. "Hybrid Monte Carlo." In: *Phys. Lett. B* 195 (1987), pp. 216–222. DOI: 10.1016/0370-2693(87)91197-X.

[54] Steven A. Gottlieb et al. "Hybrid Molecular Dynamics Algorithms for the Numerical Simulation of Quantum Chromodynamics." In: *Phys. Rev. D* 35 (1987), pp. 2531–2542. DOI: 10.1103/PhysRevD.35.2531.

[55] F. Butler et al. "Hadron mass predictions of the valence approximation to lattice QCD." In: *Phys. Rev. Lett.* 70 (1993), pp. 2849–2852. DOI: 10.1103/PhysRevLett.70.2849. arXiv: hep-lat/9212031.

[56] F. Butler et al. "Hadron masses from the valence approximation to lattice QCD." In: *Nucl. Phys. B* 430 (1994), pp. 179–228. DOI: 10.1016/0550-3213(94)90654-8. arXiv: hep-lat/9405003.

[57] S. Aoki et al. "Quenched light hadron spectrum." In: *Phys. Rev. Lett.* 84 (2000), pp. 238–241. DOI: 10.1103/PhysRevLett.84.238. arXiv: hep-lat/9904012.

[58] S. Durr et al. "Ab-Initio Determination of Light Hadron Masses." In: *Science* 322 (2008), pp. 1224–1227. DOI: 10.1126/science.1163233. arXiv: 0906.3599 [hep-lat].

[59] Paul H. Ginsparg and Kenneth G. Wilson. "A Remnant of Chiral Symmetry on the Lattice." In: *Phys. Rev. D* 25 (1982), p. 2649. DOI: 10.1103/PhysRevD.25.2649.

[60] David B. Kaplan. "A Method for simulating chiral fermions on the lattice." In: *Phys. Lett. B* 288 (1992), pp. 342–347. DOI: 10.1016/0370-2693(92)91112-M. arXiv: hep-lat/9206013.

[61] Vadim Furman and Yigal Shamir. "Axial symmetries in lattice QCD with Kaplan fermions." In: *Nucl. Phys. B* 439 (1995), pp. 54–78. DOI: 10.1016/0550-3213(95)00031-M. arXiv: hep-lat/9405004.

[62] Rajamani Narayanan and Herbert Neuberger. "A Construction of lattice chiral gauge theories." In: *Nucl. Phys. B* 443 (1995), pp. 305–385. DOI: 10.1016/0550-3213(95)00111-5. arXiv: hep-th/9411108.

[63] Herbert Neuberger. "Exactly massless quarks on the lattice." In: *Phys. Lett. B* 417 (1998), pp. 141–144. DOI: 10.1016/S0370-2693(97)01368-3. arXiv: hep-lat/9707022.

[64] Herbert Neuberger. "More about exactly massless quarks on the lattice." In: *Phys. Lett. B* 427 (1998), pp. 353–355. DOI: 10.1016/S0370-2693(98)00355-4. arXiv: hep-lat/9801031.

[65] Christof Gattringer and Christian B. Lang. *Quantum chromodynamics on the lattice*. Vol. 788. Berlin: Springer, 2010. ISBN: 978-3-642-01849-7, 978-3-642-01850-3. DOI: 10.1007/978-3-642-01850-3.

[66] Michael Creutz. *Quarks, Gluons and Lattices*. Oxford University Press, 1983. ISBN: 978-1-00-929039-5, 978-1-00-929038-8, 978-1-00-929037-1, 978-0-521-31535-7. DOI: 10.1017/9781009290395.

[67] Thomas DeGrand and Carleton E. Detar. *Lattice methods for quantum chromodynamics*. 2006.

[68] M. Luscher and P. Weisz. "On-Shell Improved Lattice Gauge Theories." In: *Commun. Math. Phys.* 97 (1985). [Erratum: Commun.Math.Phys. 98, 433 (1985)], p. 59. DOI: 10.1007/BF01206178.

[69] K. Symanzik. "Continuum Limit and Improved Action in Lattice Theories. 2. O(N) Nonlinear Sigma Model in Perturbation Theory." In: *Nucl. Phys. B* 226 (1983), pp. 205–227. DOI: 10.1016/0550-3213(83)90469-8.

[70] K. Symanzik. "Continuum Limit and Improved Action in Lattice Theories. 1. Principles and φ^4 Theory." In: *Nucl. Phys. B* 226 (1983), pp. 187–204. DOI: 10.1016/0550-3213(83)90468-6.

[71] Holger Bech Nielsen and M. Ninomiya. "Absence of Neutrinos on a Lattice. 1. Proof by Homotopy Theory." In: *Nucl. Phys. B* 185 (1981). Ed. by J. Julve and M. Ramón-Medrano. [Erratum: Nucl.Phys.B 195, 541 (1982)], p. 20. DOI: 10.1016/0550-3213(82)90011-6.

[72] Holger Bech Nielsen and M. Ninomiya. "Absence of Neutrinos on a Lattice. 2. Intuitive Topological Proof." In: *Nucl. Phys. B* 193 (1981), pp. 173–194. DOI: 10.1016/0550-3213(81)90524-1.

[73] Rajamani Narayanan and Herbert Neuberger. "Infinitely many regulator fields for chiral fermions." In: *Phys. Lett. B* 302 (1993), pp. 62–69. DOI: 10.1016/0370-2693(93)90636-V. arXiv: hep-lat/9212019.

[74] Rajamani Narayanan and Herbert Neuberger. "Chiral fermions on the lattice." In: *Phys. Rev. Lett.* 71.20 (1993), p. 3251. DOI: 10.1103/PhysRevLett.71.3251. arXiv: hep-lat/9308011.

[75] Rajamani Narayanan and Herbert Neuberger. "Chiral determinant as an overlap of two vacua." In: *Nucl. Phys. B* 412 (1994), pp. 574–606. DOI: 10.1016/0550-3213(94)90393-X. arXiv: hep-lat/9307006.

[76] M. Tomii et al. "Renormalization of domain-wall bilinear operators with short-distance current correlators." In: *Phys. Rev. D* 94.5 (2016), p. 054504. DOI: 10.1103/PhysRevD.94.054504. arXiv: 1604.08702 [hep-lat].

[77] Renwick J. Hudspith et al. "α_s from the Lattice Hadronic Vacuum Polarisation." In: (Apr. 2018). arXiv: 1804.10286 [hep-lat].

[78] Katsumasa Nakayama, Brendan Fahy, and Shoji Hashimoto. "Short-distance charmonium correlator on the lattice with Möbius domain-wall fermion and a determination of charm quark mass." In: *Phys. Rev. D* 94.5 (2016), p. 054507. DOI: 10.1103/PhysRevD.94.054507. arXiv: 1606.01002 [hep-lat].

[79] Ph. Boucaud et al. "Dynamical twisted mass fermions with light quarks." In: *Phys. Lett. B* 650 (2007), pp. 304–311. DOI: 10.1016/j.physletb.2007.04.054. arXiv: hep-lat/0701012.

[80] Philippe Boucaud et al. "Dynamical Twisted Mass Fermions with Light Quarks: Simulation and Analysis Details." In: *Comput. Phys. Commun.* 179 (2008), pp. 695–715. DOI: 10.1016/j.cpc.2008.06.013. arXiv: 0803.0224 [hep-lat].

[81] M. Foster and Christopher Michael. "Quark mass dependence of hadron masses from lattice QCD." In: *Phys. Rev. D* 59 (1999), p. 074503. DOI: 10.1103/PhysRevD.59.074503. arXiv: hep-lat/9810021.

[82] P. A. Boyle et al. "Use of stochastic sources for the lattice determination of light quark physics." In: *JHEP* 08 (2008), p. 086. DOI: 10.1088/1126-6708/2008/08/086. arXiv: 0804.1501 [hep-lat].

[83] Richard C. Brower, Harmut Neff, and Kostas Orginos. "The Möbius domain wall fermion algorithm." In: *Comput. Phys. Commun.* 220 (2017), pp. 1–19. DOI: 10.1016/j.cpc.2017.01.024. arXiv: 1206.5214 [hep-lat].

[84] Yigal Shamir. "Chiral fermions from lattice boundaries." In: *Nucl. Phys. B* 406 (1993), pp. 90–106. DOI: 10.1016/0550-3213(93)90162-I. arXiv: hep-lat/9303005.

[85] Yigal Shamir. "Constraints on the existence of chiral fermions in interacting lattice theories." In: *Phys. Rev. Lett.* 71 (17 Oct. 1993), pp. 2691–2694. DOI: 10.1103/PhysRevLett.71.2691. URL: https://link.aps.org/doi/10.1103/PhysRevLett.71.2691.

[86] A. Borici. "Truncated overlap fermions." In: *Nucl. Phys. B Proc. Suppl.* 83 (2000). Ed. by M. Campostrini et al., pp. 771–773. DOI: 10.1016/S0920-5632(00)91802-4. arXiv: hep-lat/9909057.

[87] Artan Borici. "Truncated overlap fermions: The Link between overlap and domain wall fermions." In: *NATO Sci. Ser. C* 553 (2000), pp. 41–52. arXiv: hep-lat/9912040.

[88] G. Martinelli et al. "A General method for nonperturbative renormalization of lattice operators." In: *Nucl. Phys. B* 445 (1995), pp. 81–108. DOI: 10.1016/0550-3213(95)00126-D. arXiv: hep-lat/9411010.

[89] Martin Luscher. "Advanced lattice QCD." In: *Les Houches Summer School in Theoretical Physics, Session 68: Probing the Standard Model of Particle Interactions*. Feb. 1998, pp. 229–280. arXiv: hep-lat/9802029.

[90] Brian Colquhoun et al. "Form factors of B→$\pi\ell\nu$ and a determination of |Vub| with Möbius domain-wall fermions." In: *Phys. Rev. D* 106.5 (2022), p. 054502. DOI: 10.1103/PhysRevD.106.054502. arXiv: 2203.04938 [hep-lat].

[91] Y. Aoki et al. "$B \to D^*\ell\nu_\ell$ semileptonic form factors from lattice QCD with Möbius domain-wall quarks." In: (June 2023). arXiv: 2306.05657 [hep-lat].

[92] Stephen R. Sharpe. "Future of Chiral Extrapolations with Domain Wall Fermions." In: *Workshop on Domain Wall Fermions at Ten Years*. June 2007. arXiv: 0706.0218 [hep-lat].

[93] Alessandro Barone et al. "Approaches to inclusive semileptonic $B_{(s)}$-meson decays from Lattice QCD." In: *JHEP* 07 (2023), p. 145. DOI: 10.1007/JHEP07(2023)145. arXiv: 2305.14092 [hep-lat].

[94] E. Witten. "Current algebra theorems for the U(1) "Goldstone boson"." In: *Nuclear Physics B* 156.2 (Sept. 1979), pp. 269–283. DOI: 10.1016/0550-3213(79)90031-2.

[95] G. Veneziano. "U(1) without instantons." In: *Nuclear Physics B* 159.1 (Nov. 1979), pp. 213–224. DOI: 10.1016/0550-3213(79)90332-8.

[96] Luigi Del Debbio, Leonardo Giusti, and Claudio Pica. "Topological susceptibility in the SU(3) gauge theory." In: *Phys. Rev. Lett.* 94 (2005), p. 032003. DOI: 10.1103/PhysRevLett.94.032003. arXiv: hep-th/0407052.

[97] Martin Luscher and Filippo Palombi. "Universality of the topological susceptibility in the SU(3) gauge theory." In: *JHEP* 09 (2010), p. 110. DOI: 10.1007/JHEP09(2010)110. arXiv: 1008.0732 [hep-lat].

[98] Shoji Hashimoto. "Inclusive semi-leptonic B meson decay structure functions from lattice QCD." In: *PTEP* 2017.5 (2017), 053B03. DOI: 10.1093/ptep/ptx052. arXiv: 1703.01881 [hep-lat].

[99] George Backus and Freeman Gilbert. "The Resolving Power of Gross Earth Data." In: *Geophysical Journal of the Royal Astronomical Society* 16 (Oct. 1968), pp. 169–205. DOI: 10.1111/j.1365-246X.1968.tb00216.x.

[100] John Bulava et al. "Inclusive rates from smeared spectral densities in the two-dimensional O(3) non-linear σ-model." In: *JHEP* 07 (2022), p. 034. DOI: 10.1007/JHEP07(2022)034. arXiv: 2111.12774 [hep-lat].

[101] Martin Hansen, Alessandro Lupo, and Nazario Tantalo. "Extraction of spectral densities from lattice correlators." In: *Phys. Rev. D* 99.9 (2019), p. 094508. DOI: 10.1103/PhysRevD.99.094508. arXiv: 1903.06476 [hep-lat].

[102] J. C. A. Barata and K. Fredenhagen. "Particle scattering in Euclidean lattice field theories." In: *Commun. Math. Phys.* 138 (1991), pp. 507–520. DOI: 10.1007/BF02102039.

[103] Gabriela Bailas, Shoji Hashimoto, and Tsutomu Ishikawa. "Reconstruction of smeared spectral function from Euclidean correlation functions." In: *PTEP* 2020.4 (2020), 043B07. DOI: 10.1093/ptep/ptaa044. arXiv: 2001.11779 [hep-lat].

[104] Ryan Kellermann et al. "Inclusive semi-leptonic decays of charmed mesons with Möbius domain wall fermions." In: *PoS* LATTICE2022 (2023), p. 414. DOI: 10.22323/1.430.0414. arXiv: 2211.16830 [hep-lat].

[105] Laurent Lellouch and Martin Luscher. "Weak transition matrix elements from finite volume correlation functions." In: *Commun. Math. Phys.* 219 (2001), pp. 31–44. DOI: 10.1007/s002200100410. arXiv: hep-lat/0003023.

[106] Laurent Lellouch. "Flavor physics and lattice quantum chromodynamics." In: *Les Houches Summer School: Session 93: Modern perspectives in lattice QCD: Quantum field theory and high performance computing*. Apr. 2011, pp. 629–698. arXiv: 1104.5484 [hep-lat].

[107] John Bulava. "The spectral reconstruction of inclusive rates." In: *PoS* LATTICE2022 (2023), p. 231. DOI: 10.22323/1.430.0231. arXiv: 2301.04072 [hep-lat].

[108] J. Gasser and H. Leutwyler. "Chiral Perturbation Theory to One Loop." In: *Annals Phys.* 158 (1984), p. 142. DOI: 10.1016/0003-4916(84)90242-2.

[109] Medina Ablikim et al. "Measurement of the absolute branching fraction of inclusive semielectronic D_s^+ decays." In: *Phys. Rev. D* 104.1 (2021), p. 012003. DOI: 10.1103/PhysRevD.104.012003. arXiv: 2104.07311 [hep-ex].

[110] Szabolcs Borsanyi et al. "High-precision scale setting in lattice QCD." In: *JHEP* 09 (2012), p. 010. DOI: 10.1007/JHEP09(2012)010. arXiv: 1203.4469 [hep-lat].

[111] Colin Morningstar and Mike J. Peardon. "Analytic smearing of SU(3) link variables in lattice QCD." In: *Phys. Rev. D* 69 (2004), p. 054501. DOI: 10.1103/PhysRevD.69.054501. arXiv: hep-lat/0311018.

[112] Peter A. Boyle. "Conserved currents for Mobius Domain Wall Fermions." In: *PoS* LATTICE2014 (2015), p. 087. DOI: 10.22323/1.214.0087.

[113] Peter Boyle et al. *Grid: Data parallel C++ mathematical object library*. URL: https://github.com/paboyle/Grid.

[114] Peter Boyle et al. "Grid: A next generation data parallel C++ QCD library." In: (Dec. 2015). arXiv: 1512.03487 [hep-lat].

[115] Azusa Yamaguchi et al. "Grid: OneCode and FourAPIs." In: *PoS* LATTICE2021 (2022), p. 035. DOI: 10.22323/1.396.0035. arXiv: 2203.06777 [hep-lat].

[116] A. Portelli et al. *aportelli/hadrons: Hadrons v1.3*. 2022. DOI: 10.5281/zenodo.4063666.

[117] P. Lepage and C. Gohlke. *gplepage/lsqfit: lsqfit version 12.0.3*. 2021. DOI: 10.5281/zenodo.5777652.

[118] G. P. Lepage et al. "Constrained curve fitting." In: *Nucl. Phys. B Proc. Suppl.* 106 (2002). Ed. by M. Muller-Preussker et al., pp. 12–20. DOI: 10.1016/S0920-5632(01)01638-3. arXiv: hep-lat/0110175.

[119] Takashi Kaneko. "Heavy flavor physics from lattice QCD." In: *PoS* LATTICE2022 (2023), p. 238. DOI: 10.22323/1.430.0238. arXiv: 2304.01618 [hep-lat].

[120] R. L. Workman et al. "Review of Particle Physics." In: *PTEP* 2022 (2022), p. 083C01. DOI: 10.1093/ptep/ptac097.

[121] Alexander Weiße et al. "The kernel polynomial method." In: *Reviews of Modern Physics* 78.1 (Mar. 2006), pp. 275–306. DOI: 10.1103/revmodphys.78.275. URL: https://doi.org/10.1103%2Frevmodphys.78.275.

Acknowledgments

I want to first express my gratitude towards my supervisor Prof. Dr. Shoji Hashimoto, who provided me with irreplaceable guidance during my PhD. He always had an open door to answer all my questions and discuss whenever I hit a wall. In addition to this, I thank him for holding daily zoom meetings during the Covid pandemic when I was not able to enter Japan prior to 2022. I am certain I would not haven been able to write this thesis without his support.

I further wish to express my gratitude to Prof. Dr. Thomas Mannel from the University of Siegen, for introducing and recommending me to Shoji being one of the reasons I was able to enter Japan and become a student at SOKENDAI and a part of KEK.

Additional thanks goes to Maki Ohishi and the whole secretarial body of KEK and SOKENDAI. Without her assistance it would have not been possible for me to build a life in Japan as smoothly as I did. Her knowledge and help in dealing with everything of bureaucratic nature, and her help in fulfilling all my obligations as a graduate student have been indispensable and I am sure I would not have been able to reach this point without her support.

I also wish to address a special thanks to Alessandro Barone, my colleague and friend who is working on a similar topic to mine and who also recently obtained his degree. It was extremely helpful to have someone to discuss with, who not only works in the same topic as oneself, but also someone who encounters the same problems during the analysis. We had a lot of fruitful discussions which definitely helped me in finishing this thesis.

I further want to direct my thanks to all the people I had the pleasure of meeting in Japan, including, but not limited to, Joe, Protick, Zhi, Gaku and many more. Everyone provided me with enough distractions so that the always looming deadlines never became too much of a burden.

Finally, I express my gratitude towards my mother who supported my, admittedly selfish, decision to leave Germany and start studying in Japan. She always supports my ideas and plans in any way she could and without her I would not have reached the point I am at now.